ABSTRACT

Title of dissertation: A SEARCH FOR MUON NEUTRINOS FROM GAMMA-RAY BURSTS WITH THE ICECUBE 22-STRING DETECTOR

A. Philip Roth Jr., Doctor of Philosophy, 2009

Dissertation directed by: Professor Kara Hoffman
Department of Physics

Two searches are conducted for muon neutrinos from Gamma-Ray Bursts (GRBs) using the IceCube detector. Gamma-Ray Bursts are brief and transient emissions of keV/MeV radiation occuring with a rate of a few per day uniformly in the sky. Swift and other satellites of the Third Interplanetary Network (IPN3) detect these GRBs and send notices out via the GRB Coordinate Network (GCN). The fireball model describing the physics of GRBs predicts the emission of muon neutrinos from these bursts. IceCube is a cubic kilometer neutrino detector buried in the deep antarctic ice at the South Pole that can be used to find these prediceted but still unobserved neutrinos. It is sensitive to them by detecting Cherenkov light from secondary muons produced when the neutrinos interact in or near the instrumented volume. The construction of IceCube has been underway since the austral summer of 2004-2005 and will continue until 2011. The growing IceCube detector will soon be sensitivite to the high energy neutrino emission from GRBs that is predicted by the fireball model. A blind and triggered search of the 22-string IceCube data for

this neutrino emission was conducted. The principal background to the observation of neutrinos in IceCube is muons generated in cosmic-ray air-showers in the atmosphere above the detector. Atmospheric neutrinos make up a separate irreducible background to the detection of extraterrestrial neutrinos. A binned stacked search of 41 bursts occuring in the northern hemisphere greatly reduces the muon background by looking for tracks moving up through the detector. The atmospheric neutrino background is greatly reduced by the temporal constraints of the search, making it effectively background free. 40 individual unbinned searches of bursts occuring in the southern hemisphere extend IceCube's sensitivity to the higher background regions above the horizon. No significant excesses over background expectations are found in either search. A 90% confidence upper limit on the neutrino fluence from northern hemisphere bursts is set at 6.52×10^{-3} erg cm^{-2} with 90% of the expected signal between 87.9 TeV and 10.4 PeV.

A SEARCH FOR MUON NEUTRINOS FROM GAMMA-RAY BURSTS WITH THE ICECUBE 22-STRING DETECTOR

by

A. Philip Roth Jr.

Dissertation submitted to the Faculty of the Graduate School of the
University of Maryland, College Park in partial fulfillment
of the requirements for the degree of
Doctor of Philosophy
2009

Advisory Committee:
Dr. Kara Hoffman, Chair/Advisor
Dr. Jordan Goodman
Dr. William McDonough
Dr. Julie McEnery
Dr. Rabindra Mohapatra
Dr. Gregory Sullivan

Table of Contents

List of Tables v

List of Figures vi

List of Abbreviations ix

1 Introduction 1

2 Gamma-ray Bursts 4
2.1 History . . . 4
2.2 The GRB Fireball Model . . . 7
2.3 Neutrino Emission in the Fireball Model . . . 9
2.4 Neutrino Spectrum Calculation . . . 13

3 The IceCube Detector 17
3.1 Detection Principle . . . 17
3.1.1 Neutrino Interaction . . . 21
3.1.2 South Pole Ice . . . 24
3.2 The Detector . . . 26
3.3 The Digital Optical Module . . . 30
3.4 Online Systems . . . 32
3.5 Calibration . . . 37
3.5.1 Timing Calibration . . . 37
3.5.2 DOM Calibration . . . 39
3.5.3 Geometry Calibration . . . 41
3.6 Backgrounds . . . 41
3.7 Simulated Data . . . 44
3.8 Effective Area . . . 46

4 GRB Selection 49
4.1 Gamma-ray Burst Coordinate Network . . . 49
4.2 Satellites . . . 50
4.2.1 Swift . . . 50
4.2.2 Third Interplanetary Network . . . 52
4.3 IceCube GRB Filter . . . 54
4.4 GRB Neutrino Spectra Calculation . . . 55

5 Reconstruction Techniques 65
5.1 Hit Preparation . . . 65
5.1.1 DOM Readout Cleaning . . . 65
5.1.2 DOM Calibration . . . 66
5.1.3 Feature Extraction . . . 68
5.1.4 Time Window Hit Cleaning . . . 68

5.2 Maximum Likelihood Reconstruction . . . 69
5.2.1 The Likelihood Function . . . 70
5.2.2 The Pandel Function . . . 72
5.2.3 Forming the PDF . . . 73
5.2.4 Implementation . . . 74
5.3 Specific Reconstructions Used . . . 75
5.3.1 LineFit . . . 75
5.3.2 Single Photoelectron Fits . . . 76
5.3.3 Multiple Photoelectron Fit . . . 77
5.3.4 Paraboloid Fit . . . 78
5.3.5 Bayesian Up/Down Fit . . . 79
5.3.6 Umbrella Fit . . . 81
5.3.7 Split Reconstruction . . . 81
5.3.8 Energy Reconstruction . . . 82

6 Analysis Techniques 84
6.1 Support Vector Machines . . . 84
6.1.1 Linearly Separable Case . . . 85
6.1.2 Non-Separable Linear Case . . . 88
6.1.3 Non-Linear Case . . . 89
6.2 Model Discovery Factor . . . 90
6.3 Unbinned Likelihood Method . . . 93

7 Northern Hemisphere Search 96
7.1 GRB Triggers . . . 96
7.2 IceCube Data . . . 97
7.2.1 Background . . . 97
7.2.2 Simulation . . . 97
7.2.3 Processing . . . 98
7.3 Support Vector Machine . . . 100
7.4 Angular Cuts . . . 105
7.5 Cut Optimization . . . 107
7.6 Error Estimations . . . 108
7.6.1 Background Error . . . 108
7.6.2 Signal Error . . . 110
7.7 Results . . . 114

8 Southern Hemisphere Search 116
8.1 IceCube Data . . . 116
8.1.1 Triggered Data . . . 117
8.1.2 Filtered Data . . . 117
8.1.3 Simulation . . . 119
8.2 Support Vector Machine . . . 121
8.3 Unbinned Likelihood Method . . . 122
8.4 Iterations . . . 132

8.5 Error Estimations 133
8.6 Results 133

9 Summary and Outlook 141

Bibliography 142

List of Tables

3.1 Filter Rates 36

4.1 Satellite Parameters 54

4.2 Burst Parameters 59

4.3 Burst Spectrum Parameters 61

7.1 On-Time Event Rates 100

7.2 Expected Background Errors 110

7.3 Expected Signal Errors 114

8.1 GRB Localization Errors 127

8.2 GRB070925 Event Parameters 134

List of Figures

2.1 The BATSE Skymap 5

2.2 Durations of BATSE GRBs 6

2.3 GRB γ and ν Emission 11

3.1 The IceCube Detector 18

3.2 An IceCube Event 19

3.3 An IceCube Event (continued) 20

3.4 Feynman Diagrams for Neutrino Interactions 21

3.5 Muon Energy Loss in Ice 23

3.6 Ice Properties 25

3.7 IceCube Schematic 26

3.8 IceCube Detector Layout 29

3.9 IceCube DOM 30

3.10 PnF System 33

3.11 Timing Waveforms 38

3.12 DOM Charge Histogram 40

3.13 IceCube Backgrounds 42

3.14 Atmospheric Neutrino Flux 44

3.15 Trigger Level Data/Simulation Comparisons 47

3.16 IceCube Effective Area 48

4.1 The Swift Observatory 51

4.2 Example IceCube Stability Plots 56

4.3 GRB Neutrino Spectra 58

5.1 DOMcalibrator Droop Correction 67
5.2 Reconstruction Coordinate System 71
5.3 Pandel Function 73
5.4 Paraboloid Pull Plots 80

6.1 Linearly Separable SVM 85
6.2 Non-separable Linear SVM 89
6.3 Least Detectable Signal 92

7.1 Cut power at level 3 99
7.2 Level 3 Quality Parameters 100
7.3 Level 4 Quality Parameters (1) 102
7.4 Level 4 Quality Parameters (2) 103
7.5 SVM Settings Grid Search 104
7.6 Final SVM Classifier 106
7.7 Angle Cuts 107
7.8 MDF vs. SVM classifier cut 109
7.9 Background Distribution 111
7.10 Simulation Discrepancies 112
7.11 Northern Hemisphere Flux Upper Limit 115

8.1 Trigger Level Cut Efficiency 118
8.2 Parameterized Energy Cuts 120
8.3 Triggered Dataset Quality Parameters (1) 123
8.4 Triggered Dataset Quality Parameters (2) 124
8.5 Filtered Dataset Quality Parameters (1) 125
8.6 Filtered Dataset Quality Parameters (2) 126

8.7 Example Time PDF 128
8.8 Background Space PDFs 129
8.9 Support Vector Machine PDFs 130
8.10 Unbinned Likelihood λ Distributions 131
8.11 Burst Significances 134
8.12 GRB070925 Event 135
8.13 On-Time Events (1) 137
8.14 On-Time Events (2) 138
8.15 On-Time Events (3) 139
8.16 On-Time Events (4) 140
8.17 Southern Hemisphere Burst Flux Limits 140

List of Abbreviations

AMANDA	Antarctic Muon and Neutrino Detector Array
ATWD	Analog Transient Waveform Digitizer
BAT	Burst Alert Telescope
BATSE	Burst and Transient Source Explorer
CGRO	Compton Gamma-ray Observatory
DAQ	Data Acquisition System
DOM	Digital Optical Module
fADC	Fast Analog to Digital Converter
FPGA	Field-Programmable Gate Array
GBM	Gamma-ray Burst Monitor
GCN	Gamma-ray Burst Coordinate Network
GRB	Gamma-ray Burst
HETE-2	High-Energy Transient Explorer
IPN3	Third Interplanetary Network
LC	Local Coincidence
LED	Light Emitting Diode
PDF	Probability Distribution Function
PE	Photo-Electron
PMT	Photo-Multiplier Tube
PnF	Processing and Filtering
MDF	Model Discovery Factor
MMC	Muon Monte Carlo
MPE	Multiple Photo-Electron
RAPCal	Reciprocal Active Pulsing
RBF	Radial Basis Function
SMT	Simple Majority Trigger
SPADE	South Pole Archival and Data Exchange
SPE	Single Photo-Electron
SVM	Support Vector Machine
UVOT	Ultra-Violet/Optical Telescope
XRT	X-Ray Telescope

Chapter 1

Introduction

The discovery of neutrinos in correlation with gamma-ray bursts (GRBs) would be a momentous achievement for multi-messenger astrophysics. Neutrino observations would identify GRBs as a source of the highest energy cosmic rays, would be a major step forward in our understanding of hadronic and leptonic processes in GRB jets, and would further facilitate the exploration of the high redshift Universe.

This thesis describes a first search with the IceCube detector for this neutrino emission. A binned stacked northern hemisphere search is done which is modelled after previous analyses done with the Antarctic Muon and Neutrino Detector Array (AMANDA), a prototype for the IceCube detector. A machine learning algorithm is introduced as an analysis technique that improves separation of signal and background and thus sensitivity. A search for muon neutrinos coincident with southern hemisphere bursts is also done in a first attempt to extend IceCube's sensitivity in the higher background region above the horizon. This search also incorporates new analysis techniques such as a method to avoid strict angle cuts around GRBs.

Searches for neutrinos of this kind have previously been done [1] [2]. A search done with AMANDA included 400 burst triggers from the Burst and Transient Source Explorer (BATSE) and set a very strict limit on the muon neutrino flux from GRBs [3]. The current size of IceCube and number of GRB triggers can not

provide a better limit than this, but the sensitivity of the growing IceCube detector will quickly surpass that of previous searches in the years to come.

This thesis is organized as follows:

- Chapter 2 describes the history of GRBs, lays out the leading model for gamma-ray emission, outlines how neutrino emission fits into this model, and provides equations for calculating the neutrino flux from an individual burst.
- Chapter 3 describes the IceCube detector, the physical principles of how it detects astrophysical neutrinos, its building block, the Digital Optical Module, and its data, real and simulated.
- Chapter 4 lists the GRB triggers used in this thesis and also briefly describes the satellites and detectors that provide those triggers, lists the measured parameters used in the calculation of the neutrino spectra of these bursts, and describes IceCube's online response to the GRB triggers.
- Chapter 5 details how IceCube data is processed and the algorithms used to reconstruct an event direction, energy, and other quality parameters.
- Chapter 6 describes various analysis techniques used in this thesis including Support Vector Machines, the Model Discovery Factor, and an unbinned likelihood method.
- Chapter 7 describes a binned and stacked analysis of IceCube data taken during 41 GRBs in the northern hemisphere.

- Chapter 8 describes 40 individual unbinned analyses of IceCube data taken during GRBs in the southern hemisphere.

- Chapter 9 puts the results of this study into perspective and describes the prospects for future detection.

Chapter 2

Gamma-ray Bursts

Gamma-ray bursts (GRBs) are among the most energetic phenomena in the universe. They are short bursts of keV/MeV radiation, occurring with a rate of few per day uniformally distributed in the sky. During the burst, they outshine all other sources in the gamma-ray sky, including the sun. The energy output of a single GRB in keV/MeV gamma-rays is comparable to that of the entire Milky Way galaxy over a few years.

2.1 History

The first GRB was detected in 1967 by the Vela satellites [4], whose purpose was to monitor for violations of the nuclear test ban treaty. The detection of the first GRBs was immediately classified and was not made public until seven years later. There were a number of other instruments for detecting GRBs in the years to follow, but the next major breakthrough did not occur until 1991 when the Compton Gamma-Ray Observatory (CRGO) [5] was launched carrying the Burst and Transient Source Explorer (BATSE) [6]. BATSE was sensitive to gamma-rays in the 15 keV - 2 MeV range and had a wide field of view which enabled it to detect 2704 GRBs through 2000 [7]. This large number of detections revealed new information about the nature of GRBs.

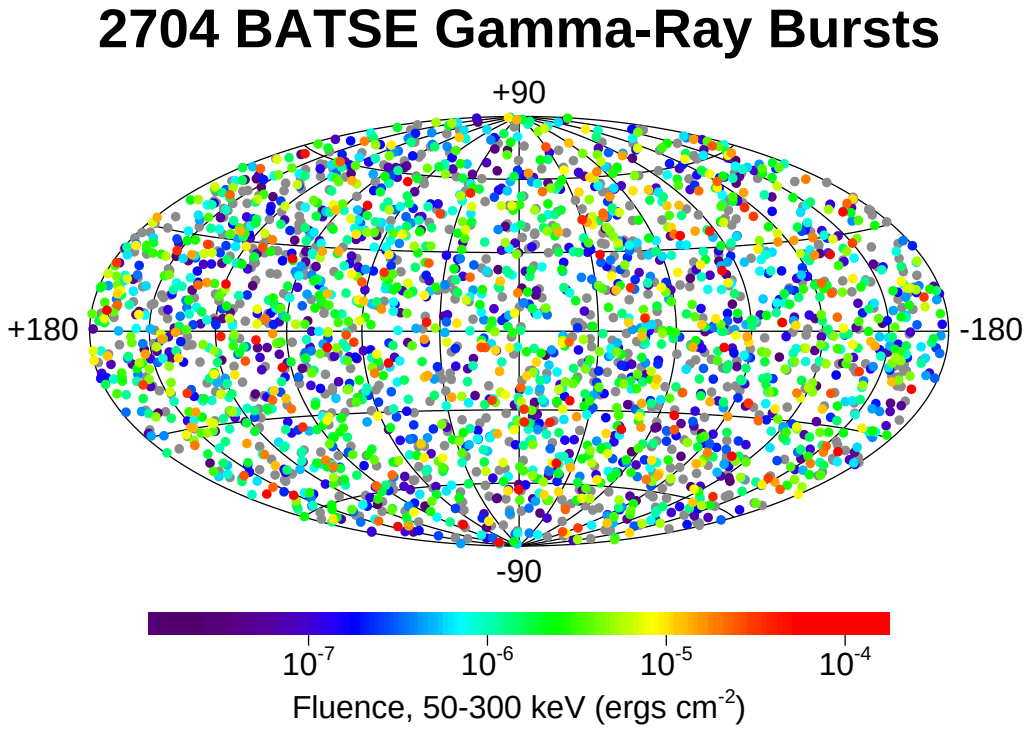

Figure 2.1: Locations of all the 2704 GRBs detected by BATSE in galactic coordinates. The isotropic distribution of GRBs in space implied that GRBs are most likely cosmological sources. Taken from [6]

The isotropic distribution of the BATSE detections (figure 2.1) strongly implied that GRBs originate from cosmological distances further away than our local group of galaxies. The distribution of GRB durations (T_{90} which is the time in which a burst emits 90% of its counts) showed two populations of GRBs (figure 2.2). Bursts were divided into two categories: "short bursts" having $T_{90} \leq 2$ seconds and "long bursts" having $T_{90} \geq 2$ seconds. The spectral properties of these two categories of GRBs were found to be different in that short bursts were generally harder (more high energy counts compared to low energy counts) than long bursts.

In 1996, the BeppoSAX satellite was launched [8]. This detector provided

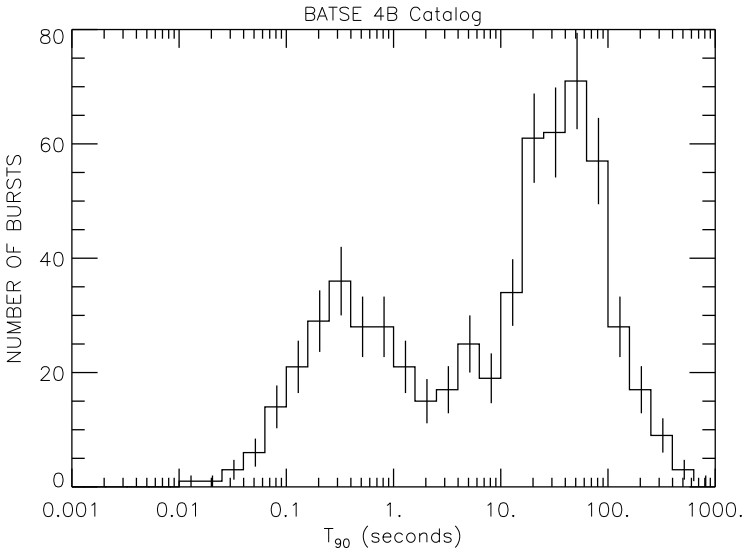

Figure 2.2: Duration (T_{90}) distribution of the GRBs detected by BATSE. Two populations of bursts, separated at $T_{90} \approx 2$ seconds, can be seen. Taken from [6]

localizations accurate enough for follow-up ground-based observations in optical, radio, and other wavelengths. These observations revealed afterglow emission that faded and moved to lower wavelengths for up to hours or even days after the initial GRB emission [9]. This also allowed the identification of host galaxies and thus redshift measurements, absolutely confirming GRB's extra-galactic origin. The High-Energy Transient Explorer (HETE-2) was launched in 2000 [10]. It provided more afterglow observions and also connected long GRBs with Type Ic supernovae [11].

The Swift satellite was launched in 2004 (section 4.2.1). Swift combined a GRB detector with an X-ray and optical/ultraviolet telescope, and the ability to automatically point those telescopes at a recently detected GRB within one minute. This allowed a deeper investigation into the transition from the energetic and chaotic prompt emission to the smoothly decaying softer afterglow. Swift also observed

afterglows of short bursts for the first time, and strengthened the case for two different progenitors for short and long bursts: compact-object binaries for short GRBs versus the collapse of massive stars for long GRBs.

The Fermi Gamma-ray Space Telescope was launched in June 2008 [12]. The on-board Gamma-ray Burst Monitor (GBM) is sensitive to GRBs from anywhere in the sky not blocked by the Earth. Although the GBM will not be able to provide burst coordinates with the precision of Swift, it's wide field of view will allow it to detect many more bursts. Its wide range of energy sensitivity will hopefully also provide more clues to the origins of GRBs in the coming years.

2.2 The GRB Fireball Model

The ultimate energy source of GRBs is convincingly associated with a cataclysmic energy release in stellar mass objects. For long bursts, this is almost certainly associated with the core collapse of a massive star [13]. For short bursts, it is believed to be the merger of two compact objects [14]. In both cases, gravitational energy is liberated and augmented by the continued infall or accretion of gas onto the central object. Material along the rotational axis of the progenitor falls in quickly and material on the equatorial plane falls in slowly due to strong centripetal acceleration. The result is a rotating disc surrounding the progenitor.

An explosion occurs on the poles of the compact object when the building outward pressure overcomes the pressure from the infalling material. A fraction of the total energy of this explosion remains trapped in a e^-, e^+, and γ fireball which

expands in the form of a collimated jet. This expansion is highly relativistic due to a small baryon load ($M_B c^2 \ll E$ where M_B is the total mass of the baryons and E is the total energy of the fireball). The baryons are believed to be protons that are accelerated along with the other charged particles. If present, they would directly result in the neutrino emission explained in the following sections. Early on, the density of the jet is very high, and because of this, any radiation in the fireball is absorbed. At some point, the optical depth is reduced enough that radiation can escape.

The spectrum of the prompt gamma-ray emission is a broken power law with great variability. This implies that a smoothly expanding fireball radiating a thermal spectrum cannot be the case. A natural way to achieve a non-thermal spectrum is by having the kinetic energy of the flow re-converted into random energy via internal [15] and external [16] shocks. The internal shocks happen inside the jet between shells of material moving with different velocities. During these shocks, electrons are accelerated to ultra-relativistic velocities [17] and give off the prompt gamma-ray emission via synchrotron radiation. The external shocks occur when the jet collides with the ambient interstellar medium, and smoothly and slowly decelerates. The external shocks are thought to be responsible for the fading afterglow emission.

The prompt GRB photon spectrum, $dN_\gamma/dE_\gamma(E_\gamma)$, can be modelled experimentally by the Band function [18]:

$$\frac{dN_\gamma}{dE_\gamma}(E_\gamma) = A \begin{cases} \left(\frac{E_\gamma}{100keV}\right)^{-\alpha_\gamma} e^{(-E_\gamma/E_0)} & E_\gamma \leq \epsilon_\gamma^b \\ \left(\frac{E_\gamma}{100keV}\right)^{-\beta_\gamma} \left[\frac{(\beta_\gamma-\alpha_\gamma)E_0}{100keV}\right]^{\beta_\gamma-\alpha_\gamma} e^{-(\beta_\gamma-\alpha_\gamma)} & E_\gamma > \epsilon_\gamma^b \end{cases} \tag{2.1}$$

Here, E_γ is the photon energy, E_0 is the reference energy with $\epsilon_\gamma^b = (\beta_\gamma - \alpha_\gamma) \cdot E_0$

as the break energy in the photon spectrum. There are two approaches to explain the break in the spectrum at a break energy typically $\epsilon_\gamma^b \sim 250$ keV. The most common explanation is the steepening of the spectrum by one power due to cooling of electrons at high energies. The break can also be explained by assuming an inverse Compton scattering scenario. For a regular GRB, the spectral indices are usually distributed around average values of $\alpha_\gamma \sim 1$ and $\beta_\gamma \sim 2$, but these values can scatter over a wide range. Short GRBs tend to have harder spectra with $\alpha_\gamma \sim 0$ and $\beta_\gamma \sim 1$.

The energy range of detection may not cover both parts of the spectrum, and thus in most cases, simpler fits are used. In this thesis, the photon spectra of various bursts are parameterized by a broken power law.

$$F_\gamma(E_\gamma) = E_\gamma \cdot \frac{dN_\gamma}{dE_\gamma} = f_\gamma \times \begin{cases} \epsilon_\gamma^{b\,(\alpha_\gamma - \beta_\gamma)} E_\gamma^{-\alpha_\gamma} & E_\gamma < \epsilon_\gamma^b \\ E_\gamma^{-\beta_\gamma} & E_\gamma \geq \epsilon_\gamma^b \end{cases} \tag{2.2}$$

where f_γ can be determined by integrating the photon spectrum over the range of detection, and setting this equal to the measured fluence.

This is a general description of the current understanding of GRB physics. For extensive reviews on the subject, see [19] [20] [21] and the references therein.

2.3 Neutrino Emission in the Fireball Model

Models exist that describe neutrino emission during three phases of a GRB: *precursor* or before gamma-ray emission, *prompt* or during gamma-ray emission, and *afterglow* or neutrinos produced when the shock fronts hit the interstellar medium.

This thesis describes a search for prompt emission. The neutrino and corresponding photon fluxes during all three phases are shown in figure 2.3.

The dominant process for neutrino production in all the above situations is photo-hadronic reactions. Protons present in the fireball produce parent pions via the processes:

$$p\gamma \rightarrow \Delta \rightarrow n\pi^{+} \tag{2.3}$$

$$p\gamma \rightarrow \Delta \rightarrow p\pi^{0} \tag{2.4}$$

which have cross sections of $\sigma_{\Delta} \sim 5 \times 10^{-28}$ cm^2. The charged pions subsequently decay producing charged leptons and neutrinos by:

$$\pi^{+} \rightarrow \nu_{\mu}\mu^{+} \rightarrow \nu_{\mu}e^{+}\nu_{e}\overline{\nu}_{\mu} \tag{2.5}$$

while the neutral pions decay into high energy photons.

Waxman and Bahcall have postulated a model of prompt neutrino emission [23] [24]. The model states that physical conditions in the fireball imply that protons may be Fermi accelerated in this region to energies $> 10^{20}$ eV. The spectrum and flux of ultra-high energy cosmic rays above 10^{19} eV are consistent with those expected from Fermi acceleration of protons in cosmological GRBs. A burst of $\sim 10^{14}$ eV neutrinos created by the photo-hadronic interactions described above is thus a natural consequence of the fireball model.

In this thesis, that prompt neutrino flux is parameterized as:

$$F_{\nu}(E_{\nu}) = f_{\nu} \times \begin{cases} {\epsilon_{\nu}^{b}}^{(\alpha_{\nu}-\beta_{\nu})} E_{\nu}^{-\alpha_{\nu}} & E_{\nu} < \epsilon_{\nu}^{b} \\ E_{\nu}^{-\beta_{\nu}} & \epsilon_{\nu}^{b} < E_{\nu} < \epsilon_{\nu}^{s} \\ {\epsilon_{\nu}^{s}}^{2} E_{\nu}^{-(\beta_{\nu}+2)} & E_{\nu} > \epsilon_{\nu}^{s} \end{cases} \tag{2.6}$$

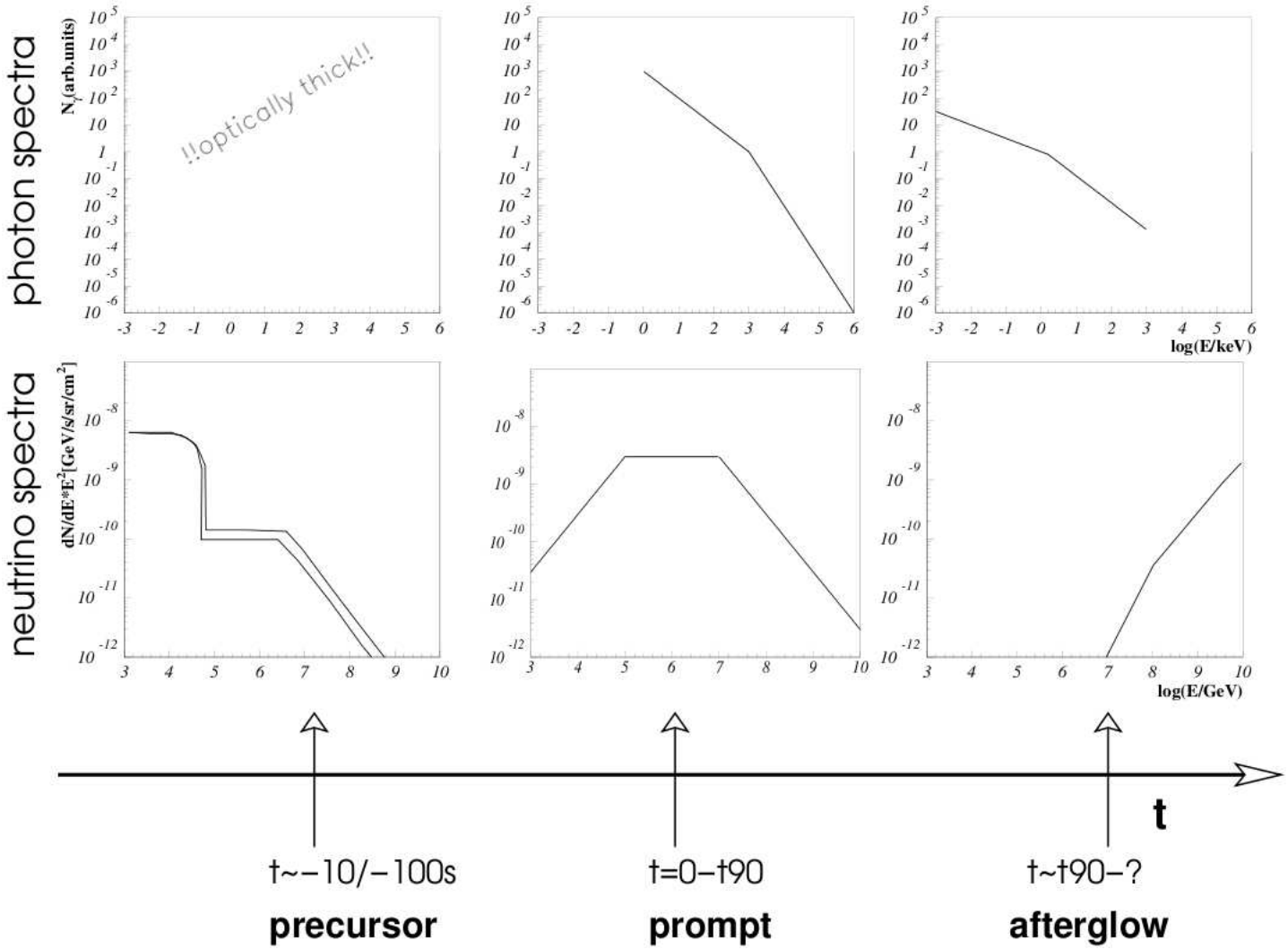

Figure 2.3: Overview of different neutrino production scenarios during the three different phases of a GRB. The corresponding electromagnetic output is indicated schematically as well. Taken from [22].

The calculation in [24] used assumed average parameters and resulted in the following parameters:

$$\begin{aligned} f_\nu &= 3 \cdot 10^{-9} \text{ GeV cm}^{-2} \text{ s}^{-1} \text{ sr}^{-1} \\ \alpha_\nu &= 3 \\ \beta_\nu &= 2 \\ \epsilon_\nu^b &= 10^5 \text{ GeV} \\ \epsilon_\nu^s &= 10^7 \text{ GeV} \end{aligned} \tag{2.7}$$

This is referred to as the average Waxman-Bahcall spectrum throughout the rest of this thesis and it is shown in figure 2.3. Section 2.4 shows more details of this calculation done with individual burst parameters.

The precursor model postulates that a shock forms when the pre-GRB matter collides with the wind of the central engine [25]. At this point, the burst is still opaque to photon emission and the shock environment yields a good target for neutrino production by shock-accelerated protons interacting with thermal X-rays in the sub-stellar jet cavity. The shocks happen at smaller radii than the prompt emission and at lower boost factors. The flux at energies $E_\nu > 10^5$ GeV originates from the $p\gamma$ interactions described above. The low energy part of the neutrino spectrum results from pp interactions and is E_ν^2 shaped. As in the $p\gamma$ interactions, the neutrinos from these pp reactions result from secondary pion decays. The two lines in the lower left panel of 2.3 represent different shock/jet radii and envelope mass settings.

Afterglow neutrinos are produced when the internal shocks from the original

fireball hit the interstellar medium and produce external shocks [26]. As with the prompt emission, the synchrotron emission of electrons gives evidence for the existence of relativistic charged particles which in turn implies neutrino production by the baryonic component of the jet and the photon field. In the case of afterglow emission, Waxman and Bahcall predict the acceleration of ultra high-energy protons ($E_p > 10^{20}$ eV) in reverse, mildly relativistic shocks. The acceleration of protons to such high energies implies the production of neutrinos in $p\gamma$ interactions in environments optically thick to the results of $p\gamma$ or pp interactions. Waxman and Bahcall conclude that a significant neutrino flux during the afterglow phase is directly correlated to the electromagnetic afterglow emission.

2.4 Neutrino Spectrum Calculation

The average Waxman-Bahcall neutrino spectrum calculation in [24] uses some average GRB parameters whose values are based on assumptions taken from the BATSE burst population. However, burst parameters can vary significantly from burst to burst and the GRB population used in this thesis (mostly observed by the Swift satellite) is qualitatively different from the BATSE population. Therefore, the measured parameters from each burst are used to calculate the neutrino spectra individually. For parameters that have not been measured, average values are used. The calculation closely follows those in [27] and [22].

To first arrive at the parameterization in equation 2.6, the original photohadronic processes are considered. In those processes, the resulting neutrino energy

is proportional to the proton energy.

$$E_\nu = \frac{1}{4}\langle x_{p\to\pi}\rangle E_p \tag{2.8}$$

The $\langle x_{p\to\pi}\rangle \simeq 0.2$ factor represents the average fraction of energy transferred from the proton to the pion. The factor of 1/4 comes from the assumption that the four resulting leptons share an equal portion of the pion energy. Because the energy of the Δ mass has to be produced in the center of mass system, the product of the proton and photon energy remains constant. This implies that the photon and neutrino energy are inversely proportional, $E_\nu \propto E_\gamma^{-1}$. For each proton energy, the resulting neutrino spectrum traces the broken power law spectrum of photons:

$$F_\nu(E_\nu) \propto \begin{cases} E_\nu^{-\alpha_\nu} & E_\nu \leq \epsilon_\nu^b \\ E_\nu^{-\beta_\nu} & \epsilon_\nu^b < E_\nu \leq \epsilon_\nu^s \end{cases} \tag{2.9}$$

where the photon spectral indices can be used to describe $\alpha_\nu = 3 - \beta_\gamma$ and $\beta_\nu = 3 - \alpha_\gamma$.

The break energy in the spectrum, ϵ_ν^b, can be related to photon break energy, ϵ_γ^b, by considering the minimal energy necessary to produce a Δ-resonance in the shock fronts of the bursts. That minimal energy is:

$$E_p' \geq \frac{m_\Delta^2 - m_p^2}{4E_\gamma'} \tag{2.10}$$

where primes indicate quantities measured in the co-moving frame. Using equation 2.8, the first break energy can be written down as:

$$\begin{aligned} \epsilon_\nu^b &= \frac{(m_\Delta^2 - m_p^2)\cdot\Gamma^2}{4\cdot(1+z)^2\cdot\epsilon_\gamma^b} \\ &= 7.5\times10^5 \text{ GeV } \frac{1}{(1+z)^2}\left(\frac{\Gamma}{10^{2.5}}\right)^2\left(\frac{\text{MeV}}{\epsilon_\gamma^b}\right) \end{aligned} \tag{2.11}$$

where z is the redshift of the source and Γ is the bulk Lorentz factor of the shock fronts.

A second break at $E_\nu = \epsilon_\nu^s$ appears in the neutrino spectrum which is caused by synchrotron radiation of the neutrino-producing pions. Pions with sufficiently high energies suffer synchrotron losses before decaying and do not produce neutrinos. Thus, the high energy tail of the neutrino spectrum is steepened by two powers:

$$F_\nu(E_\nu) \propto E_\nu^{-(\beta_\nu+2)} \text{ for } E_\nu > \epsilon_\nu^s \tag{2.12}$$

The second break energy occurs when the pion lifetime, $\tau'_\pi \approx 2.6 \times 10^{-8} E'_\pi/(m_\pi c^2)$ seconds, becomes comparable to the synchrotron loss time

$$t'_{syn} = \frac{3 m_\pi^4 c^3}{4 \sigma_T m_e^2 E_\pi U'_B} \tag{2.13}$$

where $\sigma_T = 0.665 \times 10^{-24}$ cm^2 is the Thomson cross section and $U'_B = B'^2/8\pi$ is the energy density of the magnetic field in the shocked fluid. Using fireball kinematics, this term can be related to, among others, f_e and f_b, which are the fraction of the burst's internal energy going into electrons and the magnetic fields respectively. Other terms included are variability of the gamma-ray flux t_{var}, which is used as a measure for the time between the emission of two consecutive shells and the isotropic equivalent luminosity, L_γ^{iso}. This is given by the isotropic equivalent energy released in gamma-rays, E_{iso}, divided by the burst duration. It should be noted that the isotropic luminosity is always used in conjunction with a 4π geometry. Hence, a reduction of the true total luminosity of the burst due to a narrow opening angle of the jet cancels with the reduced geometry factor.

After relating the pion lifetime and synchrotron loss time, the second break energy is:

$$\epsilon_\nu^s = \sqrt{\frac{3\pi f_e}{4\tau_\pi^0 \sigma_T f_b L_\gamma^{iso}}} \cdot \frac{c^4 t_{var}}{(1+z)\cdot m_e}\Gamma^4 \tag{2.14}$$
$$= 10^7 \text{ GeV } \frac{1}{1+z}\sqrt{\frac{f_e}{f_b}}\left(\frac{\Gamma}{10^{2.5}}\right)^4\left(\frac{t_{var}}{0.01s}\right)\sqrt{\frac{10^{52}\text{ erg s}^{-1}}{L_\gamma^{iso}}}$$

with the pion lifetime at rest $\tau_\pi^0 = 2.6 \times 10^{-8}$ s. The muon lifetime is about a factor of 100 higher than the pion lifetime, which gives a lower energy threshold for synchrotron losses for $\overline{\nu}_\mu$ and ν_e.

The resulting neutrino spectrum is normalized to the gamma-ray fluence F_γ which is assumed to be proportional to the neutrino luminosity. The gamma-ray fluence is thus integrated, adjusted by some factors, and set equal to the integration of the neutrino spectrum:

$$\int_0^\infty dE_\nu F_\nu(E_\nu) = \frac{1}{8}\frac{1}{f_e}(1-(1-\langle x_{p\to\pi}\rangle)^{N_{int}})\int_0^\infty dE_\gamma F_\gamma(E_\gamma) \tag{2.15}$$

with

$$N_{int} = \left(\frac{L_\gamma^{iso}}{10^{52}\text{ erg s}^{-1}}\right)\left(\frac{0.01\text{ s}}{t_{var}}\right)\left(\frac{10^{2.5}}{\Gamma}\right)^4\left(\frac{\text{MeV}}{\epsilon_\gamma^b}\right) \tag{2.16}$$

The factor of 1/8 is present because half of the photo-hadronic interactions result in four leptons. The $1/f_e$ factor accounts for the fraction of total energy in electrons compared to protons in the jet. The $(1-(1-\langle x_{p\to\pi}\rangle)^{N_{int}})$ factor represents the fraction of energy transferred to the pions and limits it to 1. $\langle x_{p\to\pi}\rangle$ is again the average fraction of proton energy transfered to a pion in a single average interaction.

Chapter 3

The IceCube Detector

Neutrinos are very difficult to detect because they interact weakly. Therefore, very large detectors must be constructed to see them. Various cosmological neutrino sources predict an observable number of events in a kilometer scale detector [28], and thus motivate the construction of IceCube [29] [30].

The IceCube neutrino detector consists of an array of photomultiplier tubes buried deep in the dark Antarctic ice. These tubes detect the Cherenkov radiation from neutrino induced muons. The pattern of this detected light is used to reconstruct the direction of the muon and thus the neutrino. When completed, IceCube's size will allow unprecedented sensitivity to cosmological neutrinos. Figure 3.1 shows a colorful representation of the detector along with an example neutrino reaction and Cherenkov cone. Figures 3.2 and 3.3 show a visualization of the pattern of detected light from the same example higher energy event in the 22-string detector.

3.1 Detection Principle

Neutrino detectors do not directly observe neutrinos. Cherenkov radiation is observed from secondary charged leptons created when a neutrino interacts. Because these interactions are rare, a large, clear, and dark volume must be instrumented with light sensitive equipment. In the specific case of IceCube, a large volume of

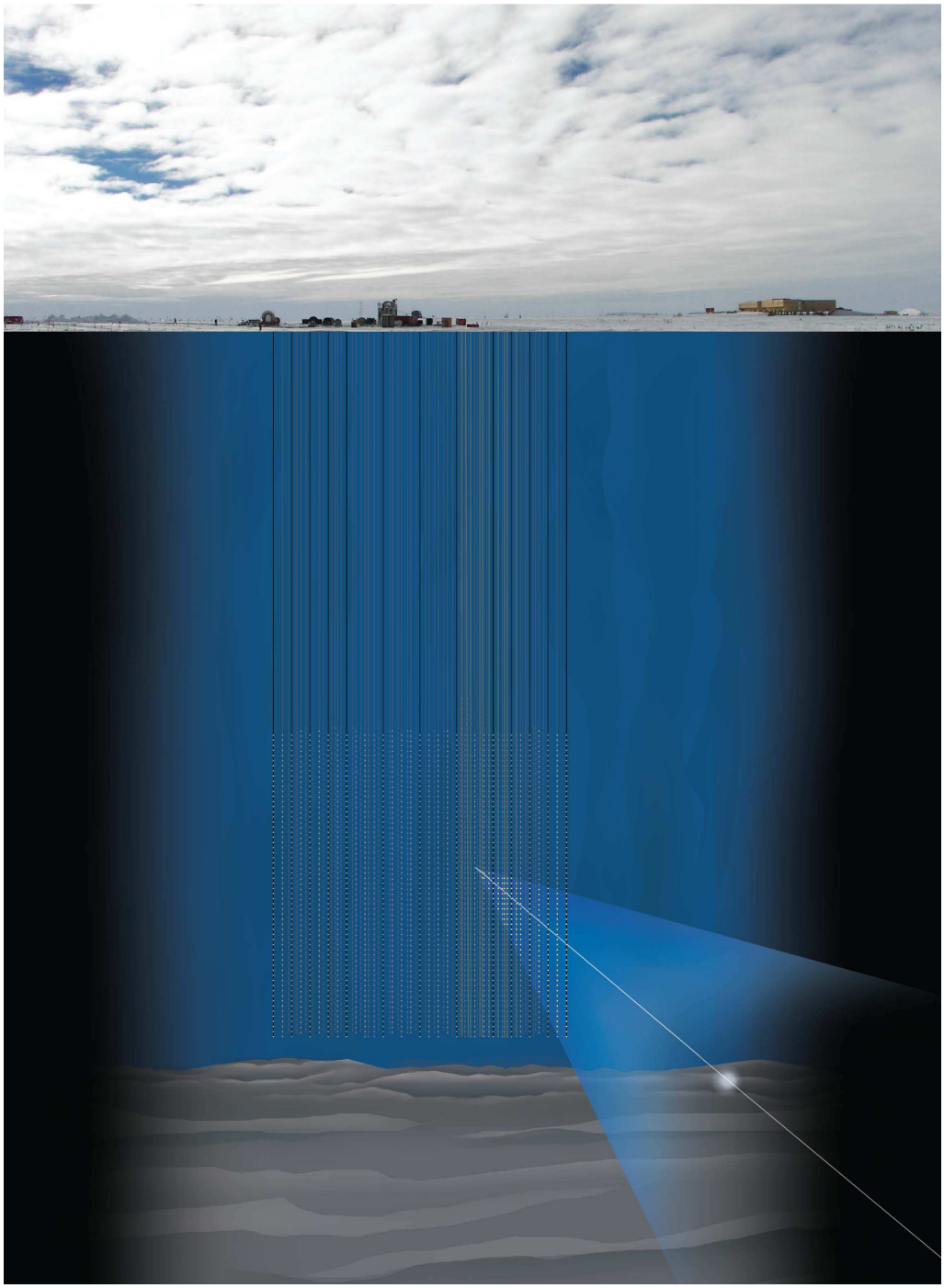

Figure 3.1: The Icecube detector is shown buried in the Antarctic ice below the South Pole. An example neutrino track interacts to form a muon in the bedrock. The muon then propagates through the detector while giving off Cherenkov radiation indicated by the cone.

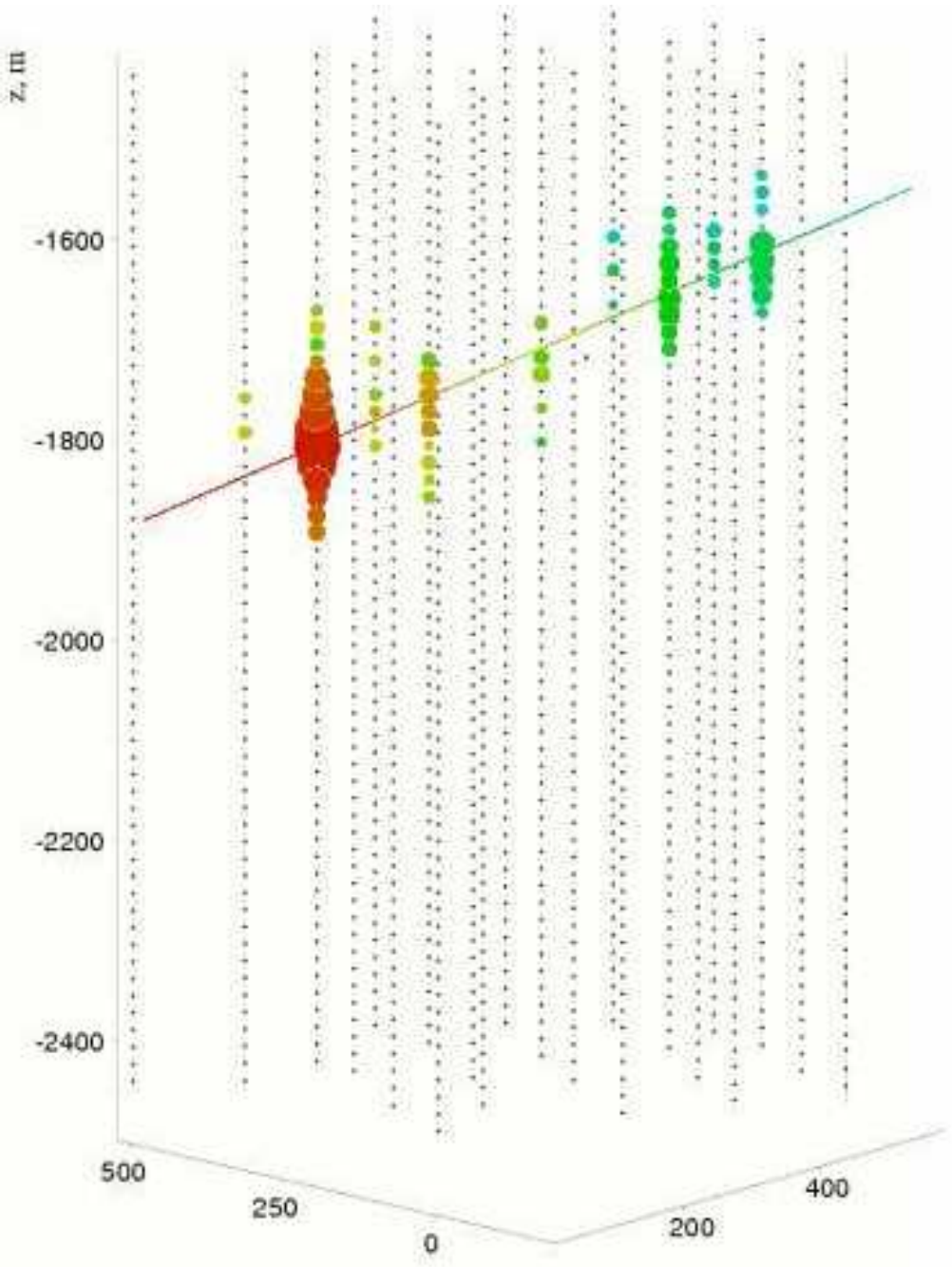

Figure 3.2: An example neutrino event in the IceCube detector. The colors show the evolution in time with early hits in red and late hits in green. The size of the circles represents the amount of deposited charge.

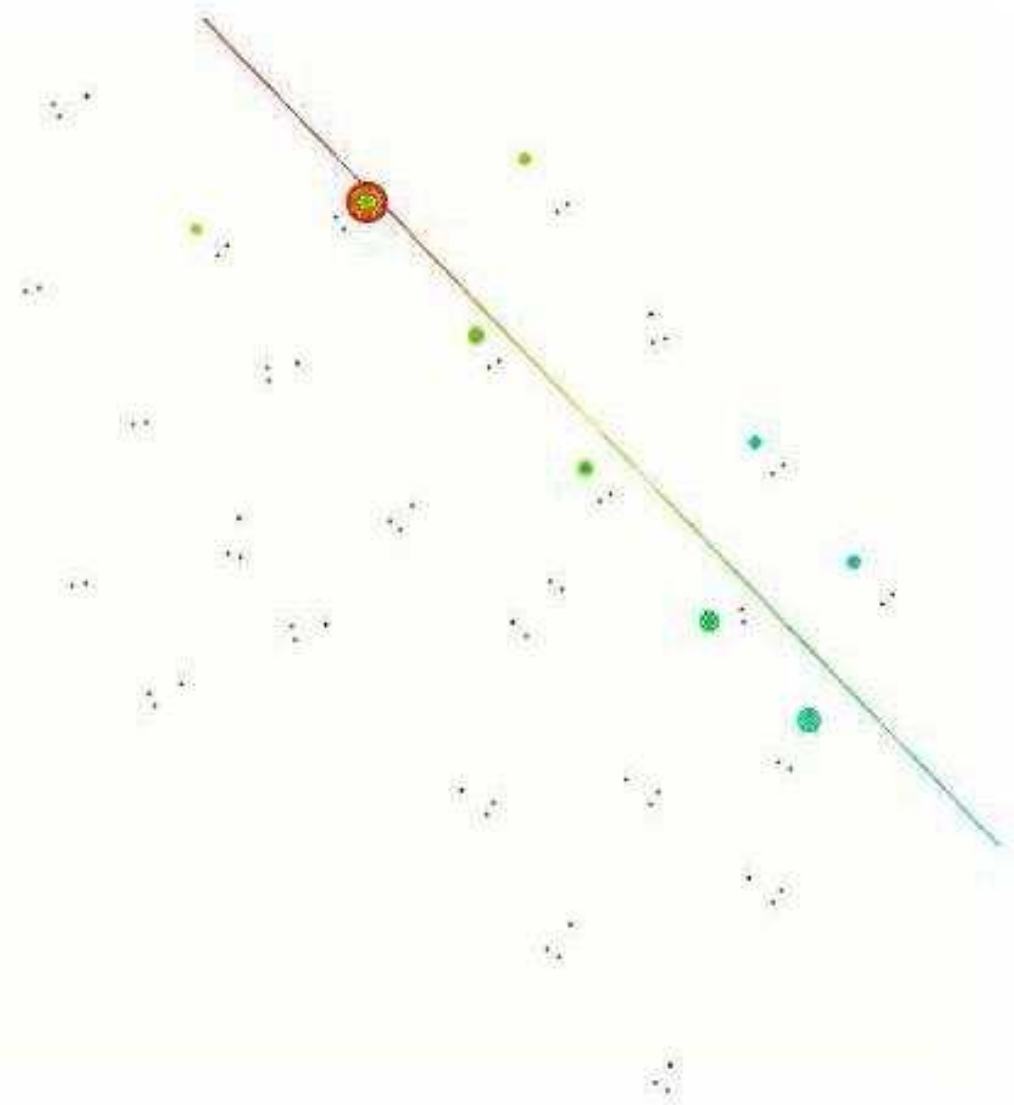

Figure 3.3: A top view of the example neutrino event in figure 3.2. The colors show the evolution in time with early hits in red and late hits in green. The size of the circles represents the amount of deposited charge.

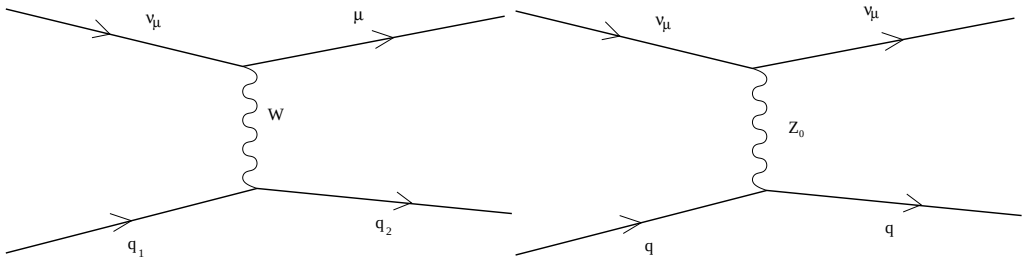

(a) Charged Current Interaction (b) Neutral Current Interaction

Figure 3.4: Feynman diagrams for two neutrino-quark interactions.

deep Antarctic ice is instrumented in order to observe this Cherenkov radiation.

3.1.1 Neutrino Interaction

The muons are the result of neutrinos interacting with nearby nucleons:

$$\nu_\mu + N \longrightarrow \mu + X, \tag{3.1}$$

The standard model of particle physics includes a three-body vertex linking a ν_μ, a μ and a $W^\pm$, and a three-body vertex involving a $W^\pm$ which can change a u quark to a d quark or vice-versa. Putting these vertices together results in the above reaction that produces a detectable muon. Also important is the neutral current interaction in which a Z_0 interacts with a quark. When they occur, these Z_0 interactions result in the neutrino losing energy to a possibly detectable hadronic cascade. Figure 3.4 shows the Feynman diagrams for both of these interactions.

Muons produced through the charged current neutrino interactions carry a significant fraction of the original neutrino energy. They then lose energy during

propagation through the ice through ionization, pair production, bremsstrahlung, and photo-nuclear interactions.

Ionization occurs as the muon scatters elastically with the surrounding electrons and protons in the ice. This energy loss is modeled by the Bethe-Bloch equation:

$$-\frac{dE}{dx} = Kz^2\frac{Z}{A}\frac{1}{\beta^2}\left[\frac{1}{2}ln\frac{2m_ec^2\beta^2\gamma^2T_{max}}{I^2}s - \beta^2 - \frac{\delta}{2}\right] \tag{3.2}$$

Of particular interest to IceCube is the *density correction* term in the Bethe-Bloch equation: $\frac{\delta}{2}$. This term weakens the energy loss. It is due to an effective weakening of the field of the muon due to the polarization of the medium. When the muon is traveling faster than the speed of light in the medium, this polarization adds coherently and some of the energy escapes as radiation at a fixed angle with respect to the path of the muon. The effect, named Cherenkov radiation after its discoverer, is useful because it is emitted uniformly along the track. As such, the Cherenkov cone can be used to reconstruct the direction of the muon. Cherenkov light is emitted at a wavelength of 420 nm and at a constant angle θ_C given by $cos(\theta_C) = \frac{1}{n\beta}$ where β is the speed of the particle in units of c, and n is the index of refraction of the medium. In ice, this angle is $\theta_C = 40.7°$.

The muons also lose energy to various stochastic processes that dominate at energies above 100 GeV (figure 3.5). Pair production is a process by which the muon interacts with an atom in the medium to produce an $e^{\pm}$ pair, which then quickly re-interacts to produce an electromagnetic shower. Bremsstrahlung is a process in which the muon interacts with a nucleus to produce gamma rays, which also results

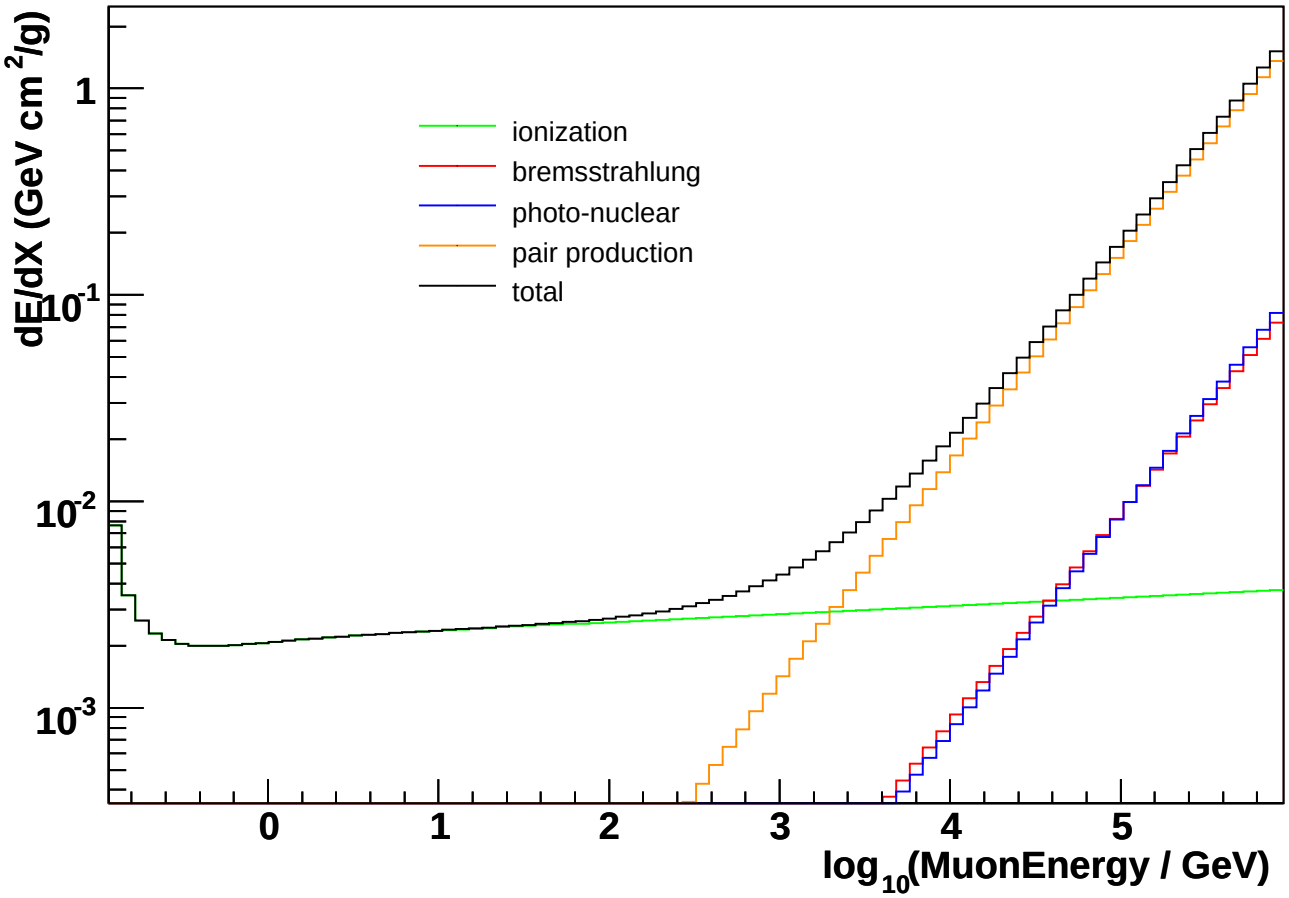

Figure 3.5: Muon energy loss in ice. Shown are the dominant energy loss mechanisms due to ionization, pair production, bremsstrahlung and photo-nuclear interactions. Ionization is dominant up to 100 GeV when stochastic energy losses take over. Obtained using MMC [31]

in an electromagnetic shower. Photo-nuclear interactions also occur when a muon interacts to produce hadrons, and these interactions produce hadronic showers as opposed to an electromagnetic ones.

Above 100 GeV, the stochastic energy loss mechanisms dominate. Because of their random nature, muons of the same energy will travel different distances in the ice. Below 100 GeV, ionization takes over as the dominant energy loss mechanism. The energy loss at this point is constant.

3.1.2 South Pole Ice

Varying geological and atmospheric conditions at the South Pole over the years resulted in different dust contamination levels at the surface. Today these buried dust layers give a depth dependence to the optical properties of the ice (figure 3.6). This depth dependence has a strong effect on the events that IceCube observes. Of particular note is the strong peak in the absorption and scattering coefficients at 2000 meters which prevent much of the light from being detected in that dust layer.

Also shown in figure 3.6 is the fact that the scattering coefficient is smaller than the absorption coefficient. In fact, for the photons emitted to Cherenkov radiation in the South pole ice, the absorption length is approximately 100 meters, but the scattering length averages around 20 meters [32]. This means that light can be seen quite far away from its source, but it's been scattered many times by the time it gets there. The muons are constantly emitting Cherenkov radiation, and thus IceCube can detect them anywhere along their substantial path length. This means

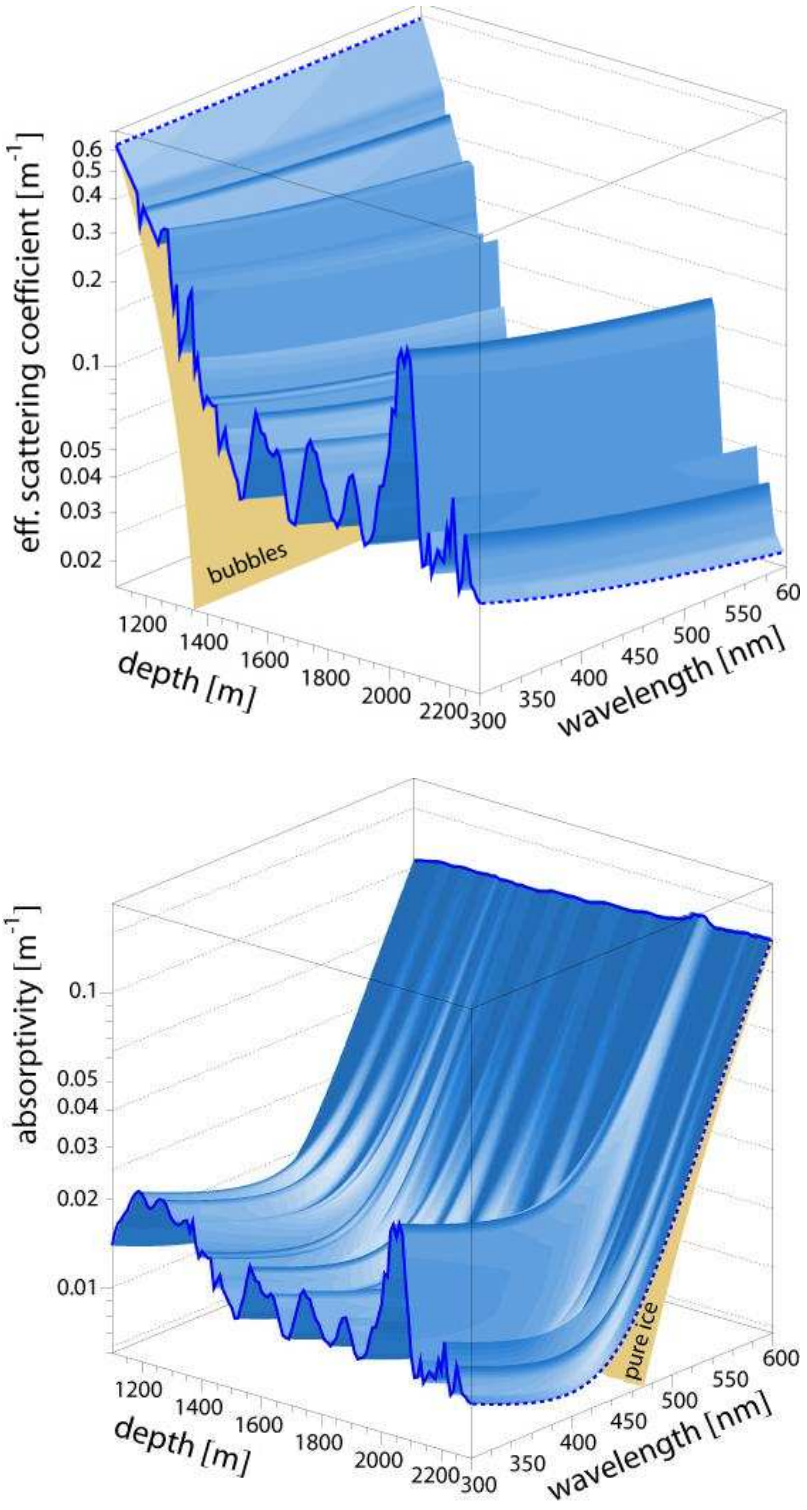

Figure 3.6: The figure on top shows the scattering in the ice as a function of depth and wavelength. The figure on the bottom shows the absorption in the ice.

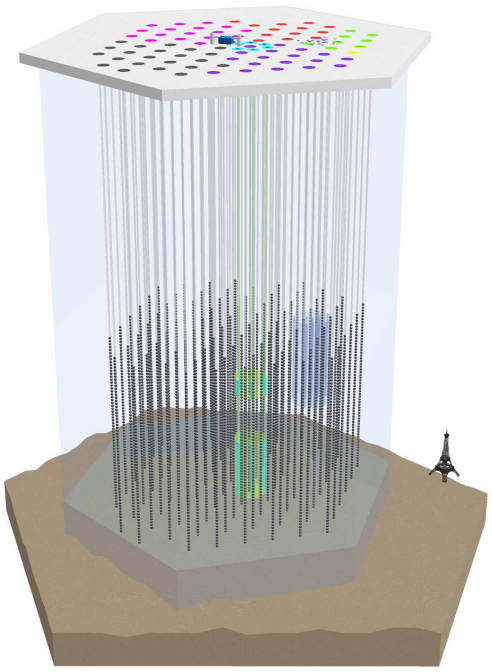

Figure 3.7: A schematic of the planned 86 string IceCube detector.

the effective detector volume is significantly larger than the actual instrumented volume.

3.2 The Detector

The IceCube detector is an array of light-sensitive Digital Optical Modules (DOMs) deployed deep below the surface of the ice at the South Pole [33] [34]. Each DOM contains a 10-inch Photo-Multiplier Tube (PMT) and electronics for acquiring and digitizing pulses from the PMT. The IceCube array is being constructed

surrounding the Antarctic Muon and Neutrino Detector Array (AMANDA) which served as a prototype for the IceCube experiment. Figure 3.7 shows the detector schematically.

To deploy DOMs in the ice, a pressurized hot water drill melts a hole in the polar ice pack. DOMs are deployed on a long cable which both supports the weight of the DOMs in the water until they freeze into place and carries power and communication to the DOM.

The detector design consists of 86 vertical strings of 60 DOMs each. The DOMs are spaced 17 meters apart on the cable that leads to the surface. DOMs are deployed starting at a depth of 1450 meters and continuing to a depth of 2450 meters. The detector is placed at this depth in order to allow downgoing muons to range out before reaching the detector and to use ice that is clearer than the ice that is near the surface. Strings are placed in a triangular grid with each string spaced 125 meters from the 6 nearest it. The spacing of the strings was the result of optimizing the geometry for the detection of TeV neutrinos. All told, the geometrical instrumented volume will be about 1 km^3.

In addition to the instrumentation below the ice, DOMs are deployed at the surface in tanks of frozen water to form an air-shower array called IceTop. Two tanks with two DOMs in each are placed at the top of each string forming an IceTop station.

An dense sub-array called Deep Core is planned in the center of the IceCube detector. Six strings will be deployed around the central IceCube string. Those strings will contain DOMs optimized for low energy neutrino detection (starting at

$\sim$ 20 GeV) spaced densely in the clear ice below the dust layer. The surrounding strings will be used as an active veto in order to gain 4π sensitivity to low energy neutrinos.

The in-ice DOMs are connected to the surface via a twisted-pair cable which simultaneously powers the DOM and carries digital communications to and from the DOM. These cables are gathered together with the IceTop DOMs at the surface and run to the counting house located in the center of the array. The counting house holds computers which communicate with the DOMs and run the Data Acquisition System (DAQ).

The DOMs are identified by a unique pair of numbers: the string number and the OM number. String numbers run from 1 to 86 and OM numbers run from 1 to 64. OM 1 is closest to the surface and OM 60 is at the bottom of the string. DOMs 61-64 are the four IceTop DOMs for a particular string.

Construction of the detector began in the austral summer 2004-2005 with the deployment of the first IceCube string and four IceTop stations [34]. Eight more strings were deployed in the 2005-2006 season and 13 more in the 2006-2007 season to bring the total to 22. Between each construction phase, data has been taken in an official physics run. For the 22-string detector, this physics run started in May 2007 and lasted until March 2008. All of the data used in this thesis is from this physics run. Since then, 18 strings were added in the 2007-2008 construction season, and 19 were added in the 2008-2009 season (including 1 Deep Core string) to bring the current total to 59 strings. Figure 3.8 shows which strings are deployed in each season.

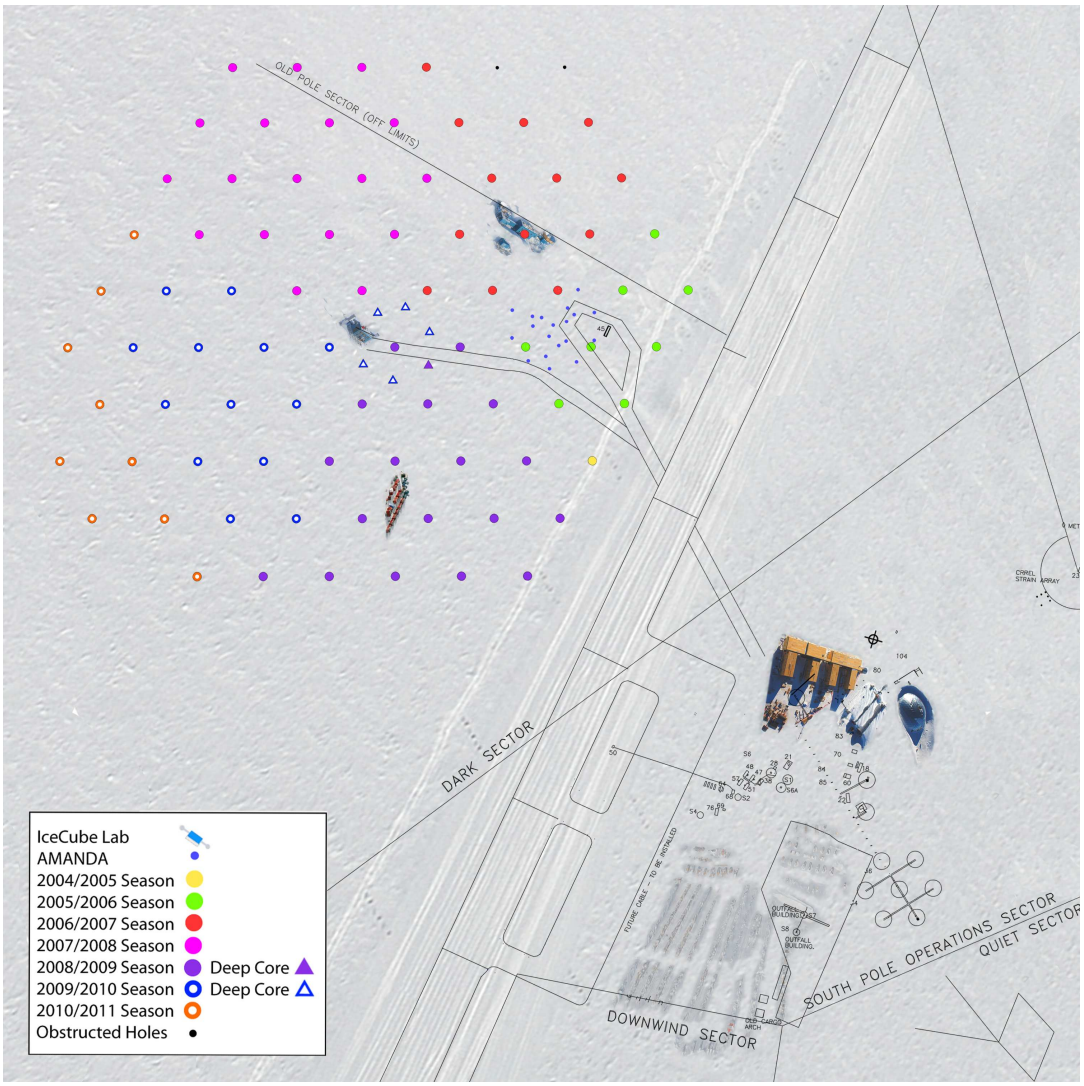

Figure 3.8: The location of IceCube's planned 86 strings at the South Pole.

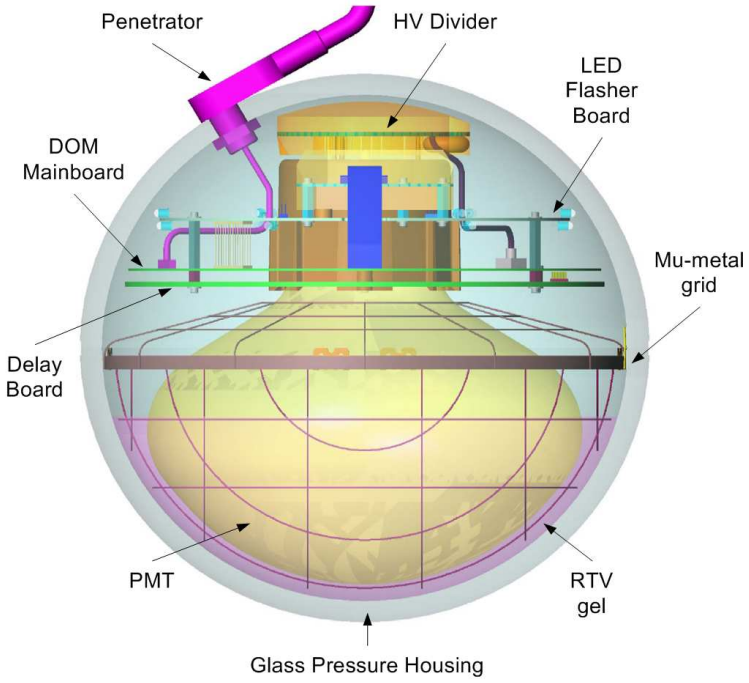

Figure 3.9: A schematic of an IceCube DOM.

3.3 The Digital Optical Module

The Digital Optical Module (DOM) (see figure 3.9) is the building block of the IceCube detector [34] [35]. The DOM is a stand-alone data acquisition computer. The photo-multiplier tube (PMT) collects incident light. The mainboard contains circuits to digitize the PMT signals and communicate them to the surface electronics. The LED flasher board contains light emitting diodes (LEDs) that are used to study the surrounding ice and calibrate the detector's geometry.

A PMT consists of a thin photo-cathode hemisphere and a dynode chain. The photo-cathode's low work function allows a certain percentage of incident photons to knock a single electron out of the photocathode. This percentage is called the

quantum efficiency of the PMT, and the first electron knocked out is called a photoelectron (PE). This PE is then accelerated towards the first in a chain of dynodes held at progressively more positive voltages. At each dynode, accelerated electrons knock progressively more low energy electrons out that then accelerate towards the next dynode. Finally, the electrons reach the anode, where the accumulation of charge results in a sharp current pulse indicating the arrival of a photon at the photocathode. The average number of electrons to come out of the final dynode per incident PE is the gain of the PMT.

The PMT for IceCube DOMs is a HAMAMATSU R7081-02 25 cm diameter PMT with 10 dynodes. This PMT was chosen for its for its low dark noise rate of 500 Hz and good time and charge resolution for single photons. It has a peak quantum efficiency of 25% at 390 nm and was operated at a nominal gain of 1×10^7 while taking all the data used in this thesis.

When the current on a PMT exceeds a certain discriminator threshold, capture of the waveform is triggered. The capture is initiated by the on-board Field-Programmable Gate Array (FPGA) which causes one of the two Analog Transient Waveform Digitizers (ATWDs) and the Fast Analog to Digital Converter (fADC) to capture the PMT waveform. All of these electronics are located on the mainboard of the DOM. The first three of the four ATWD channels capture the waveform at nominal gains of 16, 2, and 0.25. Usually, only the high gain ATWD channel is used in reconstruction unless it is saturated. In that case, the highest gain non-saturated channel is used. The fADC samples the waveform over a much longer period of time, but at a lower resolution. Its primary function is to capture late arriving light.

The DOM waveform is only digitized and sent to the surface if the readout event satisfies a Local Coincidence (LC) condition. This condition says that a DOM is read out only if either of the two closest DOMs above it or two closest DOMs below it on the string also had a trigger within ± 1000 ns. This LC condition suppresses almost all of the isolated noise hits in the detector, and allows the bandwidth to the surface to be suppressed to a manageable level.

3.4 Online Systems

Data Acquisition

The Data Acquisition system (DAQ) controls the collection of the DOM waveforms and assembly of those waveforms into events based on flexible trigger criteria. For each string, a dedicated computer, the DOMHub, houses several custom PCI cards (the DOM Readout or 'DOR' cards) which perform the communication with, and supply power to, the DOMs. Several other computers called the String Processors provide the rest of the DAQ with a well-ordered stream of data from the DOMs attached to it. The String Processor maintains the time calibration records for each DOM and performs the calibration for all readout and monitoring events.

Trigger

The trigger includes many possible conditions that identify events in the detector, but data used in this thesis is collected only through the simple majority trigger (SMT). This trigger condition is met when 8 DOMs satisfy the LC condition and have waveforms digitized in a window of 5 μs. The first 1 μs of this time is

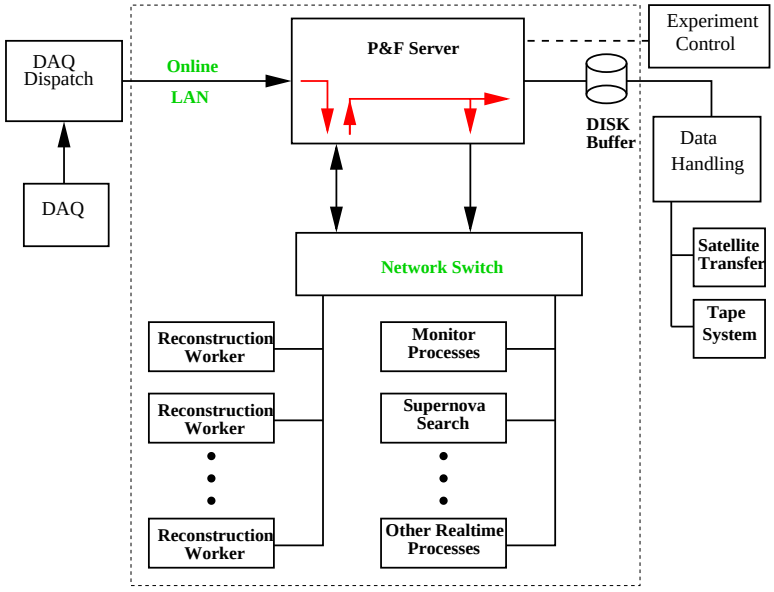

Figure 3.10: PnF System

called the trigger window. A readout window of 10 μs is then added before and after the trigger window. All DOM waveforms within the total window of length 21 μs are then recorded and assembled into an event. Any events with overlapping windows are then combined into one single event. Because of this, events can be built that last much longer than the standard 21 μs window.

Processing and Filtering

All the data collected by the DAQ totals approximately 1.2 MB/sec (∼100 GB/day). Communication satellites are only visible to the South Pole half the time and can only transfer approximately 25 GB/day of physics data. Consequently, a large fraction of the data must be rejected by systems at the Pole. Filters that are motivated by various physics analyses select a number of events that are deemed interesting. These are then sent to the north via the communication satellites.

The system that implements these filters is called the Processing and Filtering (PnF) system (figure 3.10). This system reads the data taken by the DAQ from a buffer known as DAQ-dispatch. This buffer allows the PnF and DAQ systems to run independently.

A cluster of machines, called pfclients, run reconstructions over the data and then execute the various filtering algorithms. The PnF server (pfserver) runs a daemon that keeps track of what files in the DAQ-dispatch need to be filtered, what pfclients are working on which files, and when pfclients finish and are ready for more data. The filtering is thus distributed on a per file basis. In the future, the reconstruction and filtering will be distributed to the pfclients on a per event basis. In this future setup, the pfserver will then take care of reordering the events post filtering.

Events that pass teh filter are written to a buffer that is made available to various other systems, including SPADE. The South Pole Archival and Data Exchange (SPADE) system manages the transfer of data over the communication satellites. All the events are written to a separate buffer that is again available to other interested systems, including the GRB filter (section 4.3). Another one of these systems records all the events on tapes. All the events are thus saved, but it is hoped that the tapes are not necessary.

The filters implemented in the pfclients are listed in table 3.1. The rate shows the number of events collected per second that satisfy that listed filter. The prescale shows the percentage of those events that satisfy the filter that are actually transferred via satellite. For example, a prescale of 5 implies that 1/5 of all events that

satisfy the filter are actually transferred. This is determined randomly in order to collect an unbiased sample.

Data selected by three of the implemented filters is used at various points in this thesis. Those three filters are the muon filter (IceCubeMuonFilter), the high energy filter (EHEFilter), and the GRB filter. The muon filter runs the linefit reconstruction (section 5.3.1), and chooses events which satisfy one of the following conditions:

- linefit zenith $\geq$ 70 degrees and number of hit DOMs $\geq$ 10
- linefit zenith $\geq$ 60 degrees and number of hit DOMs $\geq$ 40
- linefit zenith $\geq$ 50 degrees and number of hit DOMs $\geq$ 50

The high energy filter simply accepts all events with a number of hit DOMs $\geq$ 80. The GRB filter is discussed in detail in section 4.3.

Table 3.1: Physics Filter Rates During IceCube 22-string Physics Run

Filter	**Rate (Hz)**	**Prescale**	**Description**
CascadeFilter	17.92	1	Electromagnetic showers
ContainedFilter	4.03	1	AMANDA/IceCube combined events passing a veto
DowngoingContainedFilter	3.09	1	Downgoing track events passing a veto
EHEFilter	1.28	1	High energy events
FilterMinBias	531.80	200	All events
IceCubeMuonFilter	19.51	1	Upgoing track events
IceTopSMT	15.39	5	All IceTop triggered events
IceTopSMT_InIceCoincidence	2.63	1	Events with IceTop and InIce activity
IceTopSMT_Large	0.93	1	Large IceTop triggered events
InIceSMT_IceTopCoincidence	13.20	5	Events with IceTop and InIce activity
JAMSMuonFilter	0.0	1	Upgoing track events in AMANDA
LowEnergyContainedFilter	4.11	1	Single string events with other cuts
MoonFilter	0.0	1	Events from moon direction (when moon is above horizon)
MuonFilter	19.51	1	Combined upgoing track events
PhysicsMinBiasTrigger	91.25	40	Events that are randomly triggered

3.5 Calibration

3.5.1 Timing Calibration

The Reciprocal Active Pulsing (RAPCal) procedure periodically synchronizes the surface time (Universal Time) to the local DOM time. Since the DOM oscillator is stable, this procedure is done only once every two seconds. It starts when the DOR card sends out a short bipolar pulse to the DOM. The DOM uses the same hardware that is typically used for digital communication to digitize the pulse when it is received. By the time the waveform is received at the DOM, it has dispersed to microsecond length and the waveform can be sampled at the relatively slow 20 Mhz communications rate. The DOM then waits a known amount of time and transmits a pulse identical to the one it was sent by the DOR card. The DOM also transmits the time stamp and waveform that it recorded in the ice. The DOR card at the surface digitizes the DOM-sent waveform the same way the DOM did.

By comparing global and DOM-local timestamps for the transmission and reception events, a rough scale of the timing offset between the surface and DOM clocks can be obtained, but by isolating the final waveform features precision beyond the intrinsic 20 MHz timing can be attained. The precision arises from the reciprocity of the system. Since the pulse is sent down the same path both to and from the DOM, the final dispersed pulse should be identical in shape at the DOM and the DOR (figure 3.11). It does not matter what fiducial mark on the dispersed pulse is used to time the pulse as long as we choose the same mark on both the sending and receiving pulse.

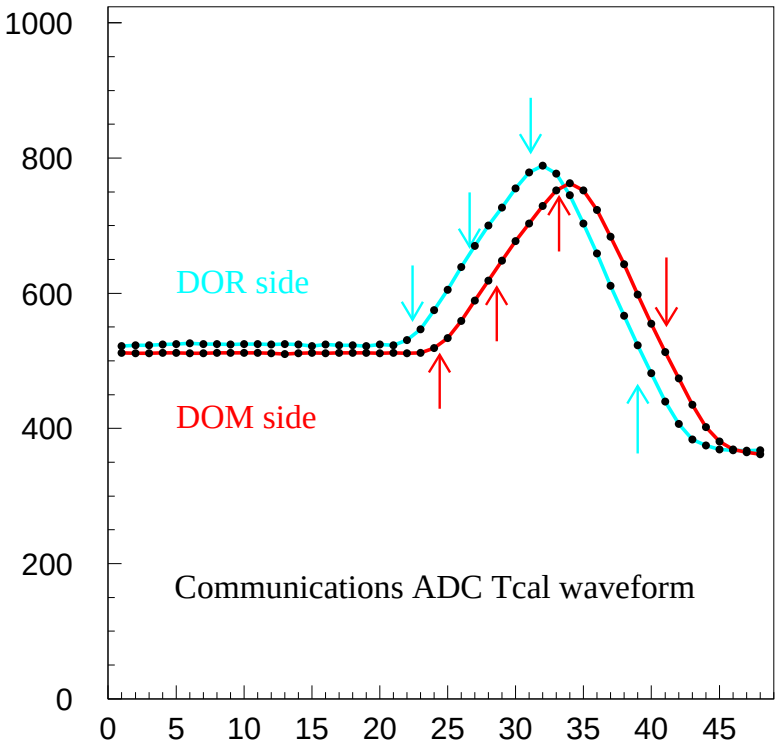

Figure 3.11: Example waveforms used in the timing calibration. Shown are the waveform recorded by the DOR and the waveform recorded by the DOM. The x-axis is units of the 20 MHz communications cycle. The arrows show waveform features as extracted by different algorithms.

3.5.2 DOM Calibration

DOMs are calibrated periodically with a program called *domcal*. This program executes a wide variety of different routines to calibrate different parts of the DOM. A pulser calibration simply uses the on-board discriminator to set a pulser to a known voltage. This pulser can then be used to drive the DOM readouts as opposed to the PMT. The response of each ATWD bin to a range of known voltages is measured in order to create a function that maps these responses to the real input voltages. An amplifier calibration uses the now calibrated pulser to measure the specific gains of each ATWD channel. The waveform from the DOM clock is fed to the ATWD in order to measure the ATWD sampling speed.

The PMT response to single photoelectrons must be measured. To do this, the PMT high-voltage is turned on, and the PMT is set up to collect individual photoelectron events. The integrated charge from each event is used to build a histogram like the one displayed in figure 3.12. Low-amplitude noise in the PMT generates the exponential tail, called the noise pedestal. Single photoelectrons (SPEs) generate the Gaussian peak. The peak-to-valley ratio and the position of the SPE peak can be measured and used to calculate the gain of the PMT. This is done at a variety of high-voltage settings, so that a relation between high-voltage and gain is generated. During IceCube's 22-string operations of interest to this thesis, the DOMs were set to the high-voltage corresponding to a gain of 10^7.

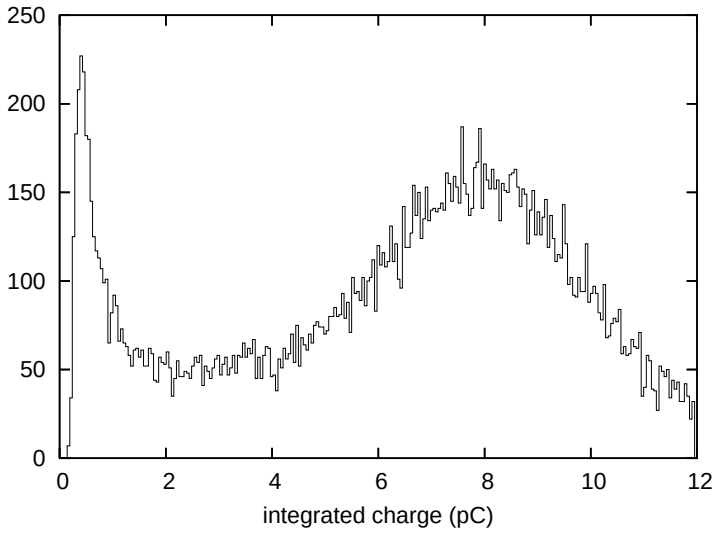

during

Figure 3.12: Typical charge histogram acquired during the calibration of an IceCube PMT with a voltage of 1340 V. Two features are prominent. First is the noise pedestal, the exponentially decaying low amplitude component. Also clear is the SPE peak which allows the conversion from integrated charge to PEs.

3.5.3 Geometry Calibration

The goal of the geometry calibration is to find the position of the DOMs to within one meter. This is accomplished in three stages. Stage one geometry uses deployment data and surveys for a preliminary geometry. The horizontal positions of the DOMs are measured by the combination of a survey of hole positions and data from the drill position acquired during drilling. The vertical positions are calculated by using pressure readings at the string's final location in combination with a measurement of the depth of the waterline. Stage two geometry seeks to correct the stage one values by flashing the LEDs on various DOMs and measuring the arrival times of the light in the nearby DOMs. Stage three geometry uses large amounts of downgoing muon data in order to track the movements of the array over time due to ice shear.

3.6 Backgrounds

Atmospheric muons are the dominant background to searches for cosmological neutrino events in IceCube. They are created by cosmic ray induced air showers in the atmosphere above the South Pole. The muons then rain down through the detector before ranging out. This background is partially eliminated by only looking at tracks that move up through the detector. In this way, IceCube is essentially using the Earth as a shield to cosmic rays. Even when considering upgoing tracks, misreconstructed atmospheric muons must be eliminated with track quality cuts (figure 3.13).

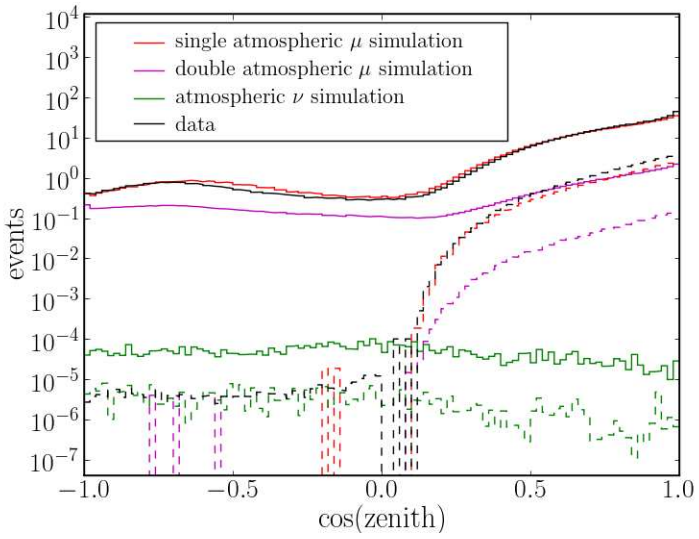

Figure 3.13: Zenith distributions of IceCube backgrounds. Solid lines are trigger level data, and dashed lines are data after various quality cuts. An event with a cos(zenith) of 1 is moving straight down through the detector. An event with a cos(zenith) of -1 is moving straight up through the detector.

The vast majority of the atmospheric muon background are single muon tracks moving down through the detector. Another important component of this background is two muon tracks triggering the detector at nearly the same time. These double muon events are especially good at mimicking an upgoing neutrino track when the first hits an area in the bottom of the detector and a second hits an area at the top of the detector soon after. These double muon events are much more persistant to quality cuts.

Atmospheric neutrinos are also created in the air showers caused by incident cosmic rays. They constitute an irreducible background in that they can pass through the Earth and create an upgoing muon track in the detector that is indis-

tinguishable from one created by a cosmological neutrino. Searches for cosmological neutrinos thus employ various strategies to account for this background. Searches for cosmological sources of neutrinos look for an excess over the isotropic background of atmospheric neutrinos. Searches for diffuse cosmological neutrinos attempt to find an excess above a known energy spectrum of atmospheric neutrinos.

The atmospheric neutrino spectrum has two parts. The first is the conventional flux from decaying $\pi^{\pm}$ and $K^{\pm}$ produced in cosmic ray induced air showers. The second is the 'prompt' flux from the decay of charmed hadrons. This flux does not turn on until higher energies because the charmed hadrons do not have time to interact before decaying until they reach extremely high energies. In this thesis, the *Bartol* [36] simulated model is used to estimate the flux of the conventional atmospheric neutrino spectrum and the *Naumov RQPM* [37] model is used for the prompt atmospheric neutrino flux. The sum of these fluxes is shown in figure 3.14.

There are two searches presented in this thesis: one in the northern hemisphere and one in the southern. Both searches are limited to the times and directions surrounding GRB observations. These temporal and spatial constraints reduce the background from atmospheric neutrinos to a miniscule rate. In the case of the northern hemisphere search, the analysis becomes almost background free. The Southern hemisphere search uses the spatial and temporal constraints to reduce the much greater rate of atmospheric muons.

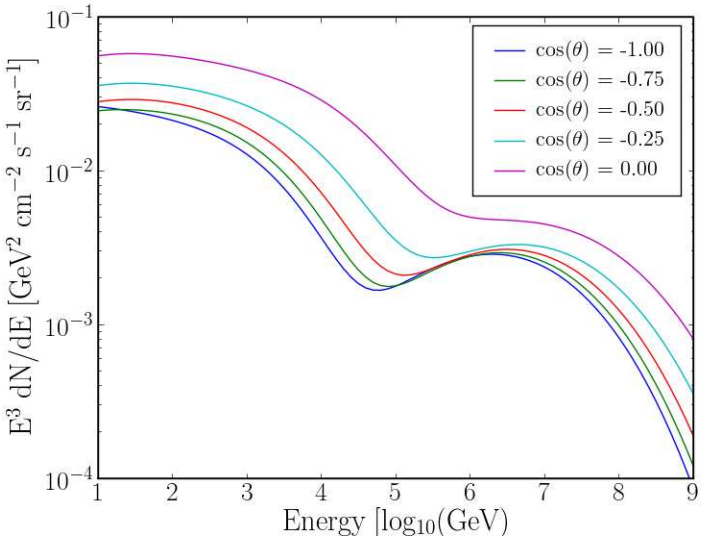

Figure 3.14: The atmospheric neutrino flux spectrum assumed in this thesis, sampled at various zenith angles. The *bartol* model dominates at lower energies, and the *Naumov RQPM* model takes over around 100 TeV.

3.7 Simulated Data

In addition to real data taking, it is necessary to simulate the response of the detector to signal and background events in order to better understand the real data and to accurately estimate the sensitivity to predicted signals. This is done using a full Monte Carlo chain. This chain begins with the simulation of the primary particles (either cosmic rays or neutrinos), continues with the propagation of resulting muons and photons through the detector, and finally ends with a reproduction of the IceCube hardware. After this Monte Carlo chain, the simulation data is processed in the same way as the real data.

The CORSIKA [38] program for simulating extensive air-showers in the atmosphere is used to model the down-going cosmic-ray muon flux in both single and

double muon events. Cosmological and atmospheric neutrinos are simulated with the NUGEN program. Because of the neutrino's very small interaction cross section, it's not practical to throw large numbers of neutrinos at the detector and to see which ones interact. Instead, the NUGEN program begins with the assumption that an interaction has occurred, and then assigns a weight to it that reflects that interaction's probability of occurring. Neutrinos are generated at an E^{-1} or E^{-2} spectrum, but are then re-weighted according to whatever spectrum is under investigation.

The Muon Monte-Carlo (MMC) [31] program tracks the continuous and stochastic energy losses of muons as they propagate through the Earth and ice. The photon propagation program, photonics [39], takes the timing and location of the muon energy losses and calculates how many resulting photo-electrons will be detected at each DOM. Since it is impractical to track every photon in the detector, the photon simulation is performed once and the resulting arrival time distributions are compiled into a table. The resulting photonics tables are parameterized by the direction of the muon, relative position of the muon and the DOM, the angle of detection on the DOM, and the absolute depth of the muon and DOM in the ice.

The IceCube hardware response is simulated by various software programs. The PMT-simulator takes photo-electron arrival times and constructs a waveform that shows the photo-multiplier tube response. The DOMsimulator takes those waveforms and simulates the DOM mainboard response. This involves simulation of the discriminator condition, filling of ATWD and fADC waveforms, and the application of the local coincidence logic. The trigger-sim program takes those

digital waveforms and decides if the conditions for detector triggering have been met.

3.8 Effective Area

It is useful to characterize the response of the detector in terms of an effective area A_{eff}. For a predicted number of neutrino events N_{events} associated with a diffuse neutrino flux (differential in area, time, energy and solid angle) $\Phi(E, \theta)$, the effective area A_{eff} is defined as the function that satisfies:

$$N_{events} = \int dt \int d\Omega \int dE \cdot \Phi(E, \theta) \cdot A_{eff}(E, \theta) \tag{3.3}$$

The effective area is defined so that it is flux-independent. With the effective area, one can calculate the expected number of events in the detector to any diffuse neutrino signal without re-running simulation. All of the effects in the simulation can be tied up in this one function. The effective area is different for different selection criteria since they result in different numbers of events recorded in the detector. The effective area of the 22-string IceCube to upgoing muon neutrinos is shown in figure 3.16. The event selection implied in this figure includes all the cuts in the northern hemisphere analysis excluding the angle cuts. They are all described in detail in chapter 7.

The effective area begins to drop at very high energies in high declination bands. These bands represent events that are moving up through the detector, and are thus associated with neutrinos that have propagated through the Earth. At these very high energies, the neutrinos have a shorter attenuation length when

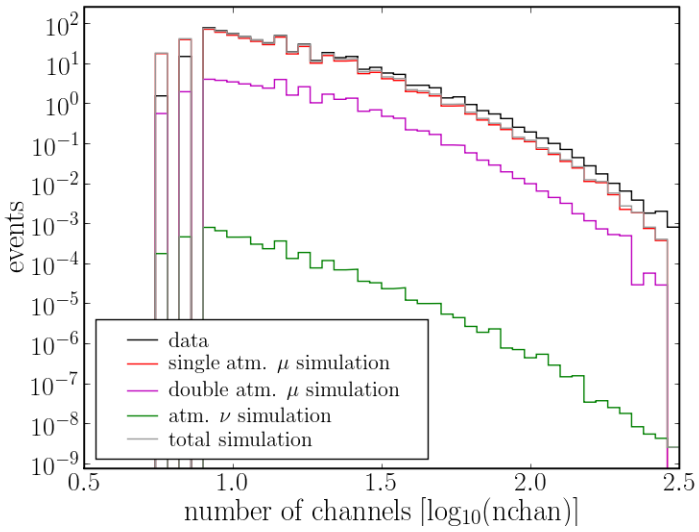

(a) Number of Hit DOMs

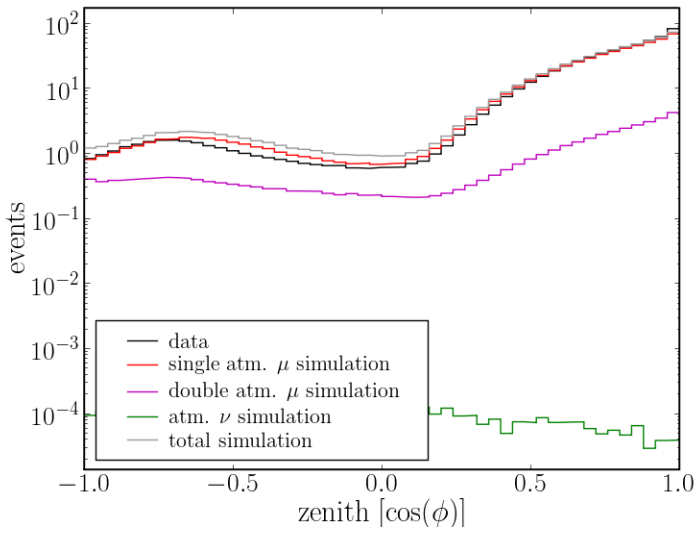

(b) Zenith Angle

Figure 3.15: Comparison of data and simulation at trigger level.

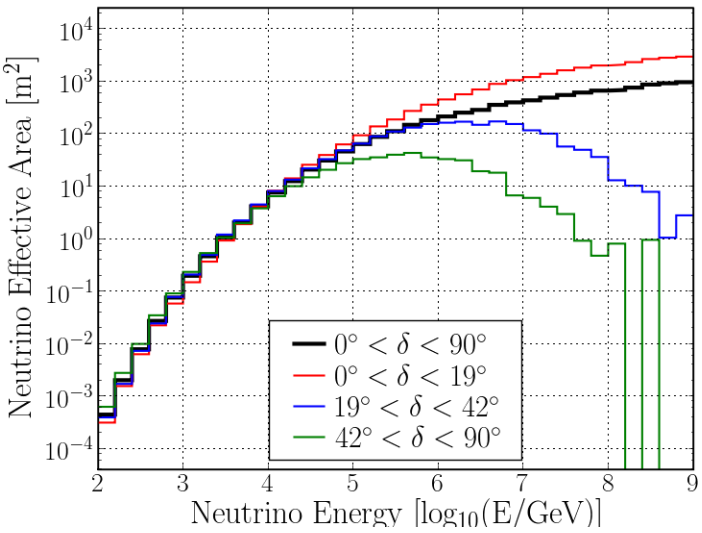

Figure 3.16: The effective area of IceCube to muon neutrinos after final cuts in the northern hemisphere analysis, plotted in different declination bands.

moving through the Earth, and thus IceCube has a lower chance of detecting them.

Chapter 4

GRB Selection

All GRB triggers taken by the Swift, Integral, and other Third Interplanetary Network (IPN3) satellites that occur during the IceCube 22-string physics run are considered for inclusion in this thesis. The majority of the bursts used were originally detected by Swift or use some Swift measured parameters. Bursts are usually identified in the form "GRBYYMMDD", where YY, MM, and DD refer to the last two digits of the year, month, and day the burst was detected respectively. If more than one burst is detected in a certain day, letter suffixes are added in the order they are detected. For example, GRB070721B refers to the second burst detected on July 21st, 2007.

4.1 Gamma-ray Burst Coordinate Network

The Gamma-ray Burst Coordinate Network (GCN) is a system for distributing GRB triggers measured by satellites to various ground based detectors, institutions, or individuals who are interested in receiving them [40]. The first distributed information about detected GRBs are *notices*. These are initiated by satellite triggers and are then sent out as quickly possible in order to allow ground based instruments to follow up with observations in optical, X-ray, or other wavelengths.

The GCN sends out a second set of messages called *circulars* which contain

more detailed reports of GRB observations. Circulars are initiated by e-mails from participating collaborations, and are then distributed to a list of interested parties that is separate from the list associated with notices.

4.2 Satellites

4.2.1 Swift

Launched in November of 2004, the Swift observatory is an orbiting robotic spacecraft whose primary scientific objective is to determine the origin of GRBs and to pioneer their use as probes of the distant, and thus young universe [41] [42]. Swift has the ability to scan the sky for gamma-ray bursts and to quickly slew to the position of a burst when one is detected. There are three instruments aboard the satellite: the Burst Alert Telescope (BAT), the X-Ray Telescope (XRT), and the Ultraviolet and Optical Telescope (UVOT). The BAT searches the sky for new GRBs and, upon discovery, triggers an autonomous spacecraft slew to bring the burst into the XRT and UVOT fields of view. Such autonomy allows Swift to perform X-ray and UV/optical observations of approximately 100 bursts per year within 20 - 70 seconds of a burst detection. A schematic of the satellite is shown in figure 4.1.

The Burst Alert Telescope (BAT) provides the initial detection of the gamma-ray emission from a burst [43]. It then calculates the position of the burst and sends it to the systems that control the pointing of the satellite. It is sensitive to gamma-rays in the 15-150 keV energy range, and its pointing resolution is 1-3 arcmin. Refined analysis of the BAT data usually provides information about the

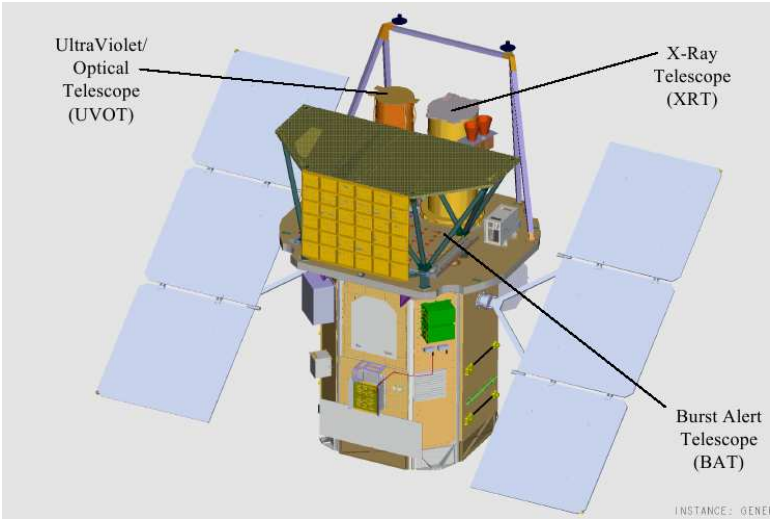

Figure 4.1: The Swift Observatory. The BAT, consisting of the coded aperture mask above and the detector array below, is shown in the foreground. A fringe shield that surrounds the BAT is not pictured. The XRT and UVOT are shown behind the BAT.

gamma-ray spectrum that is then used to calculate the predicted neutrino spectrum used in this thesis.

The BAT is able to monitor a large field of view, about 2 steradians, by using a coded aperture imaging algorithm. This algorithm serves as a replacement for focusing optics, which can be very difficult at energies above 10 keV and do not allow a wide field of view. The coded aperture mask is a D shaped panel made up of 54,000 lead tiles arranged in a random but known pattern. As photons coming from a particular direction pass through the mask, they cast a shadow across an array of detectors positioned below the mask. An automated Fourier transform algorithm compares the shadow with those expected from every point in the sky. The result is an image of the sky, with bright points where gamma-ray sources are present and dark background everywhere else.

The X-Ray Telescope (XRT) is designed to measure the 0.2 to 10 keV X-ray fluxes, spectra, and light curves of GRBs and afterglows over a wide dynamic range covering more than 7 orders of magnitude in flux [44]. The focusing XRT pinpoints GRBs to 5 arcsec accuracy within 10 seconds of target acquisition for a typical GRB and studies the X-ray counterparts of GRBs beginning at the time the XRT has stabilized on-target (20 - 70 seconds after burst discovery) and continuing for days to weeks. The XRT provides the vast majority of the final coordinates of the GRBs used in this thesis, including some that were originally detected by other satellites. The error on these coordinates is much less than the angular resolution that IceCube can achieve, and so this is not a significant source of error in this thesis.

4.2.2 Third Interplanetary Network

The Third Interplanetary network (IPN3) is a group of GRB detectors that precisely measure the arrival time of gamma-rays from GRBs [45]. By combining these measurements, the location of the burst can be found. The first interplanetary network was formed in 1978 with the various spacecraft in orbits around the Sun, Venus, and the Earth. The current version of the network began in 1992, and now consists Swift, Suzaku, AGILE, Konus-Wind, Integral, 2001 Mars Odyssey, Messenger, Rhessi, and NASA/ESA Ulysses.

Swift's XRT can locate GRBs with a much higher accuracy than combining the measurements of the IPN3 spacecraft. Many of them were obtained when the

Swift XRT followed up on a burst detection by one of the other IPN3 satellites. In the case of three bursts used in this thesis, the XRT data is not available and the IPN3 measurements must be used. Some basic information on the satellites that provided data for these localizations, or just triggers for the Swift XRT to follow up on, are described below.

Konus/Wind

The Wind satellite was launched in 1994 by NASA [46]. It's primary purpose is the study of solar wind, and for this reason has been inserted into a halo orbit in the solar wind upstream from the Earth. The Konus instrument on board the satellite is the first Russian scientific instrument aboard an American satellite since space cooperation between the U.S. and Russia was resumed in 1987. Konus consists of two detectors mounted on the top and bottom of the satellite. They provide isotropic sensitivity to gamma-ray bursts and spectrum measurements in the 10 keV to 10 MeV range.

Integral

The European Space Agency's International Gamma-Ray Astrophysics Laboratory (INTEGRAL) was launched in 2002 into an Earth orbit with a 72 hour period [47] [48]. Integral carries two main instruments, a spectrometer and an on-board imager (IBIS). Both instruments provide images of the γ-ray sky in the 15 keV - 10 MeV energy range using the coded aperture technique. GRBs detected by IBIS can be quickly localized to within a few arcminutes by the on-board burst alert system.

Agile

The Italian Space Agency's Agile was launched into an equatorial orbit in

2007 [49] [50]. The *Super*AGILE instrument on-board is a hard X-ray imager using a coded mask that is sensitive to X-rays in the energy range 15 45 keV. *Super*AGILE is able to localize bursts with an optimum angular resolution of 6 arcminutes. It is placed on top of a a complementary gamma-ray imaging detector (GRID) using a silicon tracker that is sensitive to gamma-rays in the 50 MeV 30 GeV energy range.

Suzaku

Suzaku was launched in 2005 by the Japan Aerospace Exploration Agency into a circular Earth orbit. The on-board Wide-band All-sky Monitor [51] [52] submits burst alerts to the GCN. Its four subdetectors are designed to monitor the sky from 50 keV to 5 MeV with a large effective area and good spectral capabilities.

Table 4.1: Table of Satellite Parameters

Satellite	Energy Range (keV)	Field of View (sr)	Localizations (arcmin)
Swift (BAT)	15 - 150	2	1-3
Swift (XRT)	0.2 - 10	4.7×10^{-5}	8.3×10^{-2}
Integral	15 - 1×10^5	0.256	2-3
Konus/Wind	10 - 1×10^5	4π	(IPN based)
Suzaku	50 - 5×10^4	4π	(IPN based)
Agile	15 - 45	$4\pi/3$	(IPN based)

4.3 IceCube GRB Filter

During the IceCube 22-string detector physics run, a GRB filter was installed and running at the South Pole. The purpose of this filter was to capture raw IceCube data surrounding GCN notices, and to transfer this data via satellite to the north. Because of the need to very accurately determine the expected background level at

hard cut levels, this dataset was not used to optimize most of the analyses contained in this thesis, but it was used to validate the stability of the IceCube detector during the bursts. For each GRB, the trigger level rate and time difference between events were plotted and fit. Examples of those plots are shown for GRB070616 in figure 4.2. The IceCube detector was stable during all the bursts used in this thesis. The timing and directions of all the bursts are listed in table 4.2 at the end of this chapter.

4.4 GRB Neutrino Spectra Calculation

The neutrino spectrum for each GRB included in this thesis was calculated according to the formulas in section 2.4. The parameters that were used in this calculation are listed in table 4.3. When a certain burst parameter was not measured, average values were used [22]. Those average values are $E_{iso} = 10^{51}$ erg, $z = 2.15$, $f_\gamma = 7.41$ MeV^{-1} cm^{-1}, $\epsilon_\gamma^b = 0.2$ MeV, $\alpha_\gamma = 1$, and $\beta_\gamma = 2$. For the variability t_{var} and the jet Lorentz boost factor Γ_{jet} which have not been measured for any of the GRBs, average values of 0.01 s and 315 are assumed. The resulting neutrino spectra are shown in figure 4.3.

Clear differences between the average Waxman-Bahcall spectrum and the calculated spectra are observed which stresses the importance of using individual fluxes. For example, Waxman and Bahcall based their calculations on the bursts in the BATSE population. Swift is a more sensitive satellite, and thus its population of bursts is dimmer on average than the BATSE population. That is why the calculated

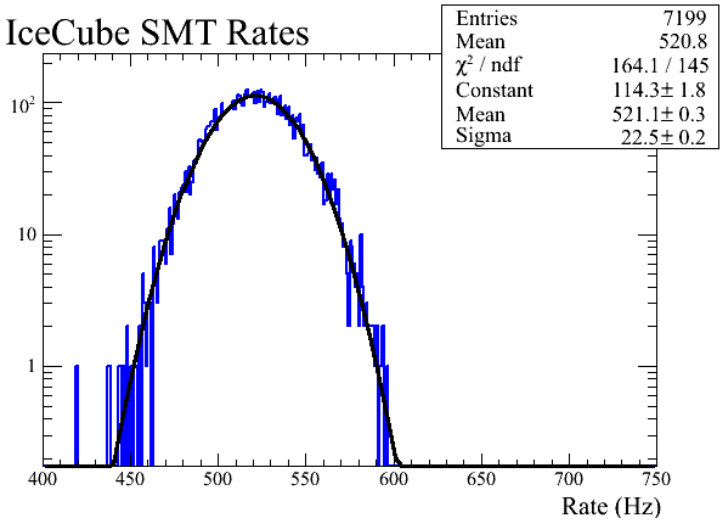

(a) Rate Histogram

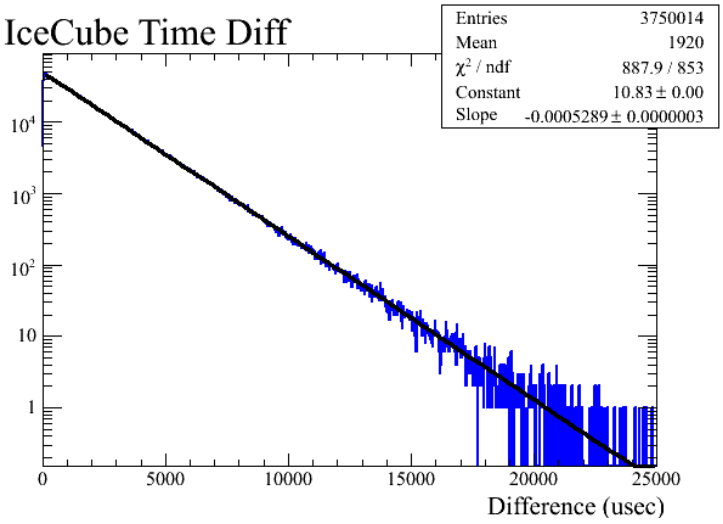

(b) Time Difference

Figure 4.2: Examples of the quality plots generated for each GRB. Panel (a) shows a histogram of the number of events that trigger the detector in 7200 one second bins surrounding the burst trigger. Panel (b) shows the time difference between subsequent events in microseconds.

individual neutrino spectra are consistently lower than the average Waxman-Bahcall spectrum.

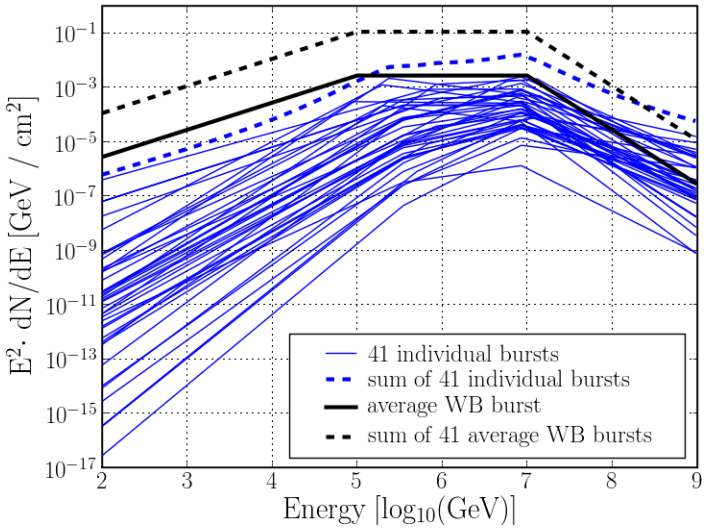

(a) Northern Hemisphere Spectra

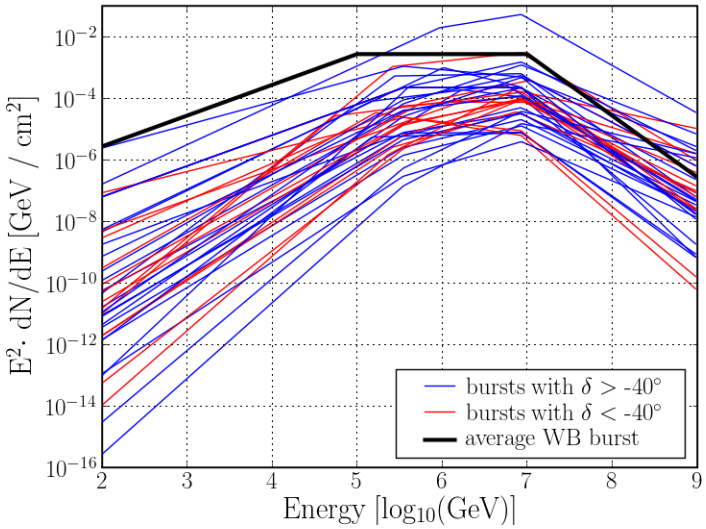

(b) Southern Hemisphere Spectra

Figure 4.3: Calculated neutrino spectra for all the bursts included in this thesis. Panel (a) shows those bursts in the northern hemisphere analysis along with the average Waxman-Bahcall spectra. Panel (b) shows those bursts included in the southern hemisphere analysis separated into two declination bands, again, with the average Waxman-Bahcall spectra shown.

Table 4.2: General Burst Parameters

GRB	T_0	T_1	T_2	RA	Dec	GRB	T_0	T_1	T_2	RA	Dec
Northern Hemisphere Bursts						Southern Hemisphere Bursts					
GRB070610	20:52:26	-0.8	4.4	298.8	26.2	GRB070611	01:57:13	-6.3	7.3	2.0	-29.8
GRB070612A	02:38:45	-4.7	418.0	121.4	37.3	GRB070612B	06:21:17	-6.4	10.3	261.6	-8.8
GRB070616	16:29:33	-2.6	602.2	32.2	56.9	GRB070615	02:20:45	-5.0	35.0	44.3	-4.4
GRB070704	20:05:57	-57.3	400.8	354.7	66.3	GRB070621	23:17:39	-5.2	36.4	323.8	-24.8
GRB070714B	04:59:29	-0.8	65.6	57.8	28.3	GRB070626	04:05:33	0.0	188.0	141.4	-39.9
GRB070724B	23:25:09	-2.0	120.0	17.6	57.7	GRB070628	14:41:02	-31.7	16.2	115.3	-20.3
GRB070808	18:28:00	-0.7	41.4	6.8	1.2	GRB070707	16:08:21	-0.5	1.5	267.7	-69.0
GRB070810B	15:19:17	0.0	0.1	9.0	8.8	GRB070721A	10:01:08	-0.1	3.7	3.1	-28.6
GRB070917	07:33:57	-0.1	11.4	293.9	2.4	GRB070721B	10:33:48	-6.7	359.9	33.1	-2.2
GRB070920A	04:00:13	15.1	75.0	101.0	72.3	GRB070724A	10:53:50	0.0	0.4	27.8	-18.6
GRB071003	07:40:55	-7.6	167.4	301.9	10.9	GRB070729	00:25:53	-0.1	1.1	56.3	-39.3
GRB071008	21:55:56	-11.0	14.0	151.6	44.3	GRB070731	09:33:22	-0.1	3.0	328.6	-15.7
GRB071010B	20:45:47	-35.7	24.1	150.5	45.7	GRB070802	07:07:25	4.9	23.2	36.9	-55.5
GRB071010C	22:20:22	-2.0	20.0	338.1	66.2	GRB070805	19:55:45	-0.6	35.7	245.1	-60.0
GRB071011	12:40:13	-9.5	63.8	8.4	61.1	GRB070809	19:22:17	-0.4	1.1	203.8	-22.1
GRB071013	12:09:19	-5.9	23.4	279.5	33.9	GRB070821	12:29:24	-10.0	210.0	95.5	-63.9
GRB071018	08:37:41	-50.0	417.7	164.7	53.8	GRB070824	20:50:00	0.0	17.0	171.9	-27.3
GRB071020	07:02:27	-3.0	7.4	119.7	32.9	GRB070911	05:57:44	-73.0	158.8	25.8	-33.5
GRB071021	09:41:33	-31.4	252.2	340.6	23.7	GRB070913	00:36:43	-2.4	1.2	228.7	-24.3
GRB071025	04:08:54	38.5	193.8	355.1	31.8	GRB070920B	21:04:32	-11.2	13.4	0.1	-34.8
GRB071028A	17:41:01	0.0	48.9	119.8	21.5	GRB070923	19:15:23	0.16	0.37	184.6	-38.3
GRB071101	17:53:46	-1.9	10.0	48.2	62.5	GRB070925	15:52:32	-3.0	32.0	253.2	-22.0
GRB071104	11:41:23	-5.0	17.0	295.6	14.6	GRB071001	16:31:48	-1.6	64.7	149.7	-59.8
GRB071109	20:36:05	-5.0	35.0	289.9	2.0	GRB071006	06:41:40	0.0	13.0	335.3	-23.1

Table 4.2: T_0 – time of satellite trigger, T_1 – time from trigger to beginning of window [s], T_2 – time from trigger to end of window [s], RA – right ascention of burst [°], Dec – declination of burst [°]

Table 4.2: (continued)

GRB	T_0	T_1	T_2	RA	Dec	GRB	T_0	T_1	T_2	RA	Dec
GRB071112C	18:32:57	-5.0	30.0	39.2	28.4	GRB071010A	03:41:12	-1.1	5.9	288.1	-32.4
GRB071118	08:57:17	-25.0	110.0	299.7	70.1	GRB071017	00:58:00	-0.25	0.75	274.7	-16.0
GRB071122	01:23:25	-29.4	47.3	276.6	47.1	GRB071028B	02:43:46	-3.5	54.5	354.2	-31.6
GRB071125	13:56:42	-0.5	8.5	251.2	4.5	GRB071031	01:06:36	-4.5	192.5	6.4	-58.1
GRB080121	21:29:55	-0.4	0.4	137.2	41.8	GRB071112B	18:23:31	0.0	0.3	260.2	-80.9
GRB080205	07:55:51	-10.1	105.3	98.3	62.8	GRB071117	14:50:06	-0.4	13.9	335.0	-63.4
GRB080211	07:23:39	-10.0	50.0	44.0	60.0	GRB071227	20:13:47	-0.1	1.9	58.1	-56.0
GRB080218A	20:08:43	-12.8	18.6	355.9	12.2	GRB080120	17:28:30	-2.0	22.0	225.3	-10.9
GRB080307	11:23:30	1.7	146.1	136.6	35.1	GRB080123	04:21:57	0.3	122.2	339.0	-64.9
GRB080310	08:37:58	-71.8	318.7	220.1	-0.2	GRB080129	06:06:45	-15.0	49.0	105.3	-7.8
GRB080315	02:25:01	-5.0	65.0	155.1	41.7	GRB080130	11:13:02	-1.0	68.0	261.6	-53.2
GRB080319C	12:25:56	-0.3	51.2	259.0	55.4	GRB080204	13:56:32	-1.0	10.0	285.6	-63.0
GRB080319D	17:05:09	0.0	50.0	99.5	23.9	GRB080212	17:34:33	-60.5	75.7	231.1	-22.7
GRB080320	04:37:38	-60.0	40.0	177.7	57.2	GRB080229A	17:04:59	-15.1	64.9	228.2	-14.7
GRB080325	04:09:17	-29.3	170.5	277.9	36.5	GRB080229B	23:33:01	-10.0	110.0	199.3	-64.9
GRB080328	08:03:04	-2.2	117.5	80.5	47.5	GRB080303	09:10:35	-0.2	73.2	112.1	-70.2
GRB080330	03:41:16	-0.5	71.9	169.3	30.6						

Table 4.2: T_0 – time of satellite trigger, T_1 – time from trigger to beginning of window [s], T_2 – time from trigger to end of window [s], RA – right ascention of burst [°], Dec – declination of burst [°]

Table 4.3: Burst Spectrum Parameters

	γ-ray spectrum						ν spectrum					
GRB	$E_\gamma^{\rm iso}$	z	f_γ	ϵ_γ^b	α_γ	β_γ	f_ν	ϵ_ν^b	ϵ_ν^s	α_ν	β_ν	$\beta_\nu+2$
Northern Hemisphere Bursts												
GRB070610	1.00	2.15	0.24	0.2	1.76	2	0.25	0.35	3.17	0.24	1.24	3.24
GRB070612A	1.00	2.15	11.0	0.2	1.69	2	13.30	0.35	3.17	0.31	1.31	3.31
GRB070616	1.00	2.15	19.2	0.2	1.61	2	27.99	0.35	3.17	0.39	1.39	3.39
GRB070704	1.00	2.15	5.9	0.2	1.79	2	5.75	0.35	3.17	0.21	1.21	3.21
GRB070714B	0.16	0.92	0.72	0.2	1.36	2	0.06	0.95	12.98	0.64	1.64	3.64
GRB070724B	1.00	2.15	18.0	0.08	1.15	2	8.85	0.86	3.17	-0.15	1.85	3.85
GRB070808	1.00	2.15	1.2	0.2	1.47	2	2.50	0.35	3.17	0.53	1.53	3.53
GRB070810B	1.00	2.15	0.01	0.2	1.44	2	0.02	0.35	3.17	0.56	1.56	3.56
GRB070917	1.00	2.15	4.9	0.21	1.36	2	5.14	0.33	3.17	-0.36	1.64	3.64
GRB070920A	1.00	2.15	0.51	0.2	1.69	2	0.62	0.35	3.17	0.31	1.31	3.31
GRB071003	1.00	2.15	53.2	0.8	0.97	2	325.81	0.09	3.17	0.03	2.03	4.03
GRB071008	1.00	2.15	0.24	0.2	2.23	2	0.11	0.35	3.17	-0.23	0.77	2.77
GRB071010B	1.1	0.95	4.78	0.05	1.25	2.65	0.21	4.88	4.88	0.35	1.75	3.75
GRB071010C	1.00	2.15	7.14	0.2	1	2	2.67	0.35	3.17	1.00	2.00	4.00
GRB071011	1.00	2.15	2.2	0.2	1.41	2	5.39	0.35	3.17	0.59	1.59	3.59
GRB071013	1.00	2.15	0.32	0.2	1.6	2	0.48	0.35	3.17	0.40	1.40	3.40
GRB071018	1.00	2.15	1.0	0.2	1.63	2	1.39	0.35	3.17	0.37	1.37	3.37
GRB071020	8.0	2.15	7.71	0.32	0.65	2	70.75	0.22	1.12	0.35	2.35	4.35
GRB071021	1.00	2.15	1.3	0.2	1.7	2	1.54	0.35	3.17	0.30	1.30	3.30
GRB071025	1.00	2.15	6.5	0.2	1.79	2	6.34	0.35	3.17	0.21	1.21	3.21
GRB071028A	1.00	2.15	0.3	0.2	1.87	2	0.25	0.35	3.17	0.13	1.13	3.13
GRB071101	1.00	2.15	0.08	0.2	2.25	2	0.04	0.35	3.17	-0.25	0.75	2.75
GRB071104	1.00	2.15	7.14	0.2	1	2	2.67	0.35	3.17	1.00	2.00	4.00

Table 4.3: $E_\gamma^{\rm iso}$ [10^{51} erg], f_γ [MeV^{-1} cm^{-2}], ϵ_γ^b [MeV], $f_\nu \times 10^{-15}$ [GeV^{-1} cm^{-2}], ϵ_ν^b [TeV], ϵ_ν^s [TeV]. The parameters f_γ and f_ν are the fluxes at ϵ_γ and ϵ_ν of the gamma-ray and neutrino spectrum, respectively.

Table 4.3: (continued)

	γ-ray spectrum						ν spectrum					
GRB	$E_\gamma^{\rm iso}$	z	f_γ	ϵ_γ^b	α_γ	β_γ	f_ν	$\epsilon_{\nu,1}$	$\epsilon_{\nu,2}$	α_ν	β_ν	$\beta_\nu+2$
GRB071109	1.00	2.15	0.66	0.2	1	2	2.67	0.35	3.17	1.00	2.00	4.00
GRB071112C	1.00	0.82	3.0	0.2	1.09	2	18.89	0.35	3.17	0.91	1.91	3.91
GRB071118	1.00	2.15	0.5	0.2	1.63	2	0.69	0.35	3.17	0.37	1.37	3.37
GRB071122	1.00	1.14	0.58	0.2	1.77	2	0.59	0.35	3.17	0.23	1.23	3.23
GRB071125	1.00	2.15	74.2	0.3	0.62	3.1	249.40	0.24	3.17	-0.10	2.38	4.38
GRB080121	1.00	2.15	0.03	0.2	2.6	2	0.01	0.35	3.17	-0.60	0.40	2.40
GRB080205	1.00	2.15	2.1	0.2	2.08	2	1.23	0.35	3.17	-0.08	0.92	2.92
GRB080211	1.00	2.15	46.6	0.44	0.61	2.62	212.00	0.20	3.17	0.38	2.39	4.39
GRB080218A	1.00	2.15	0.63	0.2	2.34	2	0.26	0.35	3.17	-0.34	0.66	2.66
GRB080307	1.00	2.15	0.87	0.2	1.78	2	0.87	0.35	3.17	0.22	1.22	3.22
GRB080310	1.00	2.43	2.3	0.2	2.32	2	0.97	0.35	3.17	-0.32	0.68	2.68
GRB080315	1.00	2.15	0.14	0.2	2.51	2	0.05	0.35	3.17	-0.51	0.49	2.49
GRB080319C	1.00	1.95	15.0	0.31	1.01	1.87	9.60	0.66	3.17	1.13	1.99	3.99
GRB080319D	1.00	2.15	0.32	0.2	1.92	2	0.24	0.35	3.17	0.08	1.08	3.08
GRB080320	1.00	2.15	0.27	0.2	1.7	2	0.32	0.35	3.17	0.30	1.30	3.30
GRB080325	1.00	2.15	4.9	0.2	1.68	2	6.06	0.35	3.17	0.32	1.32	3.32
GRB080328	1.00	2.15	22.3	0.2	1.13	0.28	42.96	0.25	3.17	-0.13	1.87	3.87
GRB080330	1.00	1.51	0.34	0.2	2.53	2	0.11	0.35	3.17	-0.53	0.47	2.47
Southern Hemisphere Bursts												
GRB070611	1.00	2.04	0.39	0.2	1.66	2	0.51	0.35	3.17	0.34	1.34	3.34
GRB070612B	1.00	2.15	1.7	0.2	1.55	2	2.87	0.35	3.17	0.45	1.45	3.45
GRB070615	1.00	2.15	7.14	0.2	1	2	2.67	0.35	3.17	1.00	2.00	4.00
GRB070621	1.00	2.15	4.3	0.2	1.57	2	6.91	0.35	3.17	0.43	1.43	3.43
GRB070626	1.00	2.15	391.0	0.23	1.45	2.28	120.98	0.94	3.17	0.72	1.55	3.55
GRB070628	1.00	2.15	3.5	0.2	1.91	2	2.71	0.35	3.17	0.09	1.09	3.09

Table 4.3: $E_\gamma^{\rm iso}$ [10^{51} erg], f_γ [MeV^{-1} cm^{-2}], ϵ_γ^b [MeV], $f_\nu \times 10^{-15}$ [GeV^{-1} cm^{-2}], ϵ_ν^b [TeV], ϵ_ν^s [TeV]. The parameters f_γ and f_ν are the fluxes at ϵ_γ and ϵ_ν of the gamma-ray and neutrino spectrum, respectively.

Table 4.3: (continued)

	γ-ray spectrum						ν spectrum					
GRB	$E_\gamma^{\rm iso}$	z	f_γ	ϵ_γ^b	α_γ	β_γ	f_ν	$\epsilon_{\nu,1}$	$\epsilon_{\nu,2}$	α_ν	β_ν	$\beta_\nu+2$
GRB070707	1.00	2.15	1.41	0.43	0.57	2	8.57	0.16	3.17	0.43	2.43	4.43
GRB070721A	1.00	2.15	0.07	0.2	2.46	2	0.02	0.35	3.17	-0.46	0.54	2.54
GRB070721B	1.00	3.63	2.1	0.2	1.34	2	6.26	0.35	3.17	0.66	1.66	3.66
GRB070724A	1.00	2.15	0.03	0.2	1.81	2	0.03	0.35	3.17	0.19	1.19	3.19
GRB070729	1.00	2.15	0.56	0.47	1.08	2	2.04	0.15	3.17	-0.08	1.92	3.92
GRB070731	1.00	2.15	0.16	0.2	1.65	2	0.21	0.35	3.17	0.35	1.35	3.35
GRB070802	1.00	2.45	0.28	0.2	1.79	2	0.27	0.35	3.17	0.21	1.21	3.21
GRB070805	1.00	2.15	0.72	0.2	1.84	2	0.64	0.35	3.17	0.16	1.16	3.16
GRB070809	1.00	2.15	0.1	0.2	1.69	2	0.12	0.35	3.17	0.31	1.31	3.31
GRB070821	1.00	2.15	100.0	0.27	1.3	2	135.09	0.26	3.17	-0.30	1.70	3.70
GRB070824	1.00	2.15	28.4	0.25	1.05	2	50.48	0.28	3.17	-0.05	1.95	3.95
GRB070911	1.00	2.15	21.0	0.17	1.6	2	13.50	0.41	3.17	-0.60	1.40	3.40
GRB070913	1.00	2.15	0.25	0.2	1.61	2	0.36	0.35	3.17	0.39	1.39	3.39
GRB070920B	1.00	2.15	0.66	0.04	0.67	2	0.18	1.71	3.17	0.33	2.33	4.33
GRB070923	1.00	2.15	0.05	0.2	1.02	2	0.39	0.35	3.17	0.98	1.98	3.98
GRB070925	1.00	2.15	2.0	0.2	1	2	2.67	0.35	3.17	1.00	2.00	4.00
GRB071001	1.00	2.15	0.77	0.2	1.62	2	1.10	0.35	3.17	0.38	1.38	3.38
GRB071006	1.00	2.15	20.8	0.2	0.75	2	51.69	0.35	3.17	1.25	2.25	4.25
GRB071010A	1.00	2.15	0.2	0.2	2.33	2	0.08	0.35	3.17	-0.33	0.67	2.67
GRB071017	1.00	2.15	7.14	0.2	1	2	2.67	0.35	3.17	1.00	2.00	4.00
GRB071028B	1.00	2.15	0.25	0.2	1.45	2	0.55	0.35	3.17	0.55	1.55	3.55
GRB071031	1.00	2.69	0.9	0.2	2.42	2	0.33	0.35	3.17	-0.42	0.58	2.58
GRB071112B	1.00	2.15	0.05	0.2	0.69	2	1.09	0.35	3.17	1.31	2.31	4.31
GRB071117	1.00	1.33	5.84	0.2	1.57	2	4.82	0.35	3.17	0.43	1.43	3.43
GRB071227	0.01	0.38	1.6	0.2	0.99	2	0.00	1.82	80.55	1.01	2.01	4.01

Table 4.3: $E_\gamma^{\rm iso}$ [10^{51} erg], f_γ [MeV^{-1} cm^{-2}], ϵ_γ^b [MeV], $f_\nu \times 10^{-15}$ [GeV^{-1} cm^{-2}], ϵ_ν^b [TeV], ϵ_ν^s [TeV]. The parameters f_γ and f_ν are the fluxes at ϵ_γ and ϵ_ν of the gamma-ray and neutrino spectrum, respectively.

Table 4.3: (continued)

	γ-ray spectrum						ν spectrum					
GRB	$E_\gamma^{\rm iso}$	z	f_γ	ϵ_γ^b	α_γ	β_γ	f_ν	$\epsilon_{\nu,1}$	$\epsilon_{\nu,2}$	α_ν	β_ν	$\beta_\nu+2$
GRB080120	1.00	2.15	1.5	0.2	1	2	2.67	0.35	3.17	1.00	2.00	4.00
GRB080123	1.00	2.15	0.57	0.2	2.15	2	0.30	0.35	3.17	-0.15	0.85	2.85
GRB080129	1.00	2.15	0.89	0.2	1.34	2	2.65	0.35	3.17	0.66	1.66	3.66
GRB080130	1.00	2.15	0.77	0.2	1.21	2	3.36	0.35	3.17	0.79	1.79	3.79
GRB080204	1.00	2.15	26.5	1.28	1.35	2	98.31	0.06	3.17	-0.35	1.65	3.65
GRB080212	1.00	2.15	2.9	0.07	0.31	2	2.94	1.04	3.17	0.69	2.69	4.69
GRB080229A	1.00	2.15	9.0	0.2	1.91	2	6.96	0.35	3.17	0.09	1.09	3.09
GRB080229B	1.00	2.15	7.14	0.2	1	2	2.67	0.35	3.17	1.00	2.00	4.00
GRB080303	1.00	2.15	0.66	0.2	1.54	2	1.14	0.35	3.17	0.46	1.46	3.46

Table 4.3: $E_\gamma^{\rm iso}$ [10^{51} erg], f_γ [MeV^{-1} cm^{-2}], ϵ_γ^b [MeV], $f_\nu \times 10^{-15}$ [GeV^{-1} cm^{-2}], ϵ_ν^b [TeV], ϵ_ν^s [TeV]. The parameters f_γ and f_ν are the fluxes at ϵ_γ and ϵ_ν of the gamma-ray and neutrino spectrum, respectively.

Chapter 5

Reconstruction Techniques

Reconstruction of IceCube muons takes place in many steps. Each successive reconstruction uses more computing resources and returns a better angular resolution. In order to keep the computing time needed to run the best reconstructions at a reasonable level, cuts are made along the way to limit the substantial background from atmospheric muons. The final reconstructions can achieve about 1 degree resolution, which is on the order of the difference between the neutrino and muon's directions.

5.1 Hit Preparation

Hit preparation is the first step in reconstructing an event. This involves taking the readouts from the DOMs and extracting a pattern of PE arrival times and positions that will be given to the reconstruction algorithms.

5.1.1 DOM Readout Cleaning

DOM readout cleaning is the first step in preparing hits. In this step, all readouts that occur on a predefined list of 29 bad DOMs are removed. DOMs are excluded for a variety of reasons. Some are known to be dead because they never powered up, spontaneously stopped powering up, or had a short in an in-ice

cable. Others have high currents and thus could not be operated. Two have bad communications with the surface. Two froze in too late to be included in the IC-22 data taking season. Finally, 7 have broken LC connections and were thus being operated in Dark Noise mode.

5.1.2 DOM Calibration

The raw ATWD and fADC waveforms are then calibrated with the DOMcalibrator module [53]. At this point, the waveforms from the three ATWD channels are combined to create one calibrated waveform. This is done on a bin by bin basis, in that if a high gain channel bin is saturated, the next highest gain channel is used to treat this bin. The length of the three ATWD channels is also treated such that the length of the calibrated waveform is equal to the longest of the three ATWD channels.

The presence of a toroid on the PMT base transformer gives a time constant to the electronics of the DOM that leads to an effect of "droop" clearly observable for high amplitude signal. The DOMcalibrator corrects this droop with a double time constant model. The response to an impulse signal $\delta(t)$ is given by:

$$\delta(t) \sim N((1-f)e^{-t/\tau_1}) + fe^{-t/\tau_2}) \tag{5.1}$$

where N is a normalization constant and f gives the mixing of the two characteristic times τ_1 and τ_2. The two time constants are computed for each DOM and each event, as they depend on the temperature. The result of the droop correction on an uncalibrated waveform can be seen in 5.1

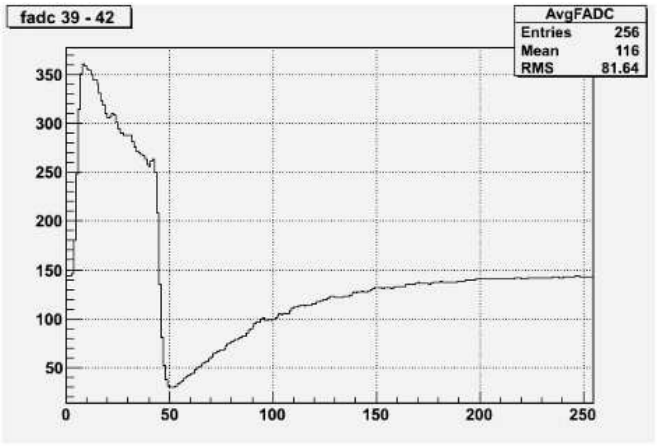

(a) Before Droop Correction

(b) After Droop Correction

Figure 5.1: An example waveform before and after double τ droop correction. The units in on the vertical axis are counts per bin. Taken from [53]

5.1.3 Feature Extraction

The semi-continuous calibrated waveform is deconvolved into the sequence of photo-electron arrival events by the process of feature extraction [34] [54]. The feature extraction process is an iterative fit to the calibrated waveform.

The assumed form of the waveform is given by the sum of n single SPE-like waveforms:

$$F^n(t) = b_0 + \sum_{k=1}^{n} A^k f(\frac{t - t^k}{\delta^k}) \tag{5.2}$$

Here b_0 is the baseline estimate. A^k, t^k, and δ^k are respectively the amplitude, time, and width of the kth pulse. The function $f(\zeta)$ is the SPE waveform.

The fit begins with $n = 1$ and proceeds with successively more SPE waveforms in the hypothesis function. At each iteration, the parameters are modified to minimize the χ^2 for the fit. The difference between the fitted waveform and the predicted waveform is then used to seed the time for the $n + 1$ pulse in the next iteration. The fit proceeds with successively more SPEs in the hypothesis until the χ^2 is small, stops improving, or we reach a predefined maximum number of pulses. The final result is then a linear combination of a number N of SPE-like waveforms.

5.1.4 Time Window Hit Cleaning

The IceCube trigger builds events by including all DOM readouts within a minimum 21 μs time window surrounding a trigger condition. If two trigger conditions occur sufficiently close to one another, their readout windows are combined into one long event. Because of this, it is not uncommon to have events where the

times between the first and last hits in the event can be up to 40 μs. In reality, a single muon will spend at most 3 μs within the detector volume. Consequently, all the hits from any single muon will arrive inside of a 4 μs window.

A sliding window of 6 μs is adjusted until the location containing the most hit DOMs is found. Hits that are outside of this window are thrown out. This procedure will clean out noise and only keep hits that are associated with the most energetic single muon.

5.2 Maximum Likelihood Reconstruction

The method of maximum likelihood is a well-known technique for estimating a set of unknown parameters $\mathbf{a}$ from a set of independent measured values $\mathbf{x} = \{x_i\}$. The technique proceeds by forming a likelihood function L

$$L(\mathbf{x}|\mathbf{a}) = \prod_i p(x_i|\mathbf{a}) \tag{5.3}$$

which is the likelihood of obtaining the measured values $\mathbf{x}$ under the assumption that the parameters are $\mathbf{a}$. Once we have this function, the parameters $\mathbf{a}$ that correspond to the maximum value of L are taken to be the measured parameters.

This technique can be used, with some modifications, in the context of reconstructing muon events in IceCube. Here, the unknown parameters $\mathbf{a}$ are parameters that determine an infinite muon track in the detector. Though it is possible to parameterize the muon track in a way that is unambiguous, it is typically assumed that the parameters that specify a muon track are some position x, y, z and time t along the track as well as the zenith angle θ and azimuth angle ϕ of the direction

the muon is coming from. Throughout this thesis, the zenith angle ranges from 0° (straight downgoing) to 180° (straight upgoing). There is one too many degrees of freedom in this set because the vertex position specified is arbitrary. To keep the likelihood function a function of the five independent parameters, the time t of the vertex is taken to be a constant value.

In the present definition we do not consider DOMs which are not hit as part of the measured signal, and the only DOMs that contribute to L are the DOMs which actually have a hit. The measured parameters x_i are then the position and times of the measured hits in the detector.

5.2.1 The Likelihood Function

The likelihood function of each of those measured hits, $p(x_i|\mathbf{a})$, must be constructed. It is useful, in considering the requirement for this function, to define the number t_{geo} which is the time that the PE is expected to arrive at a particular position, under the simple hypothesis of unscattered Cherenkov emission. Given the variables as defined in Figure 5.2, it can be shown that

$$t_{geo} = t_0 + \frac{\mathbf{p} \cdot (\mathbf{r}_i - \mathbf{r}_0) + d \cdot tan(\theta_c)}{c_{vac}} \tag{5.4}$$

where c_{vac} is the speed of light in a vacuum [55]. This is the simplest form of the equation under the assumption that the phase and group velocity of light in ice are the same. In truth, the calculation of t_{geo} uses the phase velocity to determine the angle of the Cherenkov cone, and the group velocity to determine the amount of time taken by the light to travel from the emission point to the detection point [56].

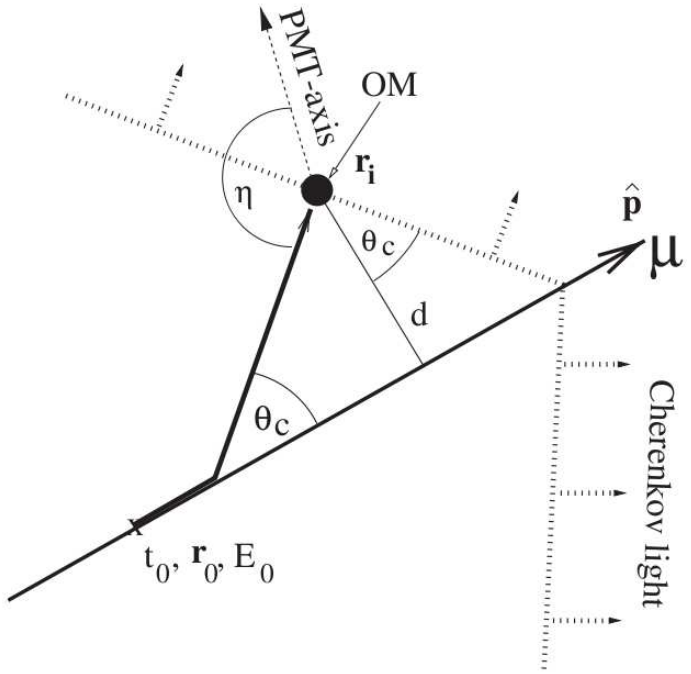

Figure 5.2: The coordinate system used for defining the single-hit likelihood function. θ_C is the Cherenkov angle, and $\hat{\mathbf{p}}$ is the momentum unit vector. The angle η is the angle of light arriving at the DOM. The vector $\mathbf{r}_i$ is the position of the DOM. t_0 and $\mathbf{r}_0$ are an arbitrary time and the corresponding position of the muon, and d is the distance of closest approach between the muon and the DOM. Taken from [55]

Given this definition of t_{geo}, the residual time t_{res} of a hit at time t_{hit} for a given hypothesis track is

$$t_{res} \equiv t_{hit} - t_{geo} \tag{5.5}$$

which is the amount of time by which the hit time differs from a pure Cherenkov hypothesis. A positive t_{res} would be a hit that arrives later than expected, for a given hypothesis.

For each hit in the detector (that is for each x_i), given some hypothesis $\mathbf{a}$ a residual can be assigned for that hit $t_{res,i}$ and the function $p(x_i|\mathbf{a})$ becomes a probability density function (PDF) in t_{res} for observing the hit at the given position with residual t_{res}. Furthermore, under the assumption that the distribution of residuals depends only on the distance d_i of the muon from the observation point and the angle η_i of the Cherenkov cone on the DOM, the single hit probability becomes a simple function of three variables, t_{res}, d_i, and η_i

$$p(x_i|\mathbf{a}) \rightarrow p(t_{res,i}, d_i, \eta_i) \tag{5.6}$$

5.2.2 The Pandel Function

The Pandel function [55] is an analytic estimate for the arrival time distribution of light emitted from a monochromatic, isotropic point light source in a medium where scattering is the dominant effect. The Pandel function is expressed relative to the residual time t_{res} and the distance d from the emission point to the detection point:

$$p_{pandel}(t_{res}, d) \equiv \frac{1}{N(d)} \frac{\tau^{(-d/\lambda)} t_{res}^{(d/\lambda - 1)}}{\Gamma(d/\lambda)} \cdot e^{-(t_{res} \cdot (\frac{1}{\tau} + \frac{c_{medium}}{\lambda_a}) + \frac{d}{\lambda_a})} \tag{5.7}$$

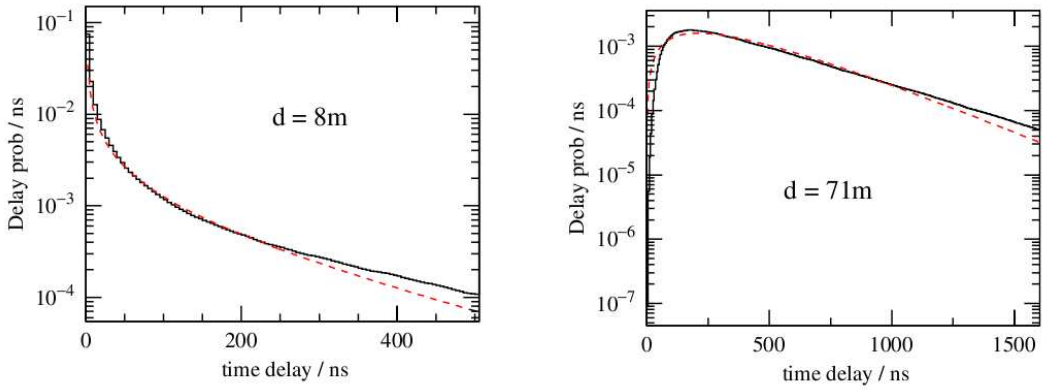

(a) (b)

Figure 5.3: Comparison of the parameterized Pandel function (dashed curves) with detailed simulation (black histogram) at different distances d from the muon track. Taken from [55]

$$N(d) = e^{-d/\lambda_a}(1 + \frac{\tau \cdot c_{medium}}{\lambda_a})^{-d/\lambda} \tag{5.8}$$

Here, $c_{medium} = c_{vac}/n$ is the speed of light in ice, λ_a the absorption length, $\Gamma(d/\lambda)$ the Gamma function and $N(d)$ a normalization factor. The free parameters are λ, an effective scattering length, and τ, a time scale. Figure 5.3 shows some examples of the pandel function compared to detailed simulation.

5.2.3 Forming the PDF

The Pandel function has some limitations. It is undefined for $t_{res} < 0$ and has a pole at $t_{res} = 0$ that causes numerical difficulties. The function also does not allow for PMT jitter or the fact that PMTs have an orientation relative to the source of the light. Various patches are applied in order to solve these problems.

To account for orientation of PMTs, the distance d is taken to be an effective

distance $d_{eff}(\eta)$ which accounts for the fact that the light is more scattered when the PMT is oriented away from the light source [57]. To account for the PMT jitter, we convolute the Pandel function with a Gaussian with width corresponding to the uncertainty in the timing (in the PMT or otherwise). In addition to the patching, a small constant offset is added to the PDF to account for the fact that a noise hit can occur at any time. The values for the free parameters of the pandel function are taken from [55].

5.2.4 Implementation

In practice, the fitter finds the minimum of the negative logarithm of the likelihood function ($-ln(L(\mathbf{x}|\mathbf{a}))$). This is equivalent to maximizing $L(\mathbf{x}|\mathbf{a})$, but is easier because of the scales of the numbers that are used. It also starts with a track hypothesis, a seed, and then varies the parameters in order to find the those that return the minimum negative log likelihood. In advanced reconstructions, a list of multiple track hypotheses are used as the basis of that many minimizations, and the most likely result of those minimizations is used as the best track. This procedure diminishes the chances that the minimizer finds a local minimum.

The software project Gulliver [58] implements all of these concepts for IceCube muon reconstruction. It is highly configurable, and allows for changing the minimization algorithms, PDFs, and seeds. Multiple maximum likelihood muon reconstructions were used in this thesis, but they did share a common minimizer. The minimization algorithm used is the simplex algorithm as implemented by the

TMinuit package in ROOT [59].

5.3 Specific Reconstructions Used

5.3.1 LineFit

The linefit reconstruction is a very fast computation that can return a good first guess of the direction of an event. It serves two main purposes. First, because of its speed and limited computational requirements, it is run at Pole on the triggered data stream. The resultant direction is used to filter out downgoing atmospheric muon background. Second, the linefit result is used as a seed to maximum likelihood muon reconstructions.

The linefit algorithm is a simple χ^2 fit based on the false assumption that light from the muon is a simple plane moving at a fitted velocity. Assuming the position of the hit i of a total of N_{hit} hits is given by $\mathbf{r}_i$ and the time of the first hit given by t_i, the equation for χ^2 is

$$\chi^2 = \sum_{i=1}^{N_{hit}} (\mathbf{r}_i - \mathbf{r} - \mathbf{v} \cdot t_i)^2 \tag{5.9}$$

where $\mathbf{r}$ is the reconstructed position and $\mathbf{v}$ is the reconstructed velocity vector. This equation can be minimized analytically and yields a solution:

$$\mathbf{r} = \langle \mathbf{r}_i \rangle - \mathbf{r} \cdot \langle t_i \rangle \tag{5.10}$$

$$\mathbf{v} = \frac{\langle \mathbf{r} \cdot t_i \rangle - \langle \mathbf{r}_i \rangle \cdot \langle t_i \rangle}{\langle t_i^2 \rangle \langle t_i \rangle^2} \tag{5.11}$$

where $\langle X_i \rangle$ denotes an average over all hits of the parameter X_i. Though it isn't used in this thesis, the reconstructed velocity $\mathbf{v}$ can be used to distinguish good fits

when $|\mathbf{v}|$ is close to c.

5.3.2 Single Photoelectron Fits

The single photo-electron (SPE) fits use the adjusted Pandel function described in section 5.2.3 to predict the arrival time of the first PE. The single iteration SPE fit uses the linefit reconstruction as a seed. The 32 iteration SPE fit uses the 1 iteration SPE fit as a seed. In addition, 32 other seed directions are chosen according to the pseudo-random sobol sequence [60]. The sobol sequence differs from a normal random sequence of numbers in that it uniformly samples a space rather than randomly sampling it. The algorithm fills in empty space evenly as more and more samples are chosen. In this way, 33 minimizations are carried out on track seeds that uniformly cover the space of possible track results. All other settings are equivalent to the 1 iteration SPE fit.

The result of these SPE fits is not only a best fit track, but also various quality parameters. The best of these is the reduced log-likelihood (rlogl), which is simply the final minimized log-likelihood divided by the number of degrees of freedom involved in the minimization. This is done because the log-likelihoods themselves cannot be meaningfully compared to each other, as track with many participating DOMs will be penalized for having many likelihoods to add together. The reduced log-likelihood is a good indication of the quality of a fit and is especially good at separating signal from background.

Another important quality parameter is the number of direct hits (ndir). A

direct hit is defined as a DOM that has a t_{res} such that:

$$-15 \text{ ns} > t_{res} > 75 \text{ ns} \tag{5.12}$$

This condition suggests that the hit arrives without much scattering and therefore the hit is trusted to convey more reliable information about the track geometry. A track with many direct hits has a higher quality than an event with only a few direct hits.

The convoluted pandel PDF described above accurately describes the expected arrival time of one PE, but it breaks down when trying to describe the arrival time of the first of many PEs. In this situation, the peak expected arrival time for the first photon is always much later than the first of many photons, and the fitter tries to match each first photon to the later peak. This causes a shift in the vertex of the track to earlier times, moving all the hits out of the direct hit window. This causes well reconstructed high energy tracks to have zero direct hits. For this reason, the SPE number of direct hits is never explicitly cut upon, but instead used as an input to a machine learning algorithm discussed in section 6.1.

5.3.3 Multiple Photoelectron Fit

The PDFs discussed so far accurately model the possible arrival times of the first PE at a DOM. For DOMs, with multiple PE arrival times, the SPE fits will not model the likelihood correctly for PEs beyond the first. The correct PDF for those PEs is:

$$\text{MPE}_n(t_{res}) = n \cdot \text{SPE}_n(t_{res}) \cdot [t_{res} \cdot \int \text{SPE}_n(t)dt]^n \tag{5.13}$$

In practice, using this PDF is difficult because the convoluted pandel PDF cannot be integrated analytically, whereas the plain pandel PDF can. The solution used in this thesis is to use the plain pandel for the PDF under the integral in equation 5.13, and a convoluted pandel for the PDF outside of the integral. This way, the jitter is properly accounted for on the first PE's PDF, but not on the subsequent ones. The result is a fit that achieves better angular resolution than the SPE fits.

This approximation breaks down for tracks that pass very close to hit DOMs, which leads to some problems. First, minimizations that start with seed tracks far away from the true muon direction fail to find the true minimum, and can sometimes return false minimums. Therefore, the MPE reconstructions are only run with one seed: either the 1 iteration SPE or the 32 iteration SPE reconstruction result. Secondly, the error on the resultant track cannot be correctly mapped by the paraboloid fit (section 5.3.4). Finally, other quality parameters from the MPE fit, such as reduced log-likelihood, have worse separation of signal and background than those taken from the 32 iteration SPE fit. Therefore, the direction of the MPE track is only used as the best direction reconstruction when the paraboloid error on that direction is not necessary.

5.3.4 Paraboloid Fit

The paraboloid fitter [61] studies the behavior of the likelihood function around a seed, presumably a previously obtained reconstruction result. After transforming the coordinate space to one centered on the direction of the seed track, it then

attempts to fit a paraboloid to the likelihood space around that track.

The important result of the paraboloid fitter is the paraboloid sigma σ. It is calculated from the sigmas on the major and minor axis of the fitted paraboloid:

$$\sigma \equiv \sqrt{\frac{1}{2}(\sigma_1^2 + \sigma_2^2)} \tag{5.14}$$

The paraboloid sigma provides a good estimate of the pointing error of the seed track. This can be demonstrated by running the paraboloid fitter on simulated data, and generating a pull plot. A pull plot in this context is the difference between truth and reconstructed directions divided by the paraboloid estimate of the error on that direction. Figure 5.4 shows this for upgoing neutrino simulation weighted to an E^{-2} spectrum and reconstructed with a 32 iteration SPE fitter. The widths of Gaussian distributions fitted to the pull plots are very close to one which proves that the paraboloid sigma is a good estimate of error.

Pull plots generated with paraboloid sigmas calculated from MPE fits show bad agreement with true reconstruction errors, due to the approximations made during the fits. Therefore, the MPE reconstruction result is only used as the final direction when the paraboloid error estimate is not necessary.

5.3.5 Bayesian Up/Down Fit

In Bayesian reconstruction we multiply the regular likelihood function (which gives the probability of the measured data given an event hypothesis) with a bias function which depends only on the event hypothesis and not on the actual event data. In this case, the bias is used as a way to include our knowledge of the char-

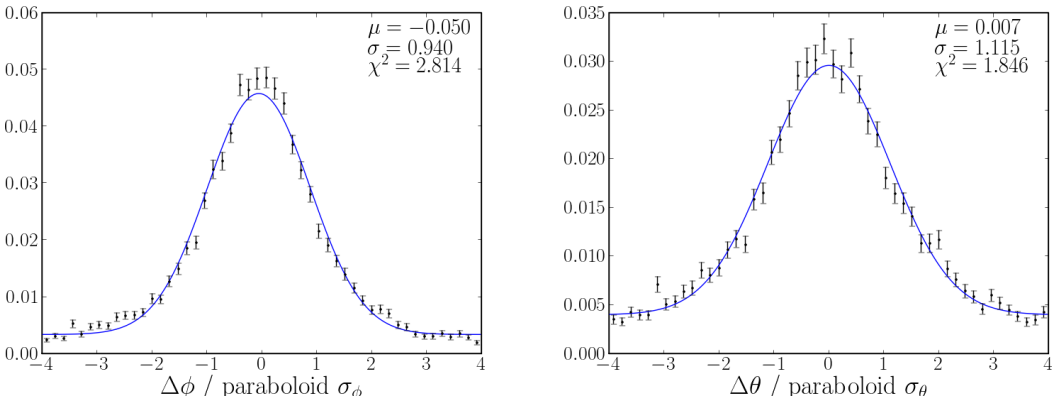

(a) Zenith Pull Plot

(b) Azimuth Pull Plot

Figure 5.4: Paraboloid pull plots run on neutrino simulation weighted to an E^{-2} spectrum. Panel (a) shows the pull plot in zenith angle and panel (b) shows it in azimuth. The mean (μ), width (σ), and reduced chi-squared (χ^2) of a fitted Gaussian are shown for each plot.

acteristics of the sample of events which we are reconstructing (ie. that downgoing tracks dominate the sample). In this thesis, a three parameter function is used to model the zenith distribution of downgoing muons:

$$w = a_0 \cdot [cos(zeinth)]^{a_1} \cdot e^{\frac{-a_2}{cos(zenith)}} \tag{5.15}$$

with $a_0 = 2.49655 \times 10^{-7}$, $a_1 = 1.67721$, and $a_2 = 0.778393$. In this purely Bayesian approach, an upgoing track should only be found if its regular likelihood is so good that it is found by the minimizer even with the bias terms added. This fit uses the same seeds as the 32 iteration SPE fit, derived from the SOBOL pseudo-random sequence.

The Bayesian likelihood ratio is the important result of this reconstruction.

This quality parameter is defined as:

$$\mathcal{R}_{bayesian} = ln(L_{Bayesian}) - ln(L_{SPE}) \tag{5.16}$$

where $L_{Bayesian}$ is the likelihood from this reconstruction and L_{SPE} is the unbiased likelihood. Better tracks will be highly favored as upgoing, and will thus have negative Bayesian likelihood ratios.

5.3.6 Umbrella Fit

The umbrella reconstruction simply constrains the minimizer to the hemisphere opposite some seed track. In this thesis, that seed is the 32 iteration SPE fit. The likelihood ratio between this reconstruction and the 32 iteration SPE reconstruction can then be calculated:

$$\mathcal{R}_{umbrella} = ln(L_{umbrella}) - ln(L_{SPE}) \tag{5.17}$$

Again, better tracks will have a much higher 32 iteration likelihood than a fit constrained to the opposite hemisphere, and so they will have negative umbrella likelihood ratios. The reduced log likelihood of the umbrella fit alone showed some separation power and so it was also used.

5.3.7 Split Reconstruction

The split reconstruction is carried out by splitting the pattern of hits into two subsets. This is done by calculating the average time of the hits, and then splitting the event into hits that occur before that time and hits that occur after. A

1 iteration SPE reconstruction seeded by linefit is done on both subsets of hits. The minimum zenith angle (most downgoing track) between those two fits is chosen as a quality parameter. Good tracks will reconstruct in the same upgoing direction when split into two. Coincident atmospheric muons can appear to be an upgoing track by hitting the bottom of the detector and later the top, and will thus return one downgoing track with this reconstruction. This minimum zenith angle is particularly good at cutting out this type of event.

5.3.8 Energy Reconstruction

Especially in the high background regime above the horizon, energy reconstructions are necessary to differentiate neutrinos from background atmospheric muons or neutrinos. There are a couple of methods used in this thesis for estimating the energy of an event. The first is using two simply calculated variables that are related to total energy of primaries: total hits and total integrated charge. These two variables can both be easily counted after the feature extraction has been performed on all the waveforms. They have many benefits over similar variables including their separation power, their ability to closely track the actual energy of events, their superior agreement between data and simulation, and their consistency throughout all ice layers.

A software package called MuE [62] is used to calculate an energy proxy. The reconstruction is seeded by the MPE fit, and then calculates what is equivalent to photons per track length. The result can be calibrated to represent the initial energy

of the primary, but the uncalibrated result shows good correlation with the energy of the primary. Therefore, the simpler uncalibrated result is used in this thesis.

Chapter 6

Analysis Techniques

6.1 Support Vector Machines

Support Vector Machines (SVMs) are a set of related supervised learning methods used for classification and regression. An SVM will take two sets of input data that are classified by n-dimensional vectors, and create a separating hyperplane in that space. In particular, an SVM will find the separating hyperplane that is farthest away from any data point in either class. This is called the maximum-margin hyperplane, as the margin is defined as the distance from the hyperplane to the nearest data point.

In this analysis, the two sets of data points are the simulated signal (ν_μ from GRBs) and the measured off time background (made up of atmospheric muons and atmospheric neutrinos). Various reconstructed quality parameters, described in section 5.3, make up the dimensions in the space where the hyperplane sits. Once the maximum-margin hyperplane is found, the distance of any new event to that hyperplane can be calculated, and this new parameter provides an excellent indication as to whether it is signal or background.

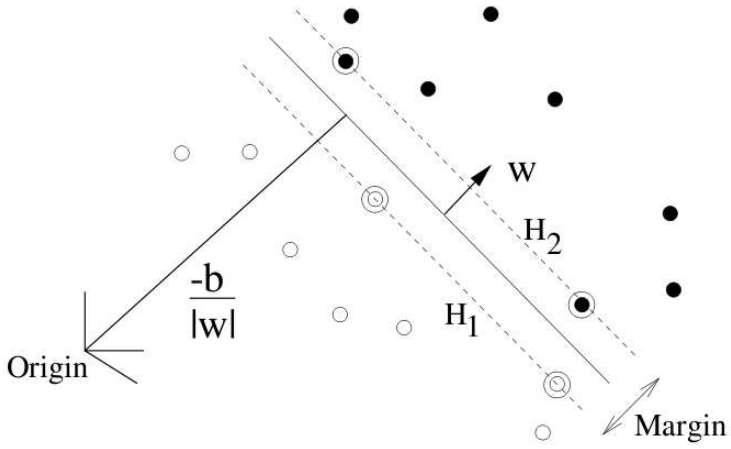

Figure 6.1: The two sets of circles represent two sets of data that are separable by a linear hyperplane. The maximum-margin hyperplane is shown as the solid line, and the dashed lines show the borders of the margin. Data points on the borders of the margin are called support vectors. Taken from [63]

6.1.1 Linearly Separable Case

In order to understand the theory behind SVMs, it's useful to start from the very basic problem they were created to solve, and then slowly add complexity. The first very basic problem involves two sets of data points which can be separated by a linear hyperplane (ie. a line in two dimensional space, a plane in three dimensional space, etc.). This situation is illustrated in two dimensions in Figure 6.1.

Formally, two sets of points can be defined in this way:

$$\mathscr{D} = \{(\mathbf{x}_i, c_i) \mid \mathbf{x}_i \in \mathbb{R}^p, c_i \in \{-1, 1\}\}_{i=1}^{n} \tag{6.1}$$

where the c_i is either 1 or -1, indicating the class to which the point $\mathbf{x}_i$ belongs. Each $\mathbf{x}_i$ is an p-dimensional real vector. The goal is to find the maximum-margin

hyperplane which divides the points having $c_i = 1$ from those having c_i = -1. Any hyperplane can be written as the set of points $\mathbf{x}$ satisfying

$$\mathbf{w} \cdot \mathbf{x} - b = 0 \tag{6.2}$$

The vector $\mathbf{w}$ is a normal vector that is perpendicular to the hyperplane. The parameter $\frac{b}{\|\mathbf{w}\|}$ determines the offset of the hyperplane from the origin along the normal vector $\mathbf{w}$. So $\mathbf{w}$ and b must be chosen to maximize the margin, or the distance between the parallel hyperplanes that are as far apart as possible while still separating the data. These parallel hyperplanes are the border of the margin, and can be described by the two equations

$$\begin{aligned} \mathbf{w} \cdot \mathbf{x} - b &= 1 \\ \mathbf{w} \cdot \mathbf{x} - b &= -1 \end{aligned} \tag{6.3}$$

If the training data is linearly separable, these two hyperplanes can be chosen so that there are no points between them and the distance between them can be maximized. This distance is $\frac{2}{\|\mathbf{w}\|}$, so $\|\mathbf{w}\|$ must be minimized. The expression $\frac{1}{2}\|\mathbf{w}\|^2$ is minimized instead, since it can be shown to yield the same solution, and is mathematically more convenient. Since no data points can fall into the margin, this minimization is subject to the constraint that for each i:

$$c_i(\mathbf{w} \cdot \mathbf{x}_i - b) \geq 1, \text{ for all } 1 \leq i \leq n \tag{6.4}$$

Formulating this problem in terms of Lagrangian multipliers will be beneficial for two reasons. First, it will allow the constraints in equation 6.4 to be expressed as constraints on the multipliers themselves. Second, in the reformulation of the

problem, the training data will only appear in the form of dot products between vectors. This crucial property will allow generalization to the non-linear case (section 6.1.2). This new formulation gives the following Lagrangian:

$$L_P \equiv \frac{1}{2}\|\mathbf{w}\|^2 - \sum_{i=1}^{n} \alpha_i c_i (\mathbf{w} \cdot \mathbf{x}_i - b) + \sum_{i=1}^{n} \alpha_i \tag{6.5}$$

L_p must now be maximized while holding its derivatives with respect to all α_i equal to zero, and all $\alpha_i \geq 0$.

Because of some specific properties of this new formulation, it can be equivalently solved in its dual form. In this Wolfe dual [64], a L_P is now maximized while holding its gradient with respect to $\mathbf{w}$ and b equal to zero, as well as all $\alpha_i \geq 0$. This results in the new conditions:

$$\mathbf{w} = \sum_i \alpha_i c_i \mathbf{x}_i \tag{6.6}$$

and

$$\sum_i \alpha_i c_i = 0 \tag{6.7}$$

Substituting them into equation 6.5 yields:

$$L_D = \sum_i \alpha_i - \frac{1}{2} \sum_{i,j} \alpha_i \alpha_j c_i c_j \mathbf{x}_i \cdot \mathbf{x}_j \tag{6.8}$$

In the solution, those points for which $\alpha_i > 0$ are called support vectors, and lie on the border of the margin. All other points have $\alpha_i = 0$. For this simple linear separable case, the support vectors are the critical elements of the training set. All other points can be removed, and the same separating hyperplane will be the solution.

6.1.2 Non-Separable Linear Case

In real applications, data is usually not cleanly separable by a linear hyperplane. A soft margin formulation of the SVM can allow for mislabelled examples in the minimization [65]. This formulation will return a hyperplane that splits the examples as cleanly as possible, while still maximizing the distance to the nearest cleanly split examples. This is done through the introduction of slack variables, ξ_i, which measure the degree of misclassification of the datum $\mathbf{x}_i$ (see Figure 6.2). The constraint then becomes:

$$c_i(\mathbf{w} \cdot \mathbf{x}_i - b) \geq 1 - \xi_i, \text{ for all } 1 \leq i \leq n \tag{6.9}$$

with $\xi_i \geq 0$. Thus, for an error to occur, the corresponding ξ_i must exceed unity, and $\sum_i \xi_i$ is an upper bound on the number of training errors. Hence, a natural way to assign an extra cost for errors is to change the function to be minimized from $\|\mathbf{w}\|^2/2$ to $\|\mathbf{w}\|^2/2 + C\sum_i \xi_i$, where C is a parameter to be chosen by the user. A larger C corresponds to assigning a higher penalty to errors. The Wolfe dual problem then becomes:

$$L_D \equiv \sum_i \alpha_i - \frac{1}{2}\sum_{i,j} \alpha_i \alpha_j c_i c_j \mathbf{x}_i \cdot \mathbf{x}_j \tag{6.10}$$

which must be maximized, subject to the following constraints:

$$0 \leq \alpha_i \leq C \tag{6.11}$$

and

$$\sum_i \alpha_i c_i = 0 \tag{6.12}$$

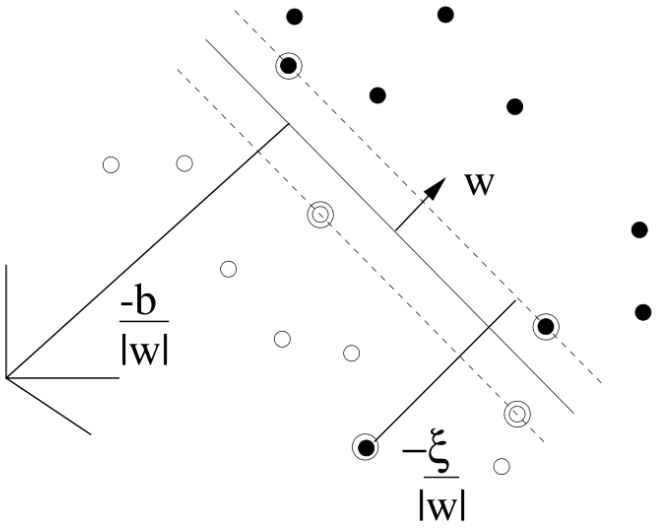

Figure 6.2: An example of the non-separable linear case. Taken from [63].

and the solution is again given by:

$$\mathbf{w} = \sum_{i=1}^{N_s} \alpha_i c_i \mathbf{x}_i \tag{6.13}$$

where N_s is the number of support vectors.

6.1.3 Non-Linear Case

The above examples have only dealt with the case in which the resulting separating hyperplane is linear. Allowing the hyperplane to be non-linear would greatly increase its separating power. This is done by mapping the original set of points into a higher dimensional space where there is a linear separating hyperplane may exist. Finding a mapping, ϕ, that does this would be very difficult. Fortunately,

the above algorithms only depends on the data through dot products, which would appear as $\phi(\mathbf{x}_i) \cdot \phi(\mathbf{x}_j)$ in the higher dimensional space. This dot product can be replaced with a kernel function [66] [65]:

$$k(\mathbf{x}_i, \mathbf{x}_j) = \phi(\mathbf{x}_i) \cdot \phi(\mathbf{x}_j) \tag{6.14}$$

This is called a kernel trick which is an application of Mercer's theorem that states that any continuous, symmetric, positive, semi-definite kernel function can be expressed as a dot product in higher dimensional space. After this replacement, the solution, $\mathbf{w}$, will be a hyperplane in some higher dimensional space

There are many kernel functions to choose from, and each one has advantages and disadvantages. In this thesis, the Radial Base Function was used:

$$k(\mathbf{x}_i, \mathbf{x}_j) = e^{-\gamma \|\mathbf{x}_i - \mathbf{x}_j\|^2} \tag{6.15}$$

with $\gamma > 0$. This kernel has the advantage that there are a small number of parameters to determine (namely just γ), the result is constrained to (-1,1) causing less numerical difficulties, and the result is defined for all inputs [67].

6.2 Model Discovery Factor

It is desirable to optimize the analyses presented here in order to maximize the chances of an interesting discovery rather than to simply set the best upper limit on potential source fluxes. In order to do this, the Model Discovery Factor (MDF) is used [68].

The MDF can best be described through its application to an example Poisson counting experiment. In this experiment, a selection cut can be chosen that will

leave some level of background events, expressed as μ_b, and some expected number of signal events, expressed as μ_s. The experiment is searching for signal events believed to be described by a flux model $A\Phi(E)$, where E is the true energy of the incident particle. The shape of the signal flux as a function of particle energy is $\Phi(E)$, and the total rate of expected signal events is given by the flux normalization, A. After averaging the flux over the detector response $\epsilon(E)$, we find the number of expected signal events:

$$\mu_s = \int A\Phi(E)\epsilon(E)dE \tag{6.16}$$

After the selection cut is set, the data is unblinded and n_{obs} events are found.

Now, in the absence of signal the probability of making some observation, n_{obs}, or a more extreme one in this experiment is $P(\geq n_{obs} \mid \mu_b)$. When this probability is less than some small number, α, a discovery can be claimed. A reasonable choice for α might be $\alpha = 5.73 \times 10^{-7}$ (or the area in the two-sided 5σ Gaussian tails). For a given α, n_{crit} can be calculated. This is the minimum number of events needed to be observed in order that a probability less than α still be reported.

If a real signal of strength μ_s is also present, then the probability (statistical power $1 - \beta$) that we would observe n_{crit} or more events is:

$$1 - \beta = P(\geq n_{crit} \mid \mu_b + \mu_s) \tag{6.17}$$

Now the least detectable signal, expressed as μ_{lds}, can be calculated. The least detectable signal is the value of μ_s that would produce an observation leading to p-values less than α in a fraction of $1 - \beta$ experiments. In other words, it is the minimum value of μ_s that satisfies equation 6.17. The Model Discovery Factor is

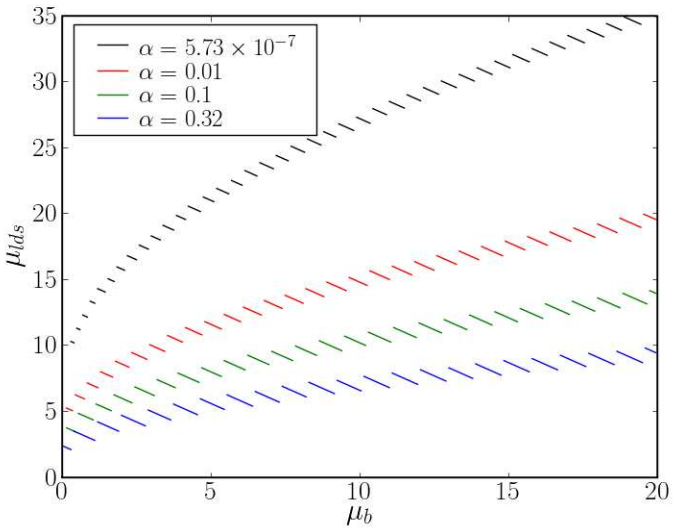

Figure 6.3: Least detectable signal for various confidence levels, α. The LDS values are all calculated for $1 - \beta = 0.9$. The breaks in the curves occur when n_{crit} moves to the next highest integer.

then:

$$\text{MDF} = \frac{\mu_{lds}(\mu_b, \alpha, \beta)}{\mu_s} \tag{6.18}$$

which should then be minimized as a function of the selection cuts necessary to produce μ_b and μ_s. This will minimize the true signal flux required to make an observation at significance level α with probability $1 - \beta$. The MDF can also be described as the factor that the original normalization factor, A, must be multiplied by in order to guarantee an observation at significance level α with probability $1-\beta$.

As an example, take $\mu_b = 3.0$, require $\alpha = 5.73 \times 10^{-7}$ and $1 - \beta = 0.9$. Then $n_{crit} = 16$ ($P(\geq 16 \mid 3.0) = 1.24 \times 10^{-7}$), $\mu_{lds} + \mu_b = 21.3$ ($P(\geq 16|21.3) = 0.90$), leading to $\mu_{lds} = 18.3$. We can calculate μ_{lds} as a function of μ_b for various values of α and $1 - \beta$. The results are shown in Figure 6.3.

6.3 Unbinned Likelihood Method

Data around a GRB can potentially be described by two hypotheses:

- H_0: The data consists solely of background atmospheric muon and atmospheric neutrino events
- H_S: The data consists of background events as well as some astrophysical neutrino events produced by a GRBs

The likelihood of obtaining the data given each hypothesis is calculable, and the ratio of those likelihoods, or equivalently the log of the likelihood ratio, serves as a powerful test statistic:

$$\lambda = ln\left[\frac{P(Data \mid H_S)}{P(Data \mid H_0)}\right] \tag{6.19}$$

Larger values of λ indicate the data is less compatible with the background hypothesis H_0. The probability density functions $P(Data \mid H_0)$ and $P(Data \mid H_S)$ are calculated using knowledge of the spatial and energy distribution of the background events and astrophysical neutrino events.

In this thesis, the extended maximum likelihood function is used [69]. In the standard maximum likelihood, the probability density function (PDF), $P(x;a)$, is normalized to 1. In the method of extended maximum likelihood the normalization n_t of the PDF-equivalent function $Q(x;a)$ (in our case $Q(x;n_s) = n_s S(x) + n_b B(x)$) is not fixed. Thus:

$$\int Q(x;a)dx = n_t = n_t \int P(x;a)dx \tag{6.20}$$

This is appropriate in experiments like IceCube where it is not known in the beginning how many events will be observed in a given amount of time. The additional information of how likely it is to observe the actual number of events given the expected mean number of events n_t can be incorporated into the likelihood by multiplying the standard maximum likelihood function with the corresponding Poisson probability:

$$\mathcal{L}_{EML} = e^{-n_t} \frac{n_t^N}{N!} \times \prod_{i=1}^{N} P(x_i; a) \tag{6.21}$$

After taking the logarithm of both sides and omitting the $N!$ as it doesn't depend on a, this results:

$$ln(\mathcal{L}_{EML}) = -n_t + N ln(n_t) + \sum_{i=1}^{N} ln(P(x; a)) \tag{6.22}$$

$$= -n_t + \sum_{i=1}^{N} ln(n_t P(x; a)) \tag{6.23}$$

$$= -n_t + \sum_{i=1}^{N} ln(Q(x; a)) \tag{6.24}$$

This is the extended maximum likelihood function used.

At this point, the signal and background PDFs ($\mathcal{S}_i$ and $\mathcal{B}_i$ respectively) for each event need to be defined. The particular PDFs used in this thesis are described in section 8.3. Once this is done, a likelihood function for the signal and null hypotheses can be constructed:

$$ln(\mathcal{L}) = -n_s - n_b + \sum_{i=1}^{N} ln(n_s \mathcal{S}_i + n_b \mathcal{B}_i) \tag{6.25}$$

$$ln(\mathcal{L}_0) = -n_b + \sum_{i=1}^{N} ln(n_b \mathcal{B}_i) \tag{6.26}$$

and then the ratio of likelihoods is:

$$\lambda = ln(\mathcal{R}) = ln(\frac{\mathcal{L}}{\mathcal{L}_0}) = -n_s + \sum_{i=1}^{N} ln(\frac{n_s \mathcal{S}_i}{n_b \mathcal{B}_i} + 1) \tag{6.27}$$

This ratio is the test statistic. For any configuration of the data, λ is minimized as a function of n_s to find the most likely number of signal events, and the resulting likelihood of the signal hypothesis. Many trials are done with randomized background, and λ is measured for each. The resulting distribution will allow the evaluation of the significance of observed values of λ.

Chapter 7

Northern Hemisphere Search

An analysis procedure to search the IceCube data taken during 41 GRB triggers in the northern hemisphere is developed in order to maximize the chances of a neutrino discovery. The data taken during the bursts is first set aside, or blinded, and off-time data is used to estimate the background level. The on-time data from each of the bursts is then combined and a binned search for an aggregate signal above the expected background is done. No excess is found and a limit on the neutrino emission is calculated.

7.1 GRB Triggers

The 41 GRB triggers listed in table 4.2 as northern hemisphere bursts are included in this search. The on-time window for each GRB is defined as the time between T1 and T2 padded on each side by one second. T1 and T2 define the beginning and end of the T_{100} time window and this is the time period during which 100% of the gamma-ray emission is detected. The padding to that period allows for small errors in the measurement of the beginning and end of the burst emission and also gives a meaningful window to search for short bursts with $T_{100} \sim 0.1$ s. Taking the on-time windows for all the bursts together yields a total on-time window of 4960.6 seconds which is ultimately searched.

7.2 IceCube Data

7.2.1 Background

When optimizing to maximize the chances of a discovery, hard cuts are required. Trigger level data taken by the GRB filter does not provide enough off-time statistics to properly estimate the background level at a hard cut level. For this reason, the analysis is carried out on the full muon filtered dataset described in section 3.4. During optimization of the analysis, IceCube data taken during a two hour period surrounding each burst is blinded, and the rest of the data is considered the background off-time sample. The livetime for this background sample is 272.3 days.

7.2.2 Simulation

Cosmological neutrinos from GRBs are simulated with the Monte Carlo chain described in section 3.7. The neutrinos are generated at an E^{-1} spectrum, and then re-weighted to the summed spectrum shown in figure 4.3.

Atmospheric muons and neutrinos are also simulated. These background simulation datasets are not used in the optimization of the analysis. They are only compared to background data in order to verify that cuts on quality parameters are affecting the signal as expected. Single and double atmospheric muon backgrounds are simulated in two different datasets. Neutrinos are also generated at an E^{-2} spectrum and then re-weighted to the atmospheric neutrino energy spectrum described in section 3.6.

7.2.3 Processing

After satellite transfer of the muon filtered data, more processing and filtering is applied offline. All of the reconstructions mentioned in section 5.3 are completed. The following cuts are applied during the processing in order to keep the computing time necessary for all the reconstructions at a manageable level:

- 1 iteration SPE reduced log likelihood ≤ 13
- 1 iteration SPE zenith ≥ 80
- 32 iteration SPE zenith ≥ 80

After all of this processing and filtering, the remaining dataset is referred to as the offline level 3 muon filtered data sample. The entire level 3 dataset still contains $\sim$7 million events and it still lacks the MPE reconstruction seeded by the 32 iteration SPE. It's necessary to make further cuts so that the processing time required for this reconstruction is reasonable. Figure 7.1 shows the power that cuts on some available quality parameters have in discriminating signal from background at this point. A cut on the Bayesian likelihood ratio retains the most signal while reducing the background by the necessary factor of two. Unfortunately, the necessary cut at a Bayesian likelihood ratio of -20 is located right at the peak of both the signal and background distributions (figure 7.2). Small changes to the cut would result in large differences in the resulting datasets. For this reason, a cut on the more stable 32 iteration reduced log likelihood is chosen at 11. After this cut, the MPE reconstruction is run with the 32 iteration SPE fit as a seed and the resulting dataset is referred to as level 4. Table 7.1 shows the number of events expected in the summed on-time window at level 3 and 4 for various datasets.

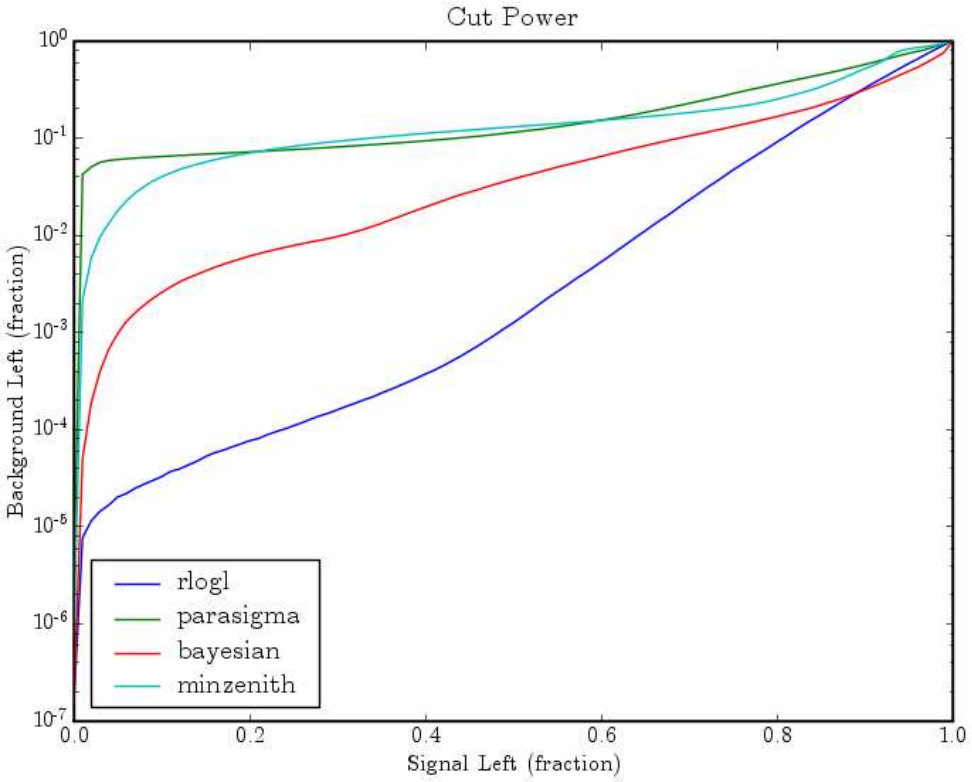

Figure 7.1: The cut power of various variables in separating signal from background is shown. The curves begin in the upper right corner, and as the cuts are increased, the curves trace how much signal and background are left.

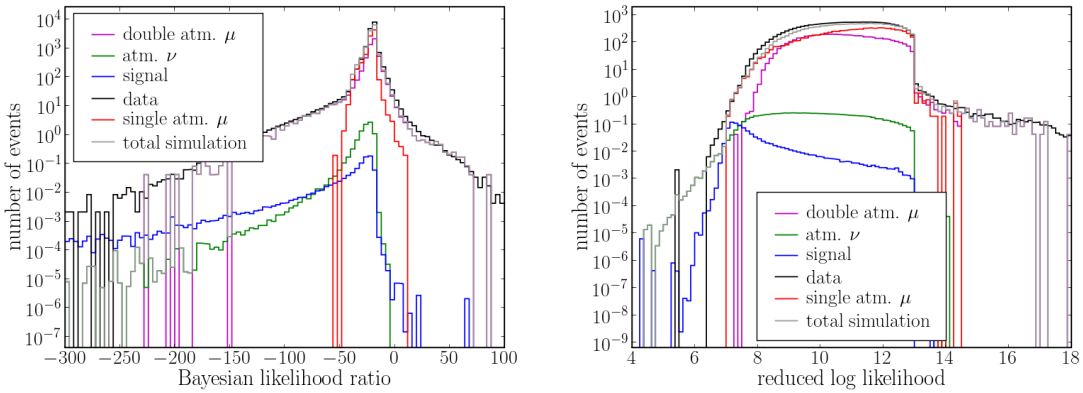

(a) Bayesian Likelihood Ratio

(b) 32 Iteration SPE Reduced Log Likelihood

Figure 7.2: Level 3 Quality Parameters.

Table 7.1: Events expected in the on-time window

Dataset	Level 3	Level 4
signal	0.0529	0.0488
background	15420	7680
total simulated background	13017	6029
single atmospheric μ	8040	3262
double atmospheric μ	4968	2760
atmospheric ν	8.708	6.325

7.3 Support Vector Machine

A Support Vector Machine (SVM) is used to combine quality cuts for separating signal and background. The package SVM^{light} [70] is used to implement this SVM. Nine quality parameters are given to the SVM to train on. They are:

- 32 iteration SPE zenith
- 32 iteration SPE azimuth
- 32 iteration SPE rlogl
- 32 iteration SPE ndir

- 32 iteration SPE paraboloid sigma
- 32 iteration SPE Bayesian likelihood ratio
- 32 iteration SPE umbrella likelihood ratio
- 32 iteration SPE umbrella rlogl
- 1 iteration split reconstruction minimum zenith

All the well understood variables that this analysis had access to are used in the SVM. The zenith and azimuth are also used to classify events so that the SVM will find that events from different directions deserve looser or stronger cuts. All of the used parameters are plotted at level 4 in figure 7.3 and 7.4.

When doing an SVM classification, the kernel and various SVM settings need to be chosen [67]. In this case, those settings are the cost factor (j), the margin (c), and the kernel parameter (g). A wide grid search is performed in order to find the general area where the best SVM settings could be found. This area is then zoomed in on with a finer grid to find the absolute best settings.

A cross-validation technique was carried out at each node of the grid searches in order to test the separating power of the SVM at that node. Cross-validation begins by splitting the available training data into five equal parts. One of those five subsets is then classified using an SVM trained on the other four subsets. Each of the five subsets is classified in the same manner. This process is meant to prevent the SVM from becoming over-trained on the specific training data chosen.

The effectiveness of each classification is evaluated by executing a simplified version of the final analysis optimization. The classified signal and background datasets are weighted to reflect the number of events expected in the total 4960.6

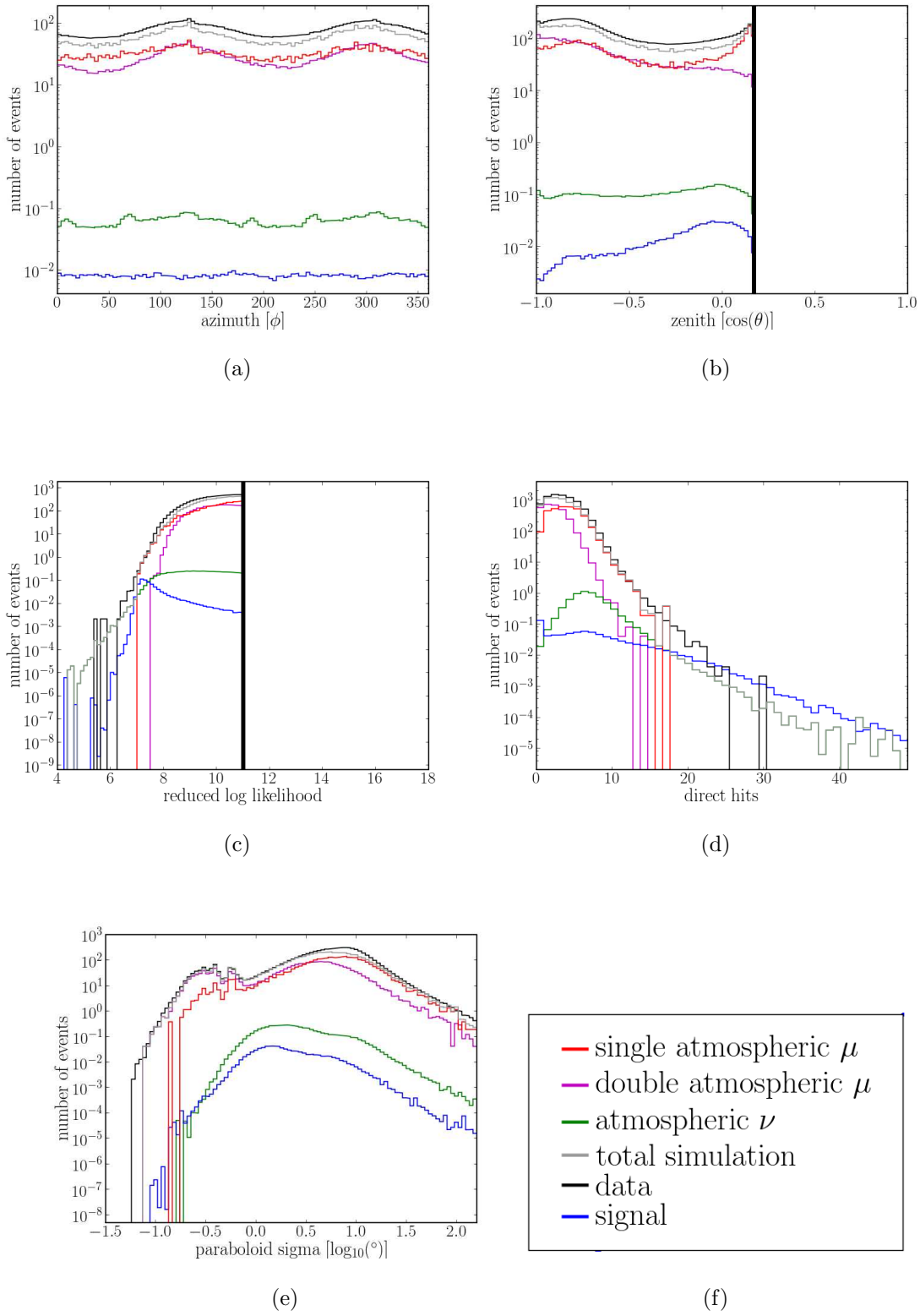

Figure 7.3: Level 4 Quality Parameters used to train the SVM.

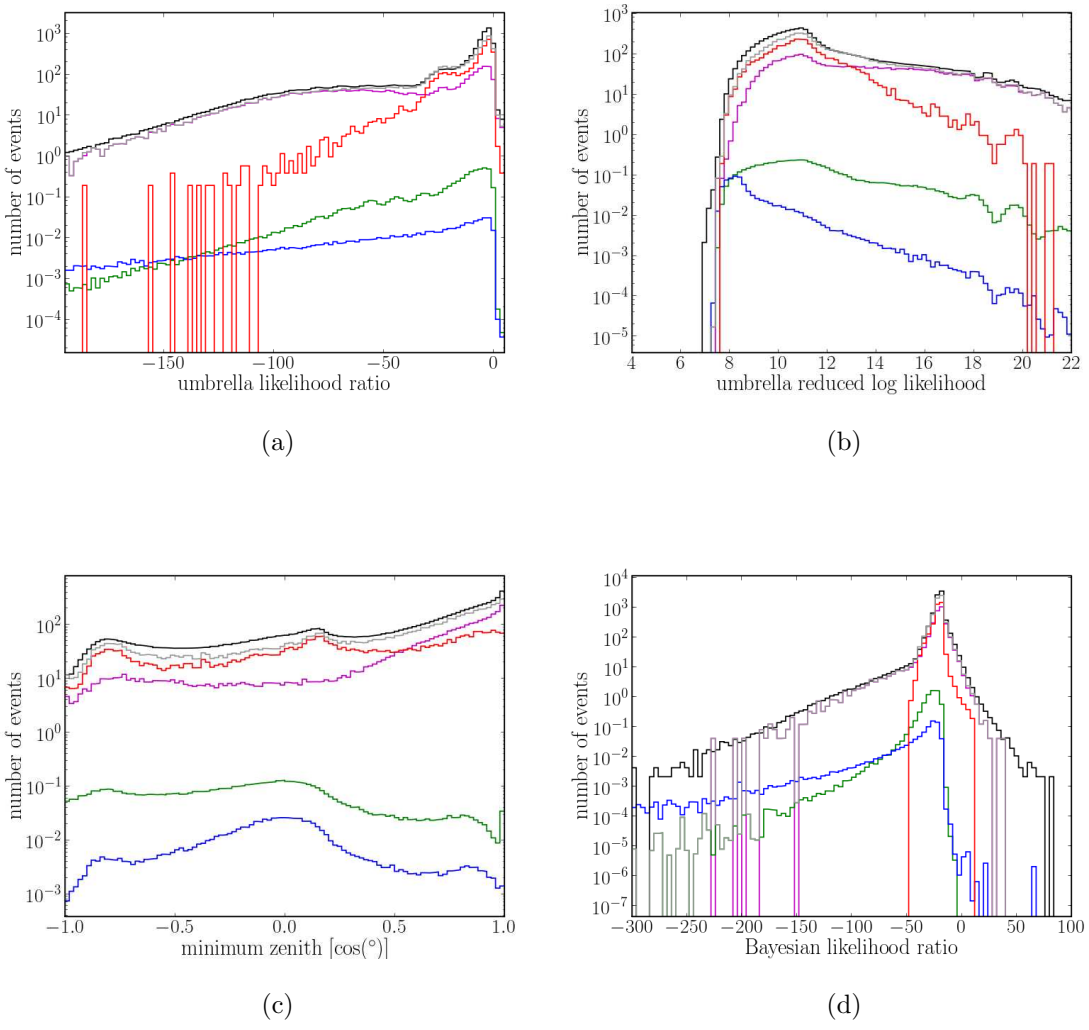

Figure 7.4: (continued) Level 4 Quality Parameters used to train the SVM.

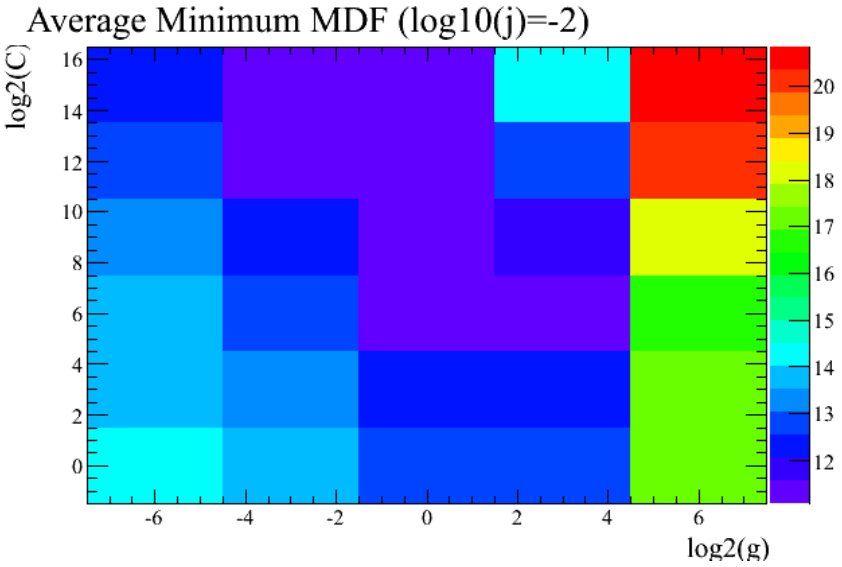

(a)

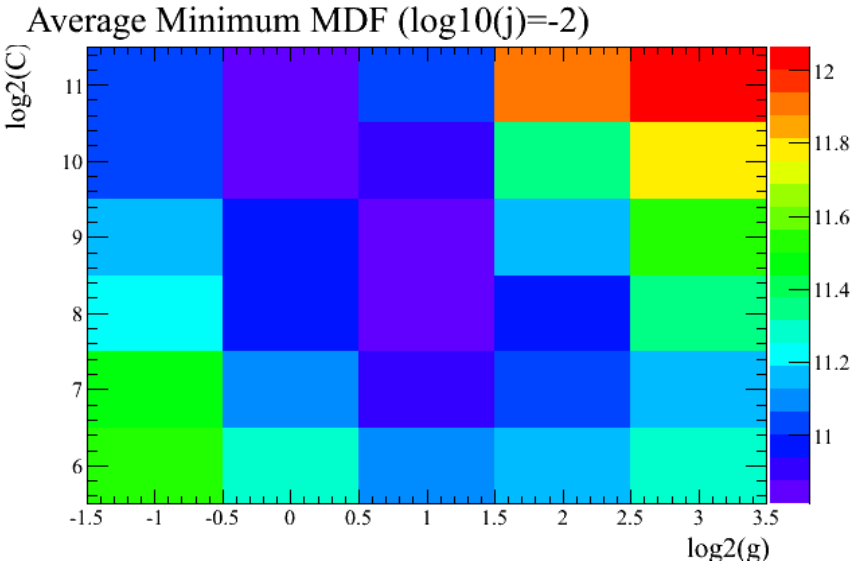

(b)

Figure 7.5: The resulting average MDFs from each SVM generated with the listed settings. Panels (a) shows the results of the wide grid search and panel (f) shows the results of the fine grid search.

second on-time window in a solid angle of radius 3 degrees. The cut on the SVM classifier that minimizes the 5 sigma, 90 percent confidence MDF is found. The minimum MDF resulting from the classification of each of the five subsets of training data are averaged to find a measure of effectiveness of the SVM classifier at that node.

At each node in the wide grid search, a total of 20000 signal events and 80000 background events are used in the above 5 fold cross-validation technique. After identifying the best area in the wide grid search, the statistics are raised to 40000 signal events and 160000 background events for the finer grid search. Those events are again used in a 5 fold cross-validation to search a smaller parameter space for the best MDFs. The best SVM settings are found to be j = 0.01, c = 512, and g = 2 (figure 7.5).

After determining the best settings, the final machine is trained with 150000 signal events and 600000 background events. The resulting SVM classifier is shown in figure 7.6.

7.4 Angular Cuts

The space angle cut around each GRB should depend on the angular resolution of the IceCube detector in that direction. For each burst, a subset of the signal simulation is assembled from all the events within 10 degrees of the GRB location in detector coordinates. The angular error on those signal events is defined as the angle between the primary neutrino and the reconstructed track direction. The

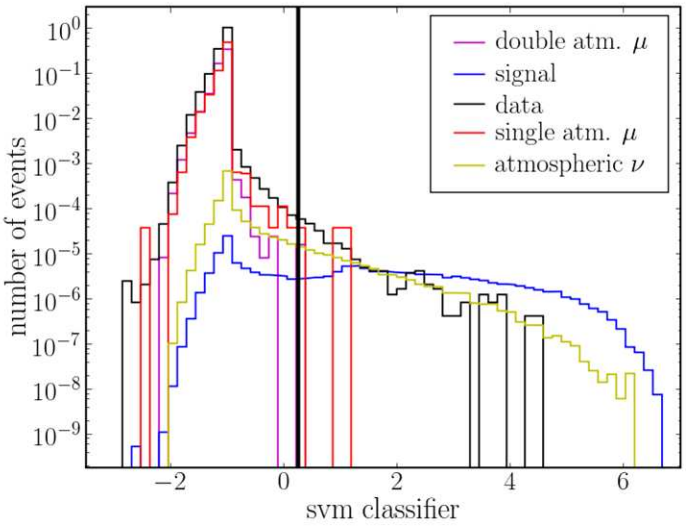

Figure 7.6: The final SVM classification distribution.

angular cut around a burst is defined as the angle at which 75% of the data in the burst's subset have an angular error less than that cut. The entire analysis was repeated for various percentages, and 75% was found to yield the best final sensitivity.

This search was optimized by finding the cut on the SVM classifier that gave the minimum 5 sigma 90 percent confidence MDF. The angle cuts around each GRB are taken to be a function of that SVM classifier cut, ie. as the SVM classifier cut changes, the events in a burst's signal subset change, and thus the angle cut around that burst changes. In this way, the data taken during each burst is subjected to a unique angle cut for that burst based on the angular resolution of the detector in that direction and a single optimum SVM classifier cut. Figure 7.7 shows the final optimum angle cuts around each GRB in this analysis.

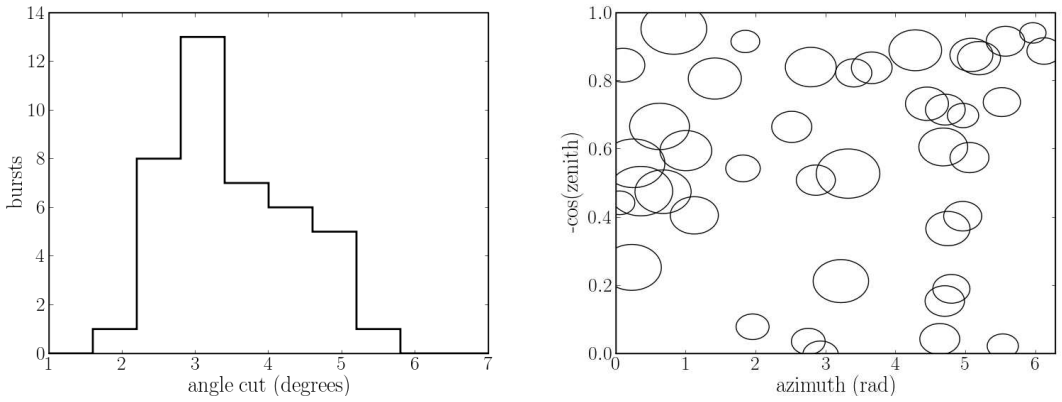

(a) (b)

Figure 7.7: The final optimum angle cuts. Panel (a) shows the values of the final angle cuts. Panel (b) shows a circle at each GRB location in detector coordinates with size relative to the optimum angle cut for that GRB. Smaller angle cuts correspond to directions with better angular resolution.

7.5 Cut Optimization

At this point, the final cut on the SVM classifier can be optimized. In this analysis, the optimal cut is defined as the one which minimizes the Model Discovery Factor (MDF) at 5 sigma power and 90 percent confidence level. To find the MDF at a certain SVM cut level, the expected number of background and signal events passing that cut must be found.

The number of signal events expected from one GRB is found by first applying the SVM cut to that GRB's subset of signal events. An implied efficiency of 75% is then applied from the definition of our angle cut. The actual value of that angle cut depends on what events survive the SVM cut, and thus it must be recalculated at each SVM cut level.

Subsets of the off-time background data are assembled in the same way that the signal events are divided up: all events within 10 degrees of a burst are added to that burst's subset. The number of background events expected from one burst is then found by applying the SVM cut to that GRB's subset of background events. The resulting number must be scaled to reflect the number of events expected in the on-time window and the space angle bin. The temporal scaling is done by dividing by the livetime of the background dataset, and then multiplying by the bursts on-time window. The space angle scaling is done by dividing by the 10 degree solid angle used when creating the subset and then multiplying by the solid angle of the burst's angle cut.

The expected number of signal and background events from each GRB are then summed into one total for the analysis at each SVM cut level. The MDF can be calculated at each cut level. This is shown in figure 7.8.

7.6 Error Estimations

7.6.1 Background Error

By definition, the minimum MDF occurs very close to a discontinuity. A misestimation of the background level could then result in a severely misplaced cut and thus a drastic overestimation of the significance of a discovery. The chances of this happening can be greatly reduced by tightening the final SVM classifier cut by an amount relative to the error on the background estimate. The MDF curve rises away from this discontinuity slowly as the cut is tightened meaning that a slightly

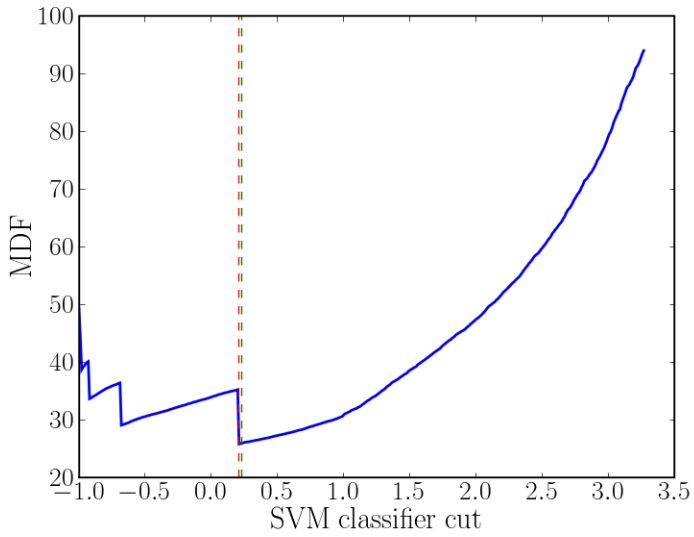

Figure 7.8: The MDF calculated at various SVM classifier cut levels. The optimum and tightened cuts are shown in red and green respectively.

tighter cut will not significantly impact the sensitivity of the analysis.

The statistical error on the background estimate is very small. This is because the entire 22-string dataset (272.3 days of data) is used to estimate the background in a ∼5000 second time window. Another reason is that each GRB's subset of background data contains events within 10° of the GRB's direction, and then that rate is scaled down to the actual bin searched around the GRB. The size of those subsets was chosen to balance the statistical error with the variability of the background rate in detector coordinates.

The error from this variability must also be considered. Figure 7.9 shows this effect at the SVM cut level and at level 4 since the SVM cut level statistics are small. In any 10° bin, the background level may vary by 10%. Most of the time, this variation is monotonic, and the errors in different directions will average to

the right value. Therefore, it is safe to assume there may be a 5% error on our background estimate from this effect.

After considering statistical and variability errors, the SVM cut is tightened until a one sigma upward deviation of the background remains less than the level at the optimum SVM cut. Table 7.2 shows the background levels and errors at the optimum and final chosen cuts. Figure 7.8 shows both SVM cuts.

Table 7.2: Error on the Background Estimation

SVM Cut	Background Estimate	Statistical	Variability	Total Error
0.22 (optimal)	1.053×10^{-3}	$\pm 3.98\%$	$\pm 5.00\%$	$\pm 6.60\%$
0.25 (tightened)	1.007×10^{-3}	$\pm 3.89\%$	$\pm 5.00\%$	$\pm 6.36\%$

7.6.2 Signal Error

The calculation of the expected number of signal events at the detector involves the use of signal simulation, and is thus affected by a couple different sources of error summarized in table 7.3.

Ice Simulation

The major systematic uncertainty arises due to the simulated propagation of light through the ice. While overall rates agree quite well between simulation and data, there are still some discrepancies visible as a function of depth. Two examples of these are shown in figure 7.10. In the deep detector, light appears to propagate farther than in the simulation, and flasher studies also indicate that this ice is clearer than simulated.

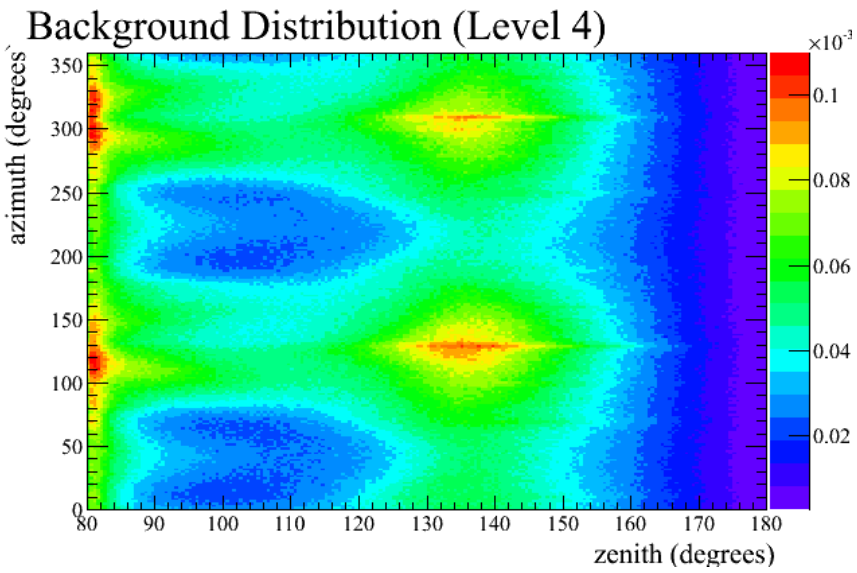

(a) Level 4

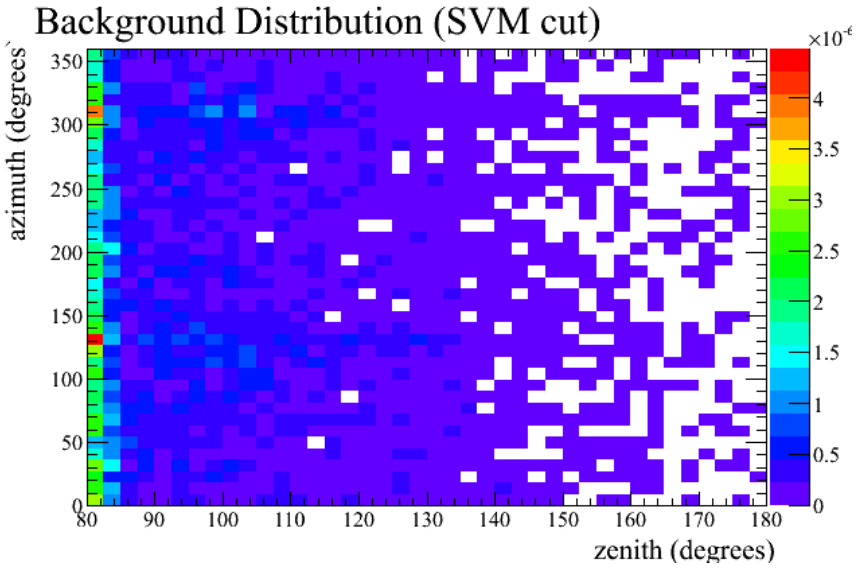

(b) SVM Cut Level

Figure 7.9: The background distribution in detector coordinates. Panel (a) shows events at level 4 and panel (b) shows events passing the SVM classifier cut at 0.25.

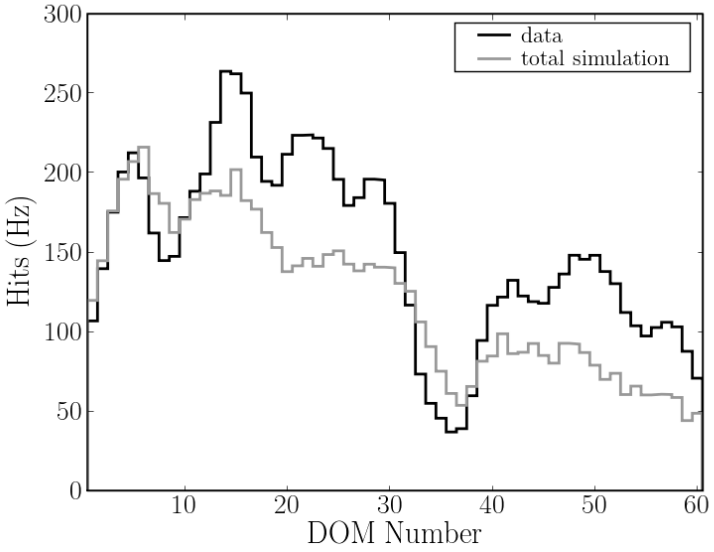

(a) DOM Occupancy

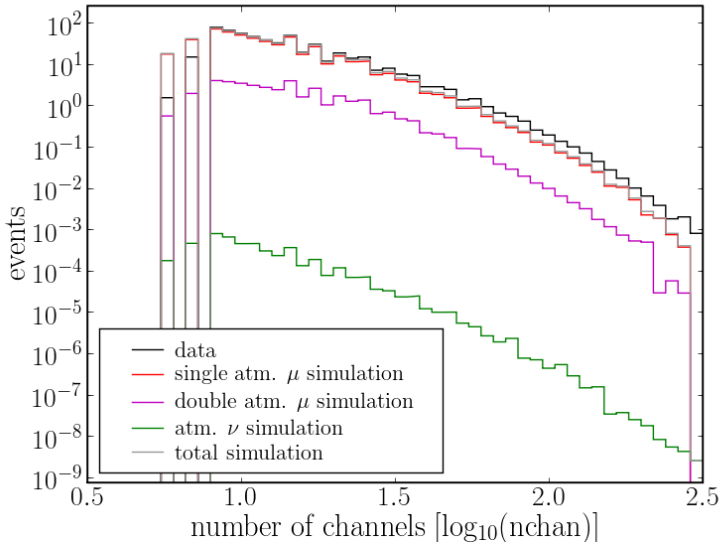

(b) Number of Hit Channels

Figure 7.10: Two disagreements between data and simulation are shown. Panel (a) shows the number of times a certain DOM number is hit per second. A clear excess of light in the bottom of the detector is observed in data above that predicted by simulation. Panel (b) shows the number of channels hit per event. Again, the higher data distribution indicates an excess of light in the detector.

Two studies were completed to try and quantify this effect. In the first one, a neutrino simulation was done with the DOM efficiencies modified as a function of depth by twice the amount that would correct the DOM occupancy disagreement. This simulation predicted a 15% higher neutrino flux [71]. Another consequence of this uncertainty in the deep ice is a disagreement in the number of channels hit (nchan) distributions. In the second study, neutrino simulation was scaled by a factor depending on nchan in order to make these distributions agree. The new simulation predicted a 13% lower neutrino flux.

Taken together, it is reasonable to assume a $\pm 15\%$ uncertainty on the signal event prediction derived from simulation based on errors on the simulation and propagation of light through the ice.

DOM Efficiency

There are uncertainties in the efficiency of the optical modules in the detection of photons. Studies have shown this effect to be on the order of $\sim 8\%$. Modifying the efficiency by $\pm 10\%$ results in an uncertainty in the event estimation from simulation of $\pm 5\%$ [71].

Neutrino and Muon Propagation

Theoretical uncertainties on muon energy losses result in a $\pm$ 3% uncertainty in the neutrino event rate in the detector [72]. Uncertainties the neutrino-nucleon cross-section (determined from the uncertainty on the CTEQ6 PDFs [73]) also contributes a 2% uncertainty.

Table 7.3: Error on the Signal Estimate

Ice Simulation	±15%
Dom Efficiency	±5%
Muon Propagation	±3%
Neutrino Cross-Section	±2%
Total Error	±16%

7.7 Results

No events survive the described cuts. A 90% confidence upper limit [74] can be placed on the neutrino flux at 166.2 times the modeled spectrum (figure 7.11). This translates to a 90% confidence upper limit on the integrated fluence from northern hemisphere bursts at 6.52×10^{-3} erg cm^{-2} with 90% of the expected signal between 87.9 TeV and 10.4 PeV.

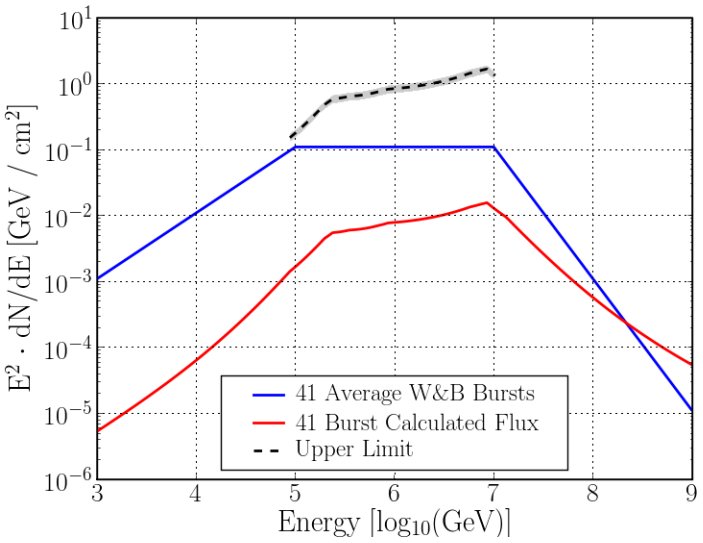

Figure 7.11: The blue curve shows the average Waxman-Bahcall flux. The red curve shows the summed individual fluxes used to optimize this analysis. The dashed black curve shows the final upper limit on the neutrino emission. The grey area represents the error on that limit.

Chapter 8

Southern Hemisphere Search

This search is meant to explore the sensitivity of IceCube to neutrinos coincident with GRBs originating in the southern hemisphere. The atmospheric muon background is much higher and varied when looking at the southern hemisphere resulting in very different sensitivities to each burst. For this reason, the bursts are not stacked, but are individually searched using an unbinned method. The analysis procedure is again developed in order to maximize the chances of discovery. On-time data is blinded until the background level is estimated from off-time data. No 5σ discovery can be claimed.

8.1 IceCube Data

Two different datasets are used in this search: filtered and triggered data. When optimizing an analysis for discovery, hard cuts are necessary and thus the filtered dataset would be preferred. Due to the high backgrounds above the horizon, though, the filtered dataset includes a cut on the zenith angle of all reconstructions at 40°. For bursts that occur above that angle, the trigger level data taken by the GRB filter provides the only available sensitivity to muon neutrinos.

8.1.1 Triggered Data

The GRB filter described in section 4.3 collected all trigger level data during a two hour period surrounding each GRB trigger time. Running all the available reconstructions on this data would be computationally restrictive, so cuts are applied during the processing. Those cuts are:

- SMT trigger satisfied
- 1 iteration SPE reconstruction $\leq 30^\circ$ away from GRB location
- 32 iteration SPE reconstruction $\leq 10^\circ$ away from GRB location

The second cut acheives the greatest background rejection. Events failing the third cut would not contribute to the likelihood in the next analysis step. The overall efficiency of these cuts is 48.6%, as calculated using point source like neutrino simulation. Figure 8.1 shows the energy dependence of this efficiency.

In addition to the data filtered by the above cuts, a small sample of background events with no angle cuts is taken from the beginning of each two hour data sample. This minimum bias sample is then used as the background to the all-sky Support Vector Machine.

8.1.2 Filtered Data

Because the focus of this analysis is on the area above the horizon, the muon filter events are supplemented by the high energy filter events described in section 3.4. This allows some sensitivity above the last muon filter zenith cut of 50°. All the reconstructions mentioned in section 5.3 are executed with the following cuts applied along the way:

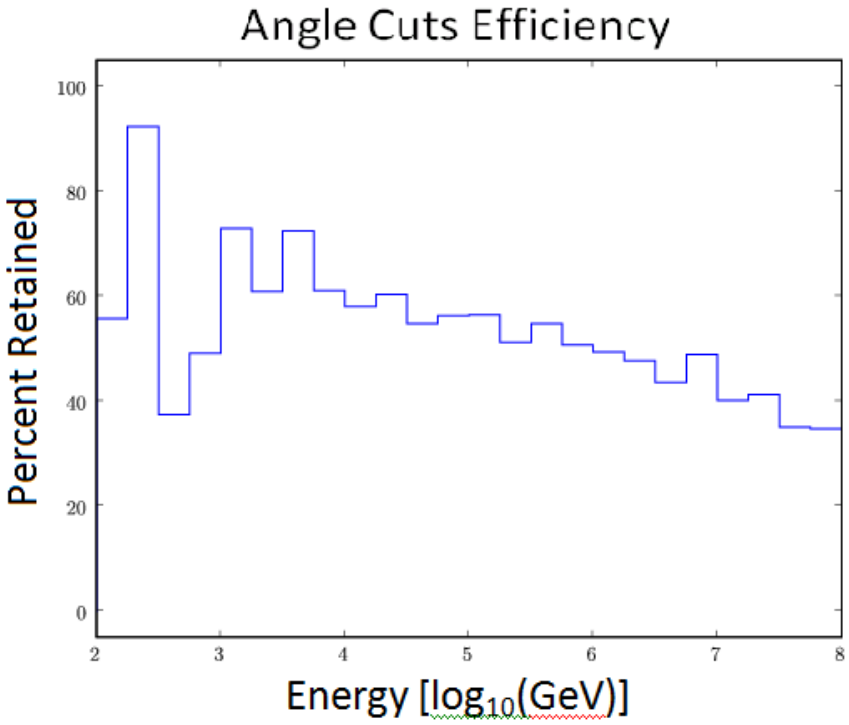

Figure 8.1: The percentage of signal events kept in relation to trigger level after directional cuts are applied. The efficiency is given as a function of neutrino energy.

- 1 iteration SPE fit and 1 iteration MPE fit zenith $\geq 40^{\circ}$
- 1 iteration SPE fit reduced log-likelihood ≤ 9
- Number of hit DOMs ≥ 20 for events with 1 iteration SPE fit zenith ≤ 80

The resulting dataset is still dominated by atmospheric muon background above the horizon. These are well reconstructed events that must be rejected by cutting on some energy indicator in order to retain signal events which have a harder spectrum than the atmospheric muons. The number of feature extracted hits per channel is found to have the strongest background rejection above the horizon at this level while also retaining good agreement between simulation and data.

Due to the strongly zenith dependent background rates and the necessity to reject lower energy events, the cut on the feature extracted hits per channel is parameterized as a function of the MPE reconstructed zenith angle and the MuE reconstructed energy. Figure 8.2 shows the square root of the remaining background rate as a histogram over over these two parameters. Using slices along the energy axis with steps of 0.05 in $\cos(\theta)$, a Gaussian is fit to the background distribution in each zenith band. This parameterization is then scaled to a cut on the average hits per channel, with the goal of reducing the downgoing atmospheric muon background and making it flat over zenith. The resulting cuts on the average hits per channel parameter are also shown in figure 8.2.

8.1.3 Simulation

Two sets of signal simulation are used in this analysis. First, a set of neutrinos from all directions is simulated at an E^{-1} spectrum. This "all-sky" neutrino

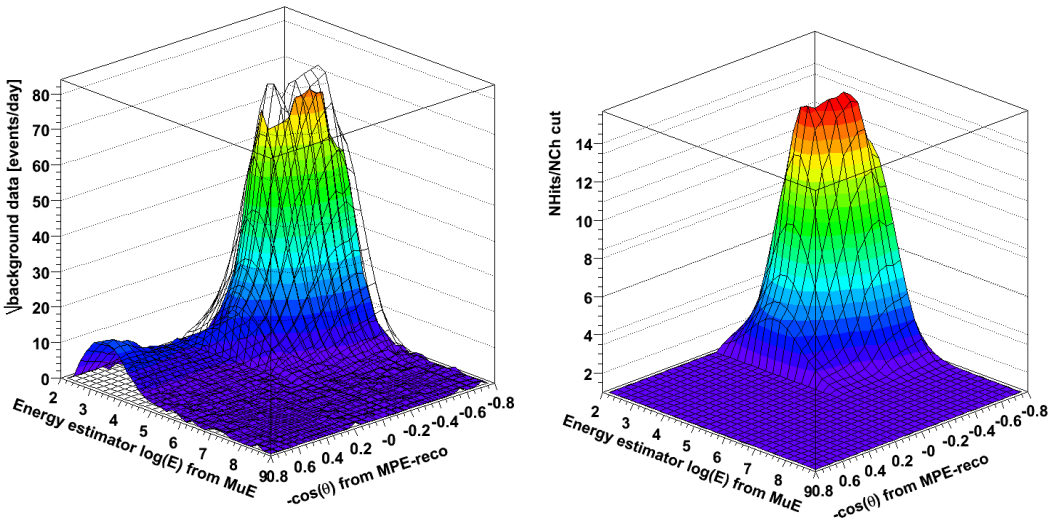

(a) Square root of background rate

(b) Cut parameterization

Figure 8.2: Panel (a) shows the square root of the background rate with respect to zenith and MuE reconstructed energy. A gaussian is fit to each energy slice and is shown as a mesh grid over the rate. Panel (b) shows the resulting parameterization of the average hits per channel cut.

simulation is then re-weighted to the average Waxman-Bahcall spectrum, and is used as the signal input to the Support Vector Machines. The second set consists of neutrinos generated from the directions of the 40 GRBs involved in this analysis. This "point-source" like simulation tracks the position of the GRBs in local detector coordinates during the burst emission and evenly distributes the neutrinos over that time period. Each burst's neutrinos are weighted to that burst's calculated neutrino flux. All those fluxes, along with those of an average Waxman-Bahcall burst, are shown in figure 4.3.

Various sets of single and double atmospheric muons are also used to simulate the background. When optimizing the analyses, real off-time data is used to estimate the background level. Consequently, none of this background simulation affects the optimization of the analysis, but it is compared to the data in order to check the quality of the simulation. Atmospheric neutrinos are not a significant source of background above the horizon compared to atmospheric muons, and so they were not simulated for this analysis.

8.2 Support Vector Machine

One SVM is trained on the filtered dataset and one is trained on the triggered dataset. In both cases, 25000 signal events from the all-sky neutrino simulation are used as the signal sample. For background, 125000 events are used. In the case of trigger level data, events are sampled from the minimum bias data sample described above. In the case of the filtered dataset, background events are evenly

sampled from the 3 million events passing the filtered dataset cuts.

Distributions of all the quality parameters that the SVM is trained on are shown in figures 8.4 and 8.6. Those quality parameters are:

- 32 iteration SPE zenith
- 32 iteration SPE azimuth
- 32 iteration SPE rlogl
- 32 iteration SPE paraboloid sigma
- Total number of feature extracted hits
- Total feature extracted charge

The SVM settings used are a cost factor of 0.1, margin of 1, and a kernel parameter of 1. An exhaustive grid search for the best SVM settings (like the one done in the northern hemisphere search) is not done because the resulting SVM classification is only used as a PDF in an unbinned likelihood method. No explicit cuts are done on this classification as in the northern hemisphere search. Instead, a limited number of different groups of settings were tried and no group showed significant improvement over the others. The settings used were chosen for their simplicity and training speed.

8.3 Unbinned Likelihood Method

The unbinned likelihood analysis method (section 6.3) is then carried out on each dataset. The signal and background PDFs for each event are described with three parts:

$$S_i^{tot}(\vec{x}, t, \vec{q}) = \mathrm{PDF}_i^{space}(\vec{x}) \times \mathrm{PDF}_i^{time}(t) \times \mathrm{PDF}_i^{SVM}(\vec{q}) \tag{8.1}$$

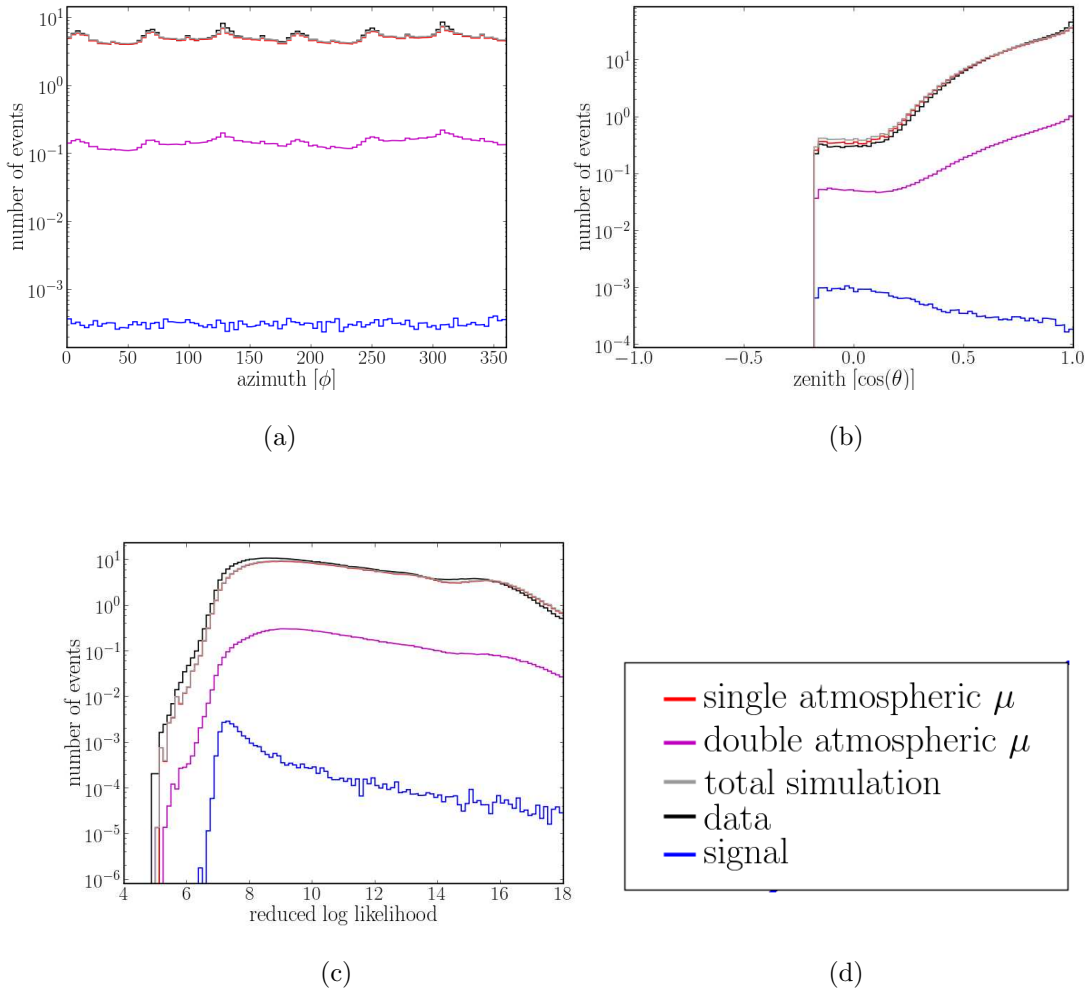

Figure 8.3: Triggered dataset quality parameters used to train the SVM.

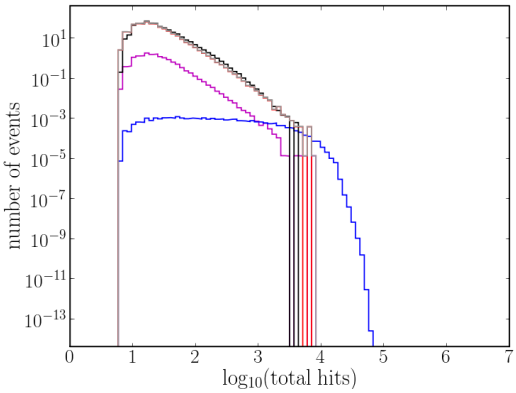

(a)

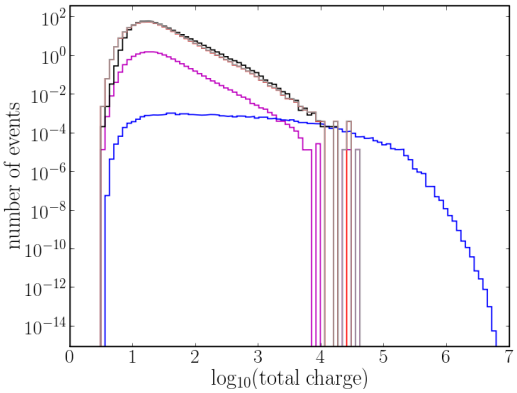

(b)

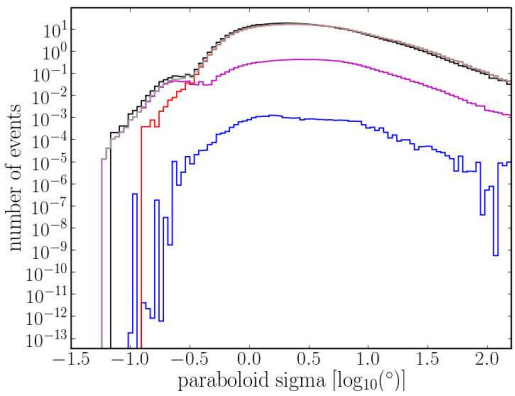

(c)

Figure 8.4: (continued) Triggered dataset quality parameters used to train the SVM.

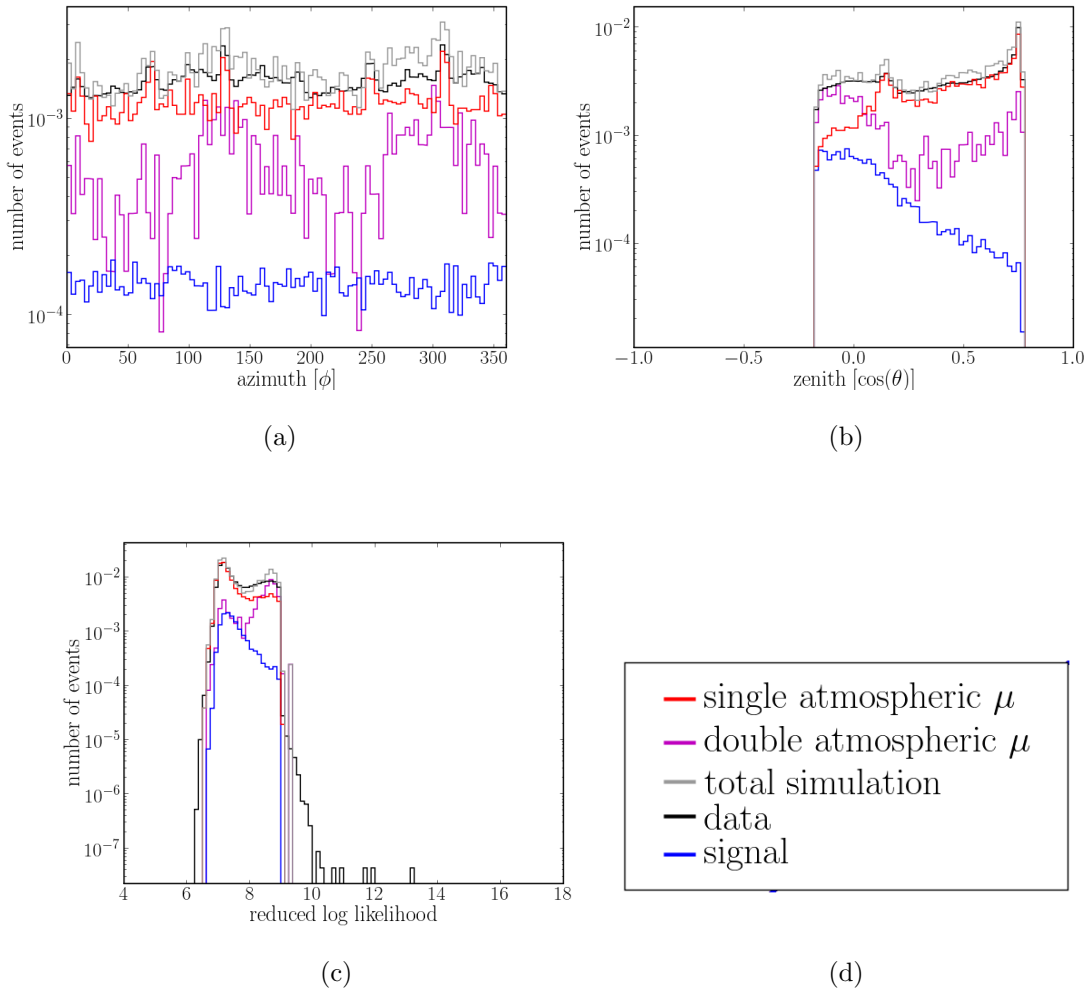

Figure 8.5: Filtered dataset quality parameters used to train the SVM.

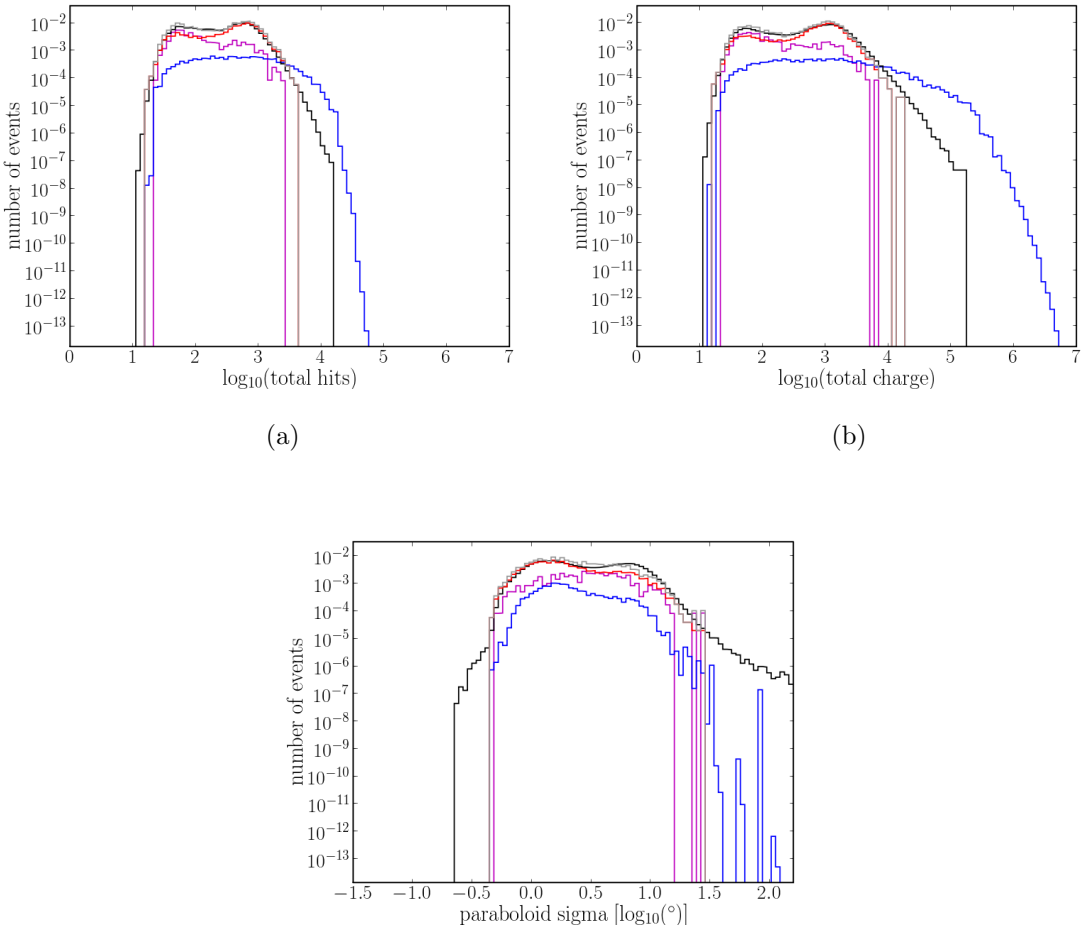

Figure 8.6: (continued) Filtered dataset quality parameters used to train the SVM.

$$B_i^{tot}(\vec{x}, t, \vec{q}) = \mathrm{PDF}_i^{space}(\vec{x}) \times \mathrm{PDF}_i^{time}(t) \times \mathrm{PDF}_i^{SVM}(\vec{q}) \tag{8.2}$$

where $\vec{x}$ represents the direction and error, t represents the time, and $\vec{q}$ represents the quality parameters of the event.

The signal space PDF is described by a two-dimensional Gaussian

$$\mathrm{PDF}_i^{space} = \frac{1}{2\pi\sigma_i} e^{-\frac{(\vec{x}_i - \vec{x}_{GRB})^2}{2\sigma_i^2}} \tag{8.3}$$

where $\vec{x}_i$ is the reconstructed direction of the event, $\vec{x}_{GRB}$ is the direction of the GRB, and σ_i is the paraboloid sigma estimation of the error on the reconstructed direction. For all but three GRBs, the uncertainty on the location of the GRB is much smaller than the uncertainty on any IceCube event ($< 0.05°$). For the three bursts listed in table 8.1, a term that accounts for the uncertainty in the position of the GRB (σ_{GRB}) is added to the signal space PDF:

$$\mathrm{PDF}_i^{space} = \frac{1}{2\pi\sigma_i} e^{-\frac{(\vec{x}_i - \vec{x}_{GRB})^2}{2\sigma_i^2}} \cdot \frac{1}{2\pi\sigma_{GRB}} e^{-\frac{(\vec{x}_i - \vec{x}_{GRB})^2}{2\sigma_{GRB}{}^2}} \tag{8.4}$$

Table 8.1: Uncertainty in GRB Localizations

GRB070626	0.25°
GRB070824	0.9°
GRB080204	0.67°

The time PDF is flat over the T_{100} of the burst. It then falls off smoothly in a Gaussian on either side to avoid discontinuities. The width of this Gaussian is equal to the burst T_{100} with a minimum of 2 and maximum of 25 seconds. This PDF is cut off on both sides two widths away from the T_{100} time period. An example time PDF for a hypothetical burst with $T_{100} = 100$ seconds is shown in figure 8.7.

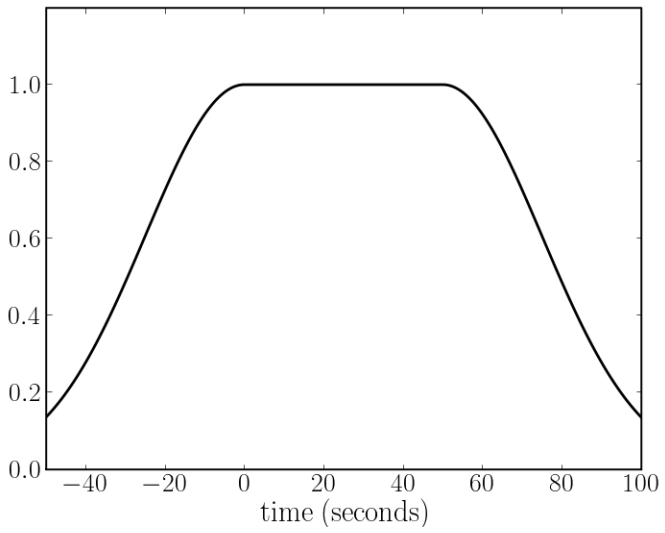

Figure 8.7: An example signal time PDF for a hypothetical burst of $T_{100} = 50$.

The background time PDF is flat over the entire on-time window. The background space PDF is taken from the actual distribution of background events in the final sample. A histogram is formed from those directions, and the PDF value at any point is evaluated with bilinear interpolation. The background space PDFs used in each analysis are shown in figure 8.8.

The signal and background SVM PDFs are formed with all-sky neutrino simulation and actual off-time background data respectively. The SVM PDFs used in each analysis are shown in figure 8.9. The PDF value is again evaluated with interpolation between bin centers.

The null hypothesis test statistic (λ) distribution is found by randomizing the background events in time. In each randomization, different events end up in the on-time region of the data and contribute to the λ minimization. The measured λs

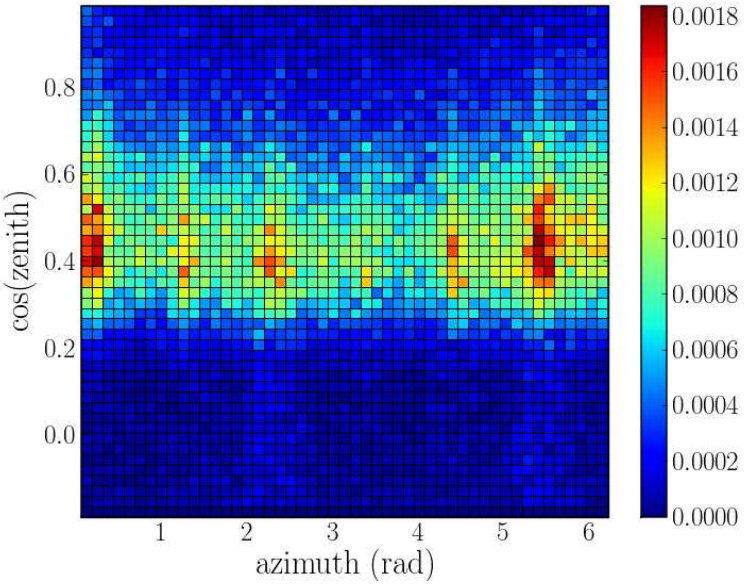

(a) Triggered Dataset

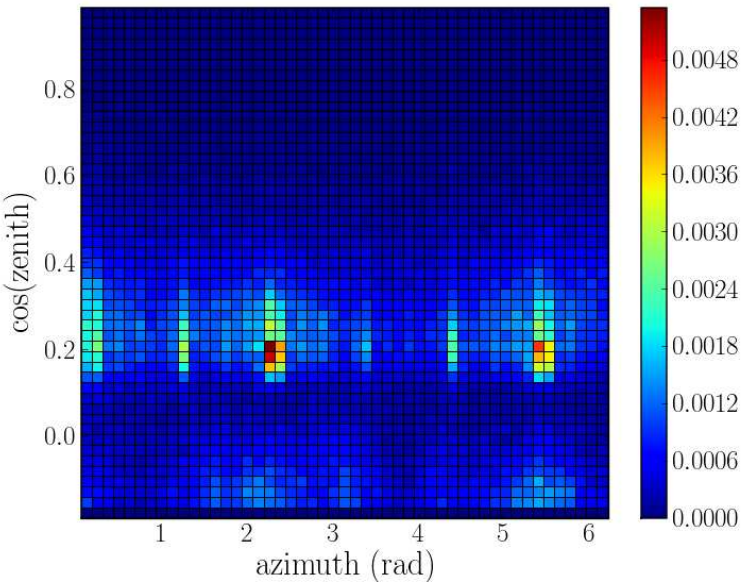

(b) Filtered Dataset

Figure 8.8: The background space PDFs for both datasets.

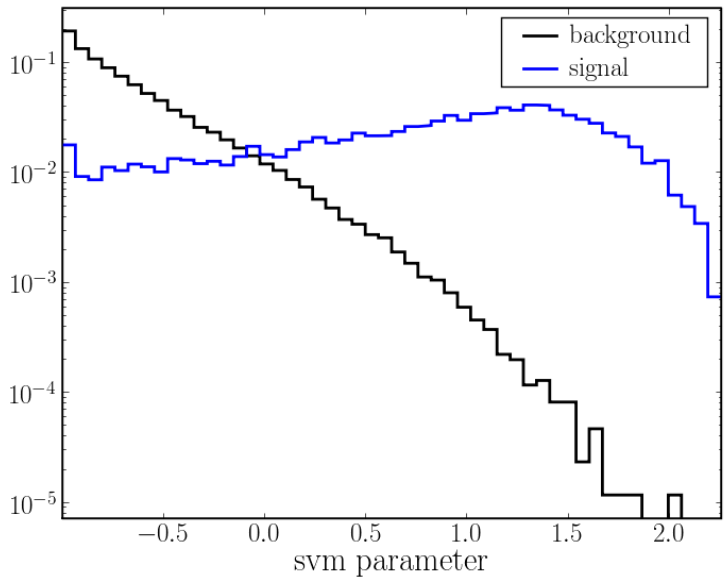

(a) Triggered Dataset

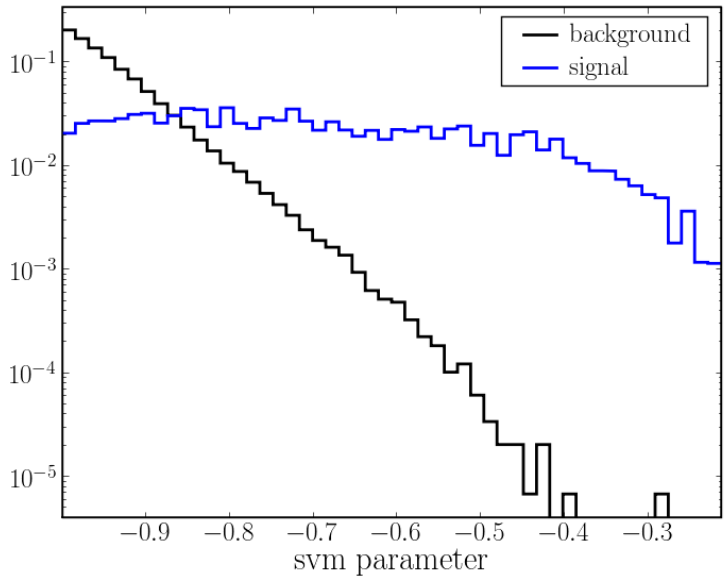

(b) Filtered Dataset

Figure 8.9: The SVM PDFs used for both signal and background in both datasets.

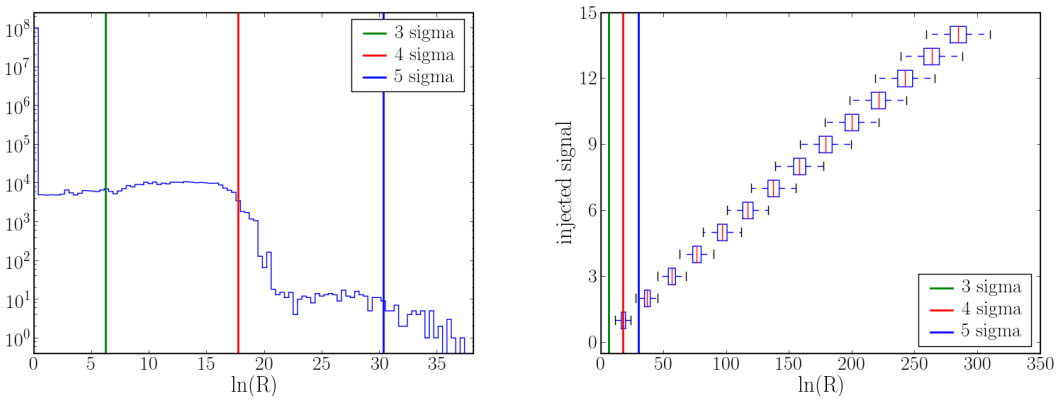

(a) Background Distribution

(b) Injected Signal Distributions

Figure 8.10: The λ distributions of filtered dataset analysis of GRB070611. Panel (a) shows the background only null hypothesis distribution with vertical lines showing the 3σ, 4σ, and 5σ significance levels. Panel (b) shows how the λ distributions of trials with various numbers of injected signal compare to those significance levels.

form the null hypothesis distribution (figure 8.10).

Signal events from the burst's point source simulation are injected to the randomized background events in order to study how the λ distribution changes. Distributions are generated for various integer number of injected signal events. For each integer number, that many signal events are picked out of the simulation sample with a probability based on their event weights.

The MDF for a given power, α, and confidence level, $1-\beta$, can then be calculated from the background and signal distributions. First, enough background randomizations are completed in order to accurately estimate the threshold where an α fraction of randomizations will yield a greater λ value. The 3σ ($\alpha = 2.70 \times 10^{-3}$), 4σ ($\alpha = 6.33 \times 10^{-5}$), and 5σ ($\alpha = 5.73 \times 10^{-7}$) thresholds are shown in figure 8.10.

Next, the fraction of each integer injected signal distribution that is greater than the α threshold is calculated. The space of injected signals is then scanned to find where the Poisson weighted sum of those fractions equals $1 - \beta$:

$$\sum_{i=1}^{\infty} \frac{e^{-n_s} n_s^i}{i!} \cdot f_i = 1 - \beta \tag{8.5}$$

This level of injected signal is analogous to the least detectable signal described in section 6.2, so it can be labeled u_{lds}. It can be divided by the signal expectation in order to get an MDF.

8.4 Iterations

Before executing the unbinned likelihood analysis method for each dataset, cuts are made on quality parameters involved in the likelihood PDFs. For both datasets, events with a 32 iteration SPE paraboloid sigma $> 5^\circ$ or an SVM classifier < -1 were cut out. These cuts serve two purposes: they make the randomizations computationally manageable and ensure that any discoveries are not based on a large number of poor quality events.

After these cuts, enough background randomizations and injected signal distributions are carried out in order to accurately estimate a 4σ 50% confidence MDF for each dataset for each burst. This amounts to 10^6 background randomizations (63 randomizations above the 4σ threshold) and 45 injected signal distributions. For each burst, the MDF from the triggered and filtered datasets are compared and the dataset with the least MDF is chosen as the best.

Because tight cuts are required when optimizing for discovery, whenever the

filtered dataset is available, it is the most sensitive. Once this was confirmed, more randomizations are carried out for the most sensitive dataset. The iterations are increased to 10^8 in order to accurately estimate a 5σ 50% confidence MDF. This best dataset is then searched for each burst. The on-time data in the most sensitive dataset is then unblinded and searched.

8.5 Error Estimations

The errors on the signal expectations are the same as those described in section 7.6 and continue to be the dominant source of error in these analyses. The error on the background estimations are not very large. Statistical errors are small for the filtered analyses because the entire off-time dataset can be used. The trigger level analyses are carried out at a very low cut level, and thus retain plentiful statistics. Seasonal variations in the background rate are at the 5% level. Ten percent variations on the background level result in $\sim 1\%$ errors on the final measured significances or limits and is insignificant compared to the $\pm 16\%$ error calculated in section 7.6.

8.6 Results

After analyzing events in the on-time windows of the most sensitive datasets for each burst, no significant discovery can be claimed. The highest background fluctuation occurs in GRB070925, representing a pre-trials significance of 3.84 sigma and a post-trials significance of 2.81 sigma (figure 8.11). This is the only burst

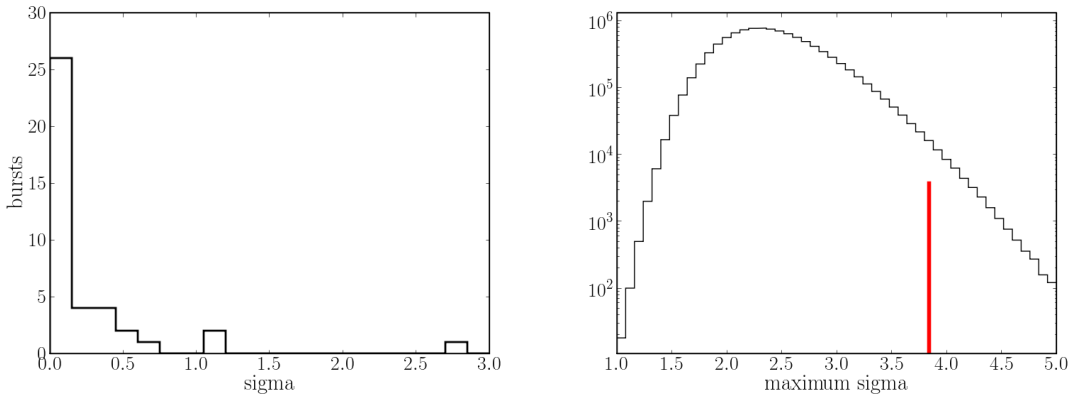

(a) Burst Significances

(b) Maximum Significance

Figure 8.11: The resulting significances of the Southern hemisphere bursts. Panel (a) histograms those significances. Panel (b) shows the maximum pre-trials significances from 10^6 repeated 40 burst experiments. The red line shows the maximum pre-trials significance of this analysis.

analyzed with the filtered dataset that has an event in the on-time window. A visualization of this event is shown in figure 8.12 and some event parameters are given in table 8.2.

Table 8.2: GRB070925 Event Parameters

GRB T_{100}	-3 to 32 seconds
Event Time	75.56 seconds
Angle to GRB	5.44°
Paraboloid Sigma	1.70°
Reduced Log Likelihood	7.30
Number of Channels	143
Total Charge	$10^{3.46}$
Total Hits	$10^{2.93}$

The plots in figures 8.13, 8.14, 8.15, and 8.16 show more details of all the events in any on-time window that contributed to the final likelihood minimizations. Each

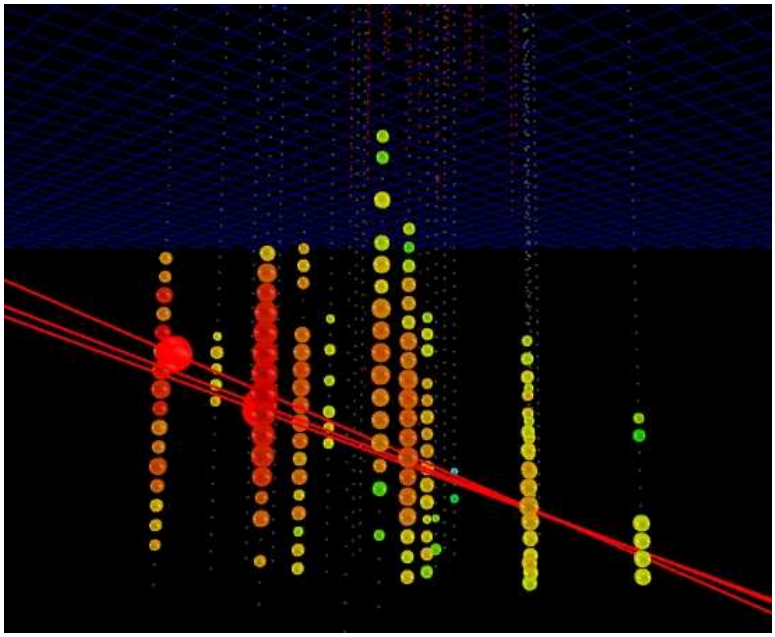

Figure 8.12: An visualization of the event in the on-time window of GRB070925. The event comes at a slight angle down through the clear ice at the bottom of the detector. The color of the hits signify the time evolution with early hits in red and later hits in yellow and green. The size of the hits is related to the logarithm of the deposited charge.

event is represented by a circle with radius equal to its reconstructed paraboloid sigma. The color refers to the SVM classifier of the event. The coordinate system has been rotated to one that is centered at the GRB location.

A 90% confidence upper limit [74] can be set on the muon neutrino flux from each individual GRB. The calculated limits are displayed in figure 8.17. The errors discussed above are assumed on each limit, though they are not shown in the figure. None of these limits, though, are competitive with the results from the northern hemisphere analysis or previous AMANDA analyses.

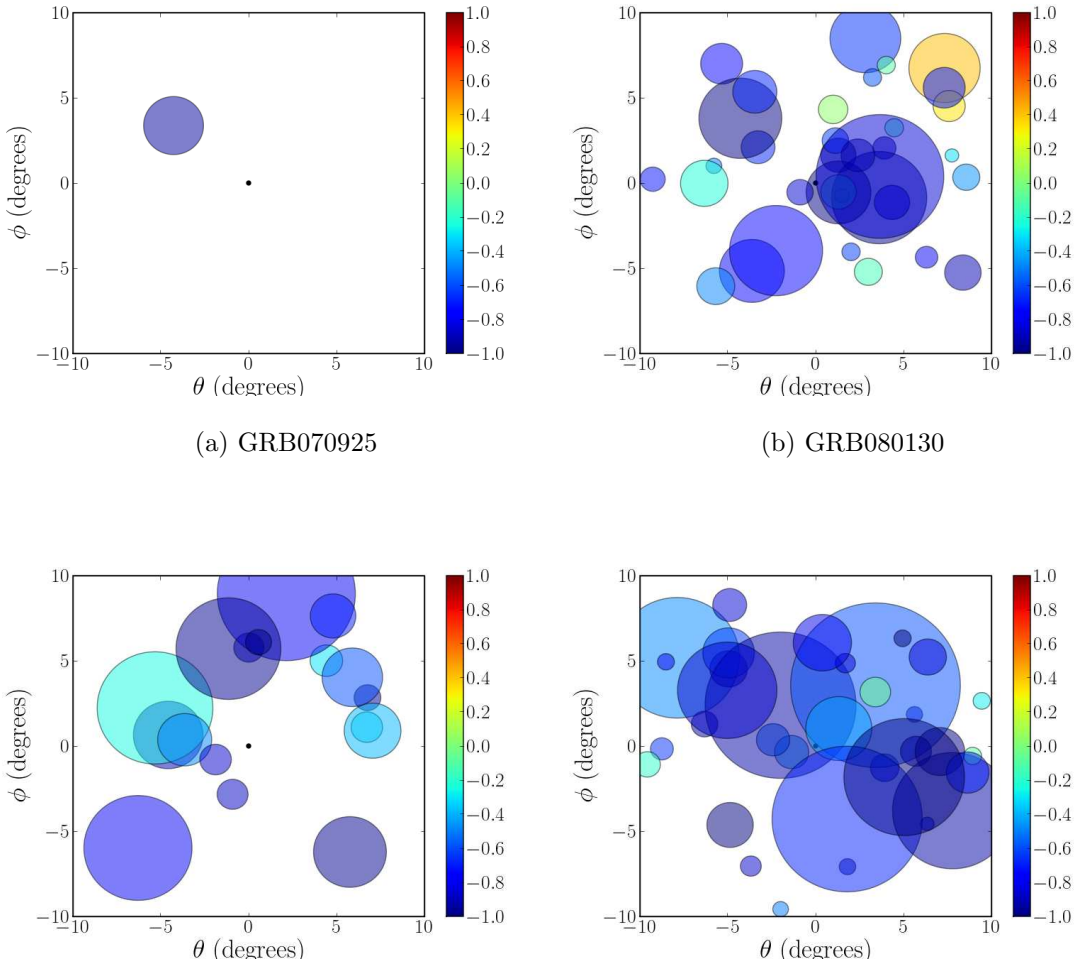

(a) GRB070925

(b) GRB080130

(c) GRB071001

(d) GRB080123

Figure 8.13: Each plot shows events that contributed to the likelihood minimization for each burst. The bursts are displayed in order from highest background fluctuation to lowest. The events are represented by a circle with radius equal to its reconstructed paraboloid sigma and color representative of its SVM classifier.

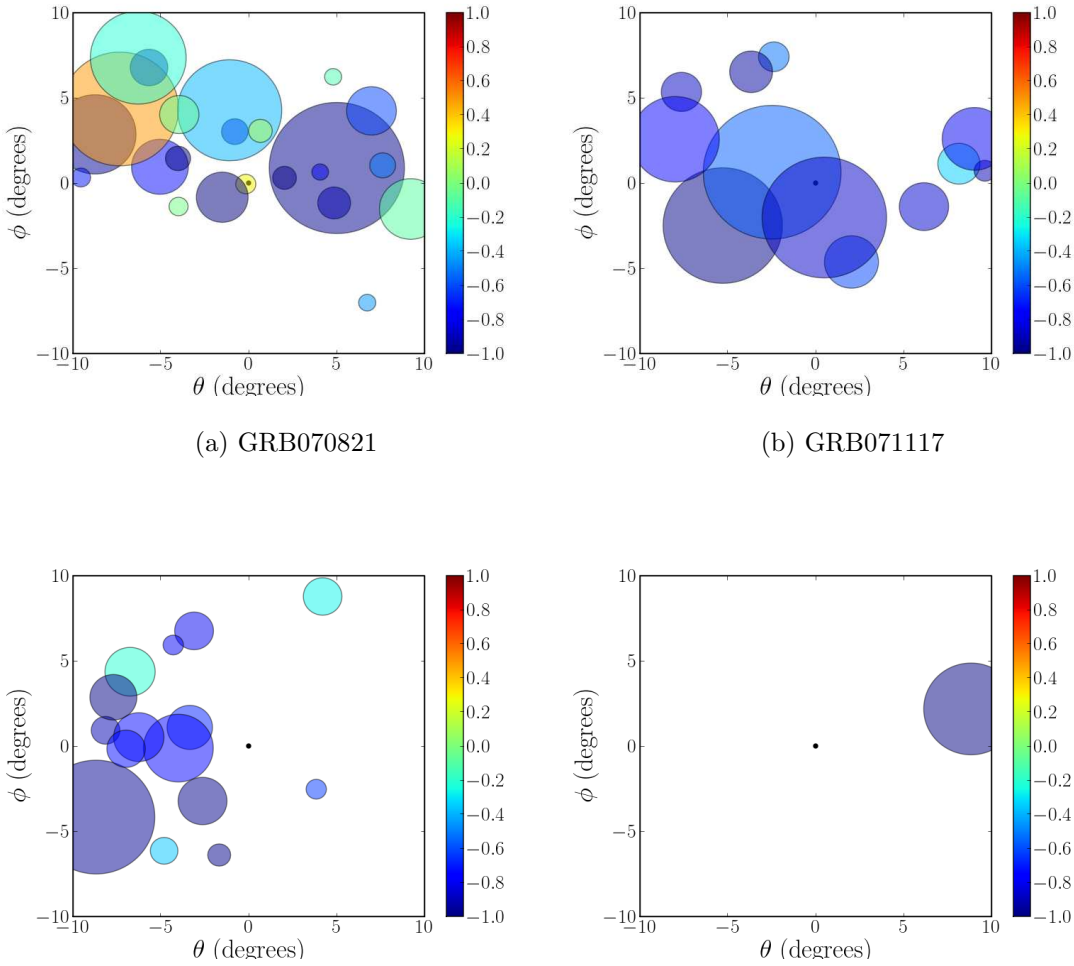

(a) GRB070821

(b) GRB071117

(c) GRB070805

(d) GRB071112B

Figure 8.14: (Continued from figure 8.13) Each plot shows events that contributed to the likelihood minimization for each burst. The bursts are displayed in order from highest background fluctuation to lowest. The events are represented by a circle with radius equal to its reconstructed paraboloid sigma and color representative of its SVM classifier.

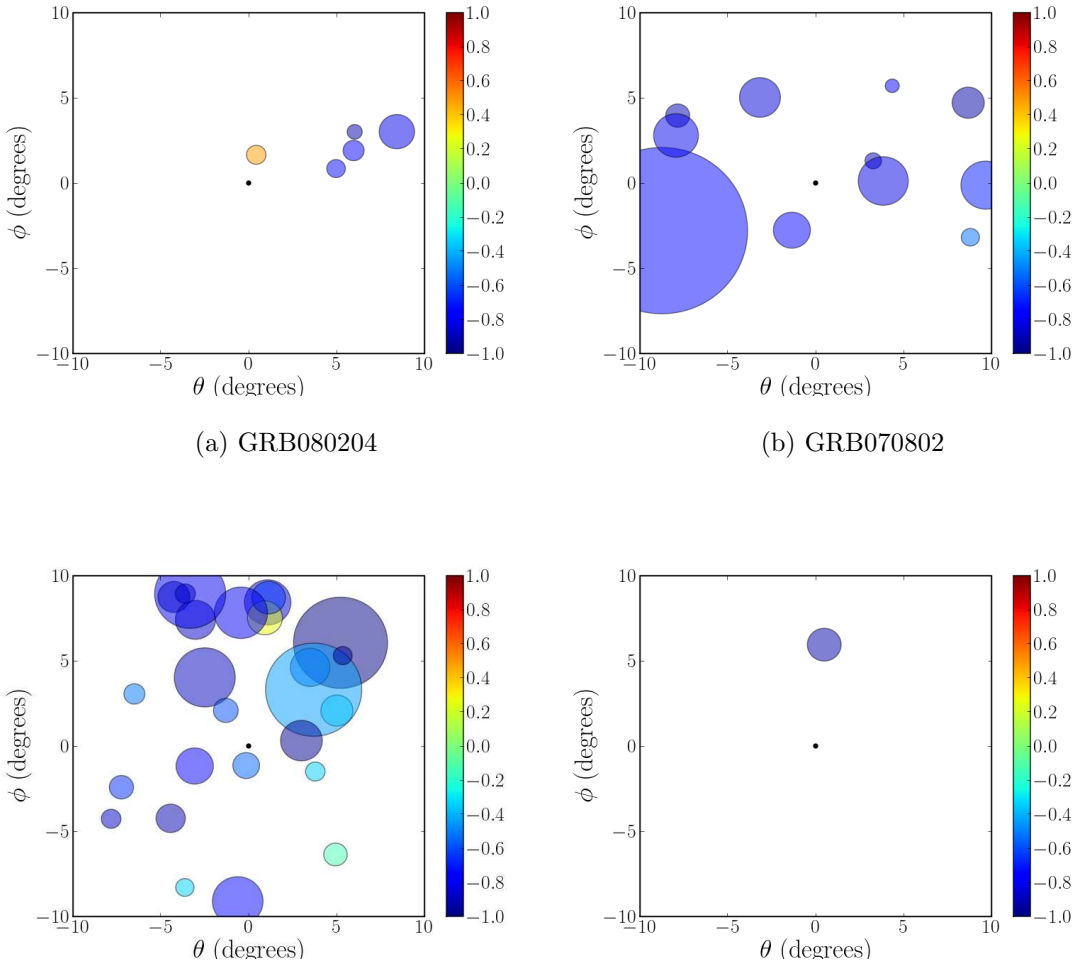

(a) GRB080204

(b) GRB070802

(c) GRB071031

(d) GRB071227

Figure 8.15: (Continued from figure 8.14) Each plot shows events that contributed to the likelihood minimization for each burst. The bursts are displayed in order from highest background fluctuation to lowest. The events are represented by a circle with radius equal to its reconstructed paraboloid sigma and color representative of its SVM classifier.

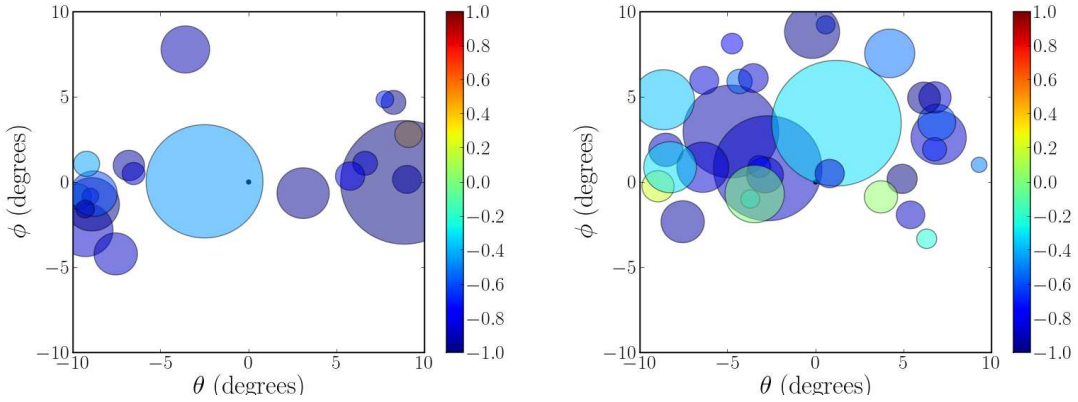

(a) GRB080303 (b) GRB080229B

Figure 8.16: (Continued from figure 8.15) Each plot shows events that contributed to the likelihood minimization for each burst. The bursts are displayed in order from highest background fluctuation to lowest. The events are represented by a circle with radius equal to its reconstructed paraboloid sigma and color representative of its SVM classifier.

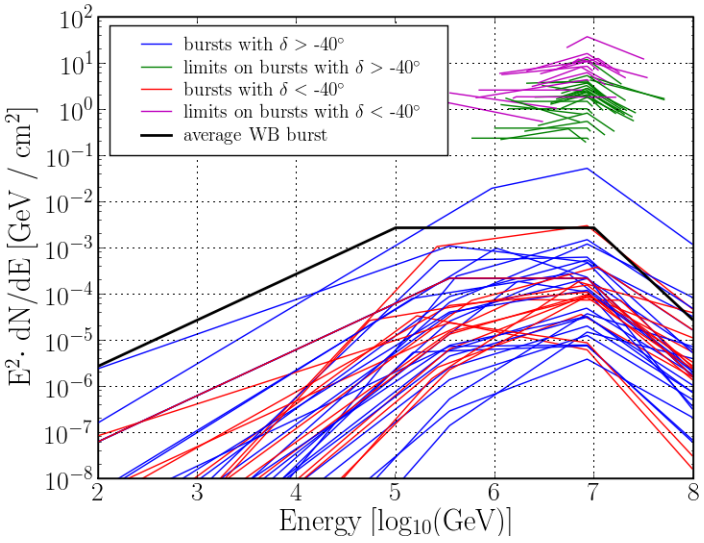

Figure 8.17: Calculated neutrino fluxes are shown for various bursts in black, red, and blue. The 90% confidence flux upper limits on those calculated fluxes from these analyses are shown in magenta and green.

Chapter 9

Summary and Outlook

The 22-string IceCube data was searched for muon neutrino events in coincidence with GRB triggers. This is the first search of its kind for IceCube and established some new techniques that will be used and improved on in future searches. 41 bursts in the northern hemisphere were searched in a binned and stacked analysis. 40 bursts in the southern hemisphere were individually searched in an unbinned analysis that is the first attempt to extend IceCube's sensitivity to GRB neutrinos into the high background regime above the horizon.

No significant fluctuation over the background hypothesis is observed in either search. A 90% confidence upper limit on the fluence from northern hemisphere bursts is set at 6.52×10^{-3} erg cm^{-2} with 90% of the expected signal between 87.9 TeV and 10.4 PeV. This limit is less stringent than the present best limit set by an AMANDA analysis with many more burst triggers.

As IceCube continues to grow, its sensitivity will quickly surpass those of existing neutrino detectors. The recently launched Fermi satellite's wide field of view will provide many more GRB triggers for analyses of this type in the future. Studies have shown that a search of data taken with the full IceCube detector with 70 GRB triggers will be sensitive to the average Waxman-Bahcall neutrino flux [75].

Bibliography

[1] S. Fukuda et al. Search for neutrinos from gamma-ray bursts using Super-Kamiokande. *Astrophys. J.*, 578:317–324, 2002.

[2] A. Achterberg et al. Search for neutrino-induced cascades from gamma-ray bursts with AMANDA. *Astrophys. J.*, 664:397, 2007.

[3] A. Achterberg et al. The search for muon neutrinos from northern hemisphere gamma-ray bursts with AMANDA. 2007.

[4] Ray W. Klebesadel, Ian B. Strong, and Roy A. Olson. Observations of Gamma-Ray Bursts of Cosmic Origin. *Astrophys. J.*, 182:L85, 1973.

[5] NASA. Compton Gamma-Ray Observatory - CGRO. 1991. URL: `http://heasarc.gsfc.nasa.gov/docs/cgro/index.html`.

[6] NASA. Burst and Transient Source Explorer - BATSE. 1991. URL: `http://www.batse.msfc.nasa.gov/batse/`.

[7] W. S. Paciesas et al. The Fourth BATSE Gamma-Ray Burst Catalog (Revised). *Astrophys. J. Suppl.*, 122:465–495, 1999.

[8] ASI. BeppoSAX. 1996. URL: `http://www.asdc.asi.it/bepposax/`.

[9] M. R. Metzger et al. Spectral constraints on the redshift of the optical counterpart to the gamma-ray burst of 8 May 1997. *Nature*, 387:878–880, 1997.

[10] MIT. High-Energy Transient Explorer - HETE-2. 2000. URL: `http://space.mit.edu/HETE/`.

[11] Krzysztof Z. Stanek et al. Spectroscopic Discovery of the Supernova 2003dh Associated with GRB 030329. *Astrophys. J.*, 591:L17–L20, 2003.

[12] NASA. Fermi homepage. 2008. URL: `http://www.nasa.gov/mission\_pages/GLAST/main/index.html`.

[13] C. L. Fryer, S. E. Woosley, and D. H. Hartmann. Formation Rates of Black Hole Accretion Disk Gamma-Ray Bursts. *Astrophys. J.*, 526:152, 1999.

[14] William H. Lee, Enrico Ramirez-Ruiz, and Dany Page. Opaque or transparent? A link between neutrino optical depths and the characteristic duration of short gamma ray bursts. *Astrophys. J.*, 608:L5–L8, 2004.

[15] Shiho Kobayashi, Tsvi Piran, and Re'em Sari. Can internal shocks produce the variability in GRBs? *Astrophys. J.*, 490:92–98, 1997.

[16] P Meszaros and M. J. Rees. Relativistic fireballs and their impact on external matter - Models for cosmological gamma-ray bursts. *Astrophys. J.*, 405:278, 1993.

[17] Enrico Fermi. On the Origin of the Cosmic Radiation. *Phys. Rev.*, 75:1169–1174, 1949.

[18] D. Band et al. BATSE observations of gamma-ray burst spectra. 1. Spectral diversity. *Astrophys. J.*, 413:281–292, 1993.

[19] T. Piran. The Phsyics of Gamma-ray Bursts. *Rev. Mod. Phys.*, 76:1143–1210, 2005.

[20] Peter Meszaros. Gamma-Ray Bursts. *Rept. Prog. Phys.*, 69:2259–2322, 2006.

[21] Bing Zhang. Gamma-Ray Bursts in the Swift Era. *Chin. J. Astron. Astrophys.*, 7:1–50, 2007.

[22] Julia K. Becker. High-energy neutrinos in the context of multimessenger physics. *Phys. Rept.*, 458:173–246, 2008.

[23] Eli Waxman and John N. Bahcall. High energy neutrinos from cosmological gamma-ray burst fireballs. *Phys. Rev. Lett.*, 78:2292–2295, 1997.

[24] Eli Waxman and John N. Bahcall. High energy neutrinos from astrophysical sources: An upper bound. *Phys. Rev.*, D59:023002, 1999.

[25] Soebur Razzaque, Peter Meszaros, and Eli Waxman. Neutrino tomography of gamma ray bursts and massive stellar collapses. *Phys. Rev.*, D68:083001, 2003.

[26] Eli Waxman and John N. Bahcall. Neutrino afterglow from gamma ray bursts: approx. 10^{18} eV. *Astrophys. J.*, 541:707–711, 2000.

[27] Dafne Guetta, D. Hooper, J. Alvarez-Muniz, F. Halzen, and E. Reuveni. Neutrinos from individual gamma-ray bursts in the BATSE catalog. *Astropart. Phys.*, 20:429–455, 2004.

[28] John N. Bahcall and Eli Waxman. High energy astrophysical neutrinos: The upper bound is robust. *Phys. Rev.*, D64:023002, 2001.

[29] Francis Halzen. Cosmic neutrinos from the sources of galactic and extragalactic cosmic rays. *Astrophys. Space Sci.*, 309:407–414, 2007.

[30] Thomas K. Gaisser, Francis Halzen, and Todor Stanev. Particle astrophysics with high-energy neutrinos. *Phys. Rept.*, 258:173–236, 1995.

[31] D. Chirkin and W. Rhode. All lepton propagation Monte Carlo. Prepared for 29th International Cosmic Ray Conference (ICRC 2005), Pune, India, 3-11 Aug 2005.

[32] The IceCube Collaboration: M. Ackerman et al. *Journal of Geophysical Research*, 111(D13203), 2006.

[33] J. Ahrens et al. Sensitivity of the IceCube detector to astrophysical sources of high energy muon neutrinos. *Astropart. Phys.*, 20:507–532, 2004.

[34] A. Achterberg et al. First year performance of the IceCube neutrino telescope. *Astropart. Phys.*, 26:155–173, 2006.

[35] R. Abbasi et al. The IceCube Data Acquisition System: Signal Capture, Digitization, and Timestamping. *Nucl. Instrum. Meth.*, A601:294–316, 2009.

[36] G. D. Barr, T. K. Gaisser, P. Lipari, Simon Robbins, and T. Stanev. A three-dimensional calculation of atmospheric neutrinos. *Phys. Rev.*, D70:023006, 2004.

[37] Giovanni Fiorentini, Vadim A. Naumov, and Francesco L. Villante. Atmospheric neutrino flux supported by recent muon experiments. *Phys. Lett.*, B510:173–188, 2001.

[38] *Hadronic Interaction Models and the Air Shower Simulation Program CORSIKA*, Hamburg, Germany, August 2001.

[39] J. Lundberg et al. Light tracking for glaciers and oceans: Scattering and absorption in heterogeneous media with Photonics. *Nucl. Instrum. Meth.*, A581:619, 2007.

[40] NASA. GCN: The gamma ray bursts coordinates network. 2009. URL: `http://gcn.gsfc.nasa.gov`.

[41] NASA. Swift satellite. 2004. URL: `http://heasarc.gsfc.nasa.gov/docs/swift/`.

[42] N. Gehrels et al. The Swift Gamma-Ray Burst Mission. *AIP Conf. Proc.*, 727:637–641, 2004.

[43] S. D. Barthelmy et al. The Burst Alert Telescope (BAT) on the Swift MIDEX Mission. 2005.

[44] David N. Burrows et al. The Swift X-ray Telescope. *Space Sci. Rev.*, 120:165, 2005.

[45] IPN. IPN3 homepage. 1990. URL: `http://www.ssl.berkeley.edu/ipn3/`.

[46] NASA. Konus-Wind homepage. 1994. URL: `http://heasarc.gsfc.nasa.gov/docs/heasarc/missions/wind.html`.

[47] ESA. INTEGRAL homepage. 2002. URL: `http://sci.esa.int/science-e/www/area/index.cfm?fareaid=21`.

[48] Sandro Mereghetti. Gamma-Ray Bursts observed by INTEGRAL. *AIP Conf. Proc.*, 727:607–612, 2004.

[49] ASI. Agile satellite. 2007. URL: `http://www.cgspace.it/index.php?option=com_content&task=view&id=143&Itemid=66`.

[50] M. Tavani et al. The AGILE space mission. *Nucl. Instrum. Meth.*, A588:52–62, 2008.

[51] JAXA. Suzaku satellite. 2005. URL: `http://www.astro.isas.ac.jp/suzaku/`.

[52] Masanori Ohno et al. Spectral Properties of Prompt Emission of Four Short Gamma-Ray Bursts Observed by the Suzaku-WAM and the Konus- Wind. 2008.

[53] C. Roucelle. Documentation for the domcalibrator module. Technical report.

[54] D. Chirkin. Feature extraction of icecube waveforms. Technical report.

[55] J. Ahrens et al. Muon Track Reconstruction and Data Selection Techniques in AMANDA. *Nucl. Instrum. Meth.*, A524:169–194, 2004.

[56] P. B. Price and K. Woschnagg. Role of group and phase velocity in high-energy neutrino observatories. *Astropart. Phys.*, 15:97–100, 2001.

[57] C. Wiebusch. Muon reconstruction with AMANDA. Prepared for International Workshop on Simulations and Analysis Methods for Large Neutrino Telescopes, Zeuthen, Germany, 6-9 Jul 1998.

[58] D. Boersma. Gulliver loglikelihood reconstruction framework. Technical report, 2009.

[59] CERN. ROOT. 1994. URL: `http://root.cern.ch/`.

[60] I. M. Sobol. *USSR Comput. Math. Math. Phys.*, 7:86–112, 1967.

[61] T. Neunhöffer. Estimating the angular resolution of tracks in neutrino telescopes based on a likelihood analysis. *Astropart. Phys.*, 25:220–225, 2006.

[62] D. Chirkin. Neutrino search with icecube. Technical report.

[63] C. Burges. A tutorial on support vector machines for pattern recognition. *Data Mining and Knowledge Discovery*, 2(2):121–167, 1998.

[64] R. Fletcher. *Practical Methods of Optimization*. John Wiley and Sons, Inc., second edition, 1987.

[65] C. Cortes and V. Vapnik. Support-vector networks. *Machine Learning*, 20(3):273–297, 1995.

[66] A. Aizerman, E.M. Braveman, and L.I. Rozoner. Theoretical foundations of the potential function method in pattern recognition learning. *Automation and Remote Control*, 25:821–837, 1964.

[67] C. Hsu, C. Chang, and C. Lin. A practical guide to support vector classification. Technical report, 2003.

[68] G. C. Hill, J. Hodges, B. Hughey, A. Karle, and M. Stamatikos. Examining the balance between optimising an analysis for best limit setting and best discovery potential. Prepared for PHYSTATO5: Statistical Problems in Particle Physics, Astrophysics and Cosmology, Oxford, England, United Kingdom, 12-15 Sep 2005.

[69] R.J. Barlow. *Statistics*. Wiley, 1989.

[70] T. Joachims. Making large-scale svm learning practical. advances in kernel methods - support vector learning. 1999.

[71] R. Abbasi et al. Search for high-energy muon neutrinos from the 'naked-eye' GRB 080319B with the IceCube neutrino telescope. 2009. arXiv:*astro-ph/09020131*.

[72] D. Chirkin and W. Rhode. Propagating leptons through matter with Muon Monte Carlo (MMC). 2002. arXiv:*hep-ph/0407075*.

[73] J. Pumplin et al. New generation of parton distributions with uncertainties from global QCD analysis. *JHEP*, 07:012, 2002.

[74] Gary J. Feldman and Robert D. Cousins. A Unified Approach to the Classical Statistical Analysis of Small Signals. *Phys. Rev.*, D57:3873–3889, 1998.

[75] A. Kappes, M. Kowalski, E. Strahler, and I. Taboada. Detecting GRBs with IceCube and optical follow-up observations. Prepared for 30th International Cosmic Ray Conference (ICRC 2007), Merida, Yucatan, Mexico, 3-11 Jul 2007.